Synthesis, radiolabeling and preclinical evaluation of gold-nanomaterial based boron carriers as drug delivery systems: Potential application to boron neutron capture therapy

Krishna Reddy Pulagam

Donostia-San Sebastian, **2020**

Synthesis, radiolabeling and preclinical evaluation of gold-nanomaterial based boron carriers as drug delivery systems: Potential application to boron neutron capture therapy

PhD Thesis

to obtain the Doctor of Philosophy degree in
Synthetic and Industrial Chemistry
at the University of the Basque Country (UPV/EHU)

by

Krishna Reddy Pulagam

Donostia-San Sebastian, **2020**

Thesis Supervisor: Dr. Jordi Llop Roig (Radiochemistry and Nuclear Imaging Group, CIC biomaGUNE)

University Tutor: Dr. María Esther Lete Expósito (Department of Organic Chemistry II, Faculty of Science and Technology, University of the Basque Country (UPV/EHU))

Table of contents

Table of contents

Table of contents

Table of contents

Acknowledgements

First and foremost, I would like to express my sincere gratitude to Prof. Manuel Martín Lomas and Prof. Luis M. Liz Marzán, former and current scientific directors of CIC biomaGUNE, respectively, for giving me the opportunity to execute the experimental work of this PhD in top quality research facilities of the centre.

I would like to thank my research supervisor Dr. Jordi Llop, who accepted me in to his research group to carry out my PhD work; thanks for teaching me many things to explore this fascinating field. I must say that I am extremely lucky to find a place in your group and you never stopped supporting me even in complicated times throughout last four years. I am forever grateful for your mentorship. Special thanks also to Dr. Vanessa Gómez-Vallejo for her kind and generous heart and tremendous support since the very beginning of my PhD. Thanks for all the encouraging words and help during the experimental work.

I would like to acknowledge my tutor Prof. Dr. Esther Lete from the University of Basque country (UPV/EHU), for her valuable guidance and feedback during last four years.

I would like to thank my former and current colleagues in the Radiochemistry and Nuclear Imaging Group and molecular imaging platform: Olatz, Larraitz, Sameer, Eunice, Unai, Luka, Zurine, Marcos, Angel, Ana Beatriz, Cristina, Ana Joya, Riccardo, Rossana, Pilar, Oscar, Luis, Aitor, Xabi, Victor, especially to Zuriñe, Ane, Kepa and Irene who were highly involved in my experiments. Thank you so much guys for supporting me all these years, both morally and technically. It has been a great privilege to work with such wonderful people.

Many thanks to my collaborators: Prof Irina Estrela-Lopis and her group from University of Leipzig for their tremendous support during *ex vivo* quantification work of gold nanosystems. Prof. Luis M. Liz Marzán and his group, namely, Dr. Jatish Kumar, Dr. Malou Henriksen and Vished for their support during gold nanorods work. Special thanks to Abraham and Monica for their support during collaborative work.

I am also grateful to all the platform managers, who offered their continuous support for completing my work on time. I thank Javier and Dorleta for their excellent support in mass

spectrometry and ICP-MS analysis, Desire for her excellent support in XPS analysis, Dani for his help in NMR studies, Unai for his exceptional support during imaging studies.

A special thanks to people of animal facility unit, Ainhoa and Ander for their tremendous support during *in vivo* studies.

I would also like to thank all the people of administration, maintenance, information technology and other supporting departments.

I also take this opportunity to thank my friend Dr. Kiran for his help to get the opportunity to work in Dr. Jordi Llop group. I am extremely grateful for your favour.

I want to thank all my family members in India, Nanna-Amma, Bava-chelli, and Babai-Pinni for their constant inspiration and encouragement.

Last but not least I owe my deepest gratitude towards my wonderful wife Anusha, as without her unwavering support I would not have been able to complete my thesis. Lots of love to my son Shourya.

Summary

Binary therapeutic approaches, in which two low-toxicity components are only activated when combined and co-localized in tumors, are a promising strategy to reduce morbidity and improve mortality. One of such approaches is Boron Neutron Capture Therapy (BNCT). In this therapeutic modality, high levels of boron atoms are accumulated in tumors, which are subsequently irradiated with thermal neutrons to trigger cellular damage via the $^{10}B(n, \alpha, \gamma)^{7}Li$ nuclear reaction. To date, two compounds have been tested in clinical practice showing promising results, but with limitations and only in specific tumor types.

The successful application of BNCT has been thwarted by a number of problems, not least the unease around conducting clinical irradiations in nuclear research reactors. This drawback has been recently mitigated by the installation of hospital-based accelerators delivering high intensity epithermal neutron beams. Apart from this, the main limitation of BNCT is the need to develop drugs that are able to deposit a sufficient number of ^{10}B atoms specifically (or preferentially) in tumor cells or tissues. Abnormal metabolism and the over-expression of certain membrane receptors have previously been exploited to accumulate ^{10}B nuclei in cancer cells. Small boron molecules have been used to prepare carbohydrate, amino acid, peptide, and nucleic acid derivatives and immunoconjugates, although results have been far from optimal.

The recent emergence of nanotechnologies has opened new avenues for the development of nanomaterial-based boron carriers. Nanomaterials have the advantage that, when appropriately designed, have a long circulating half-life and preferentially accumulate in cancer tissues due to the enhanced permeability and retention (EPR) effect. In the current PhD thesis, we have worked on the development of gold-nanomaterial based boron carriers with potential application in BNCT.

First, we synthesized and characterized spherical gold nanoparticles (AuNPs) with a core diameter of ca. 20 nm. The AuNPs were functionalized simultaneously with poly(ethylene)glycol (PEG) and the boron rich anion cobalt-bis(dicarbollide), commonly known as COSAN. Radiolabeling of the NPs both at the core and the shell was achieved by using the positron emitter Iodine-124, in order to enable *in vivo* tracking using positron emission tomography. The

biodistribution of the AuNPs was monitored in a mouse tumor model, generated by subcutaneous inoculation of HT 1080 cells. PET images revealed high accumulation of the radioactivity in the liver at short times after administration, suggesting sequestration of the NPs by the mononuclear phagocytic system and consequent low bioavailability, which resulted in low tumor accumulation. Comparison of the results obtained with the NPs labeled both at the core and the shell confirmed good stability of the NPs *in vivo*. These results are included in Chapter 3.

The results obtained in chapter 3 suggested the need for the modification of the characteristics of the NPs, in order to prolong circulation time and enhance tumor accumulation. Hence, we synthesized and characterized smaller NPs with a similar surface functionalization. With that aim, NPs with core sizes of ca. 3 and 10 nm and functionalized with PEG and COSAN were prepared and characterized using different techniques. The NPs showed low toxicity and good internalization properties in cells. Radiolabeling to enable *in vivo* imaging was achieved by incorporation of the positron emitter copper-64 into the gold core. Biodistribution studies confirmed that medium sized NPs (core size of ca. 10 nm) rapidly accumulated in the liver and showed low accumulation in the tumor. However, the smallest NPs, with a cores size of ca. 3 nm, showed long circulation time, lower accumulation in the liver and higher accumulation in the tumor, with maximum values at t = 24 hours (5.3±1.3 %ID/cm^3). These values progressively decreased afterwards (3.92±1.7 %ID/cm^3 at t = 48 hours). Additionally, good tumor discrimination could be observed on the PET images.

In spite of the improvement in tumor accumulation obtained in chapter 4, the concentration of boron in the tumor was insufficient to tackle therapeutic efficacy experiments. Hence, the next step was to design therapeutic agents enabling the combination of BNCT with another therapeutic modality. Taking advantage of the capacity of gold nanorods to interact with infrared light to generate local heating, we decided to prepare gold nanorods simultaneously functionalized with PEG and COSAN, in order to enable simultaneous or sequential BNCT and photothermal therapy. The resulting GNRs showed good internalization capacity in MKN45 cells and low toxicity both in MKN45 and human dermal fibroblasts (HDFa). Treatment of the GNRs with $^{64}CuCl_2$ in the presence of a reducing agent enabled the incorporation of the positron emitter at the gold core, resulting in stable labeling in different media. *In vivo* biodistribution experiments in a xenograft mouse model generated by inoculation of MKN45 cells demonstrated significant tumor accumulation and favorable tumor-to-muscle ratios at 24–48 hours after

administration. Such multidecorated GNRs carry large amounts of boron, and hence bear the potential to become a valuable tool for the development of nanoparticle-based BNCT agents. This, together with the capability to absorb near infrared light, opens new avenues for their use in combined therapies (BNCT + photothermal therapy).

Resumen

A pesar de los avances recientes, el cáncer sigue siendo un problema urgente de salud pública. Los avances en el diagnóstico temprano y el tratamiento del cáncer han elevado la tasa de supervivencia a 5 años para todos los cánceres del 50% (1974) al 68% (2007). Sin embargo, el cáncer todavía representó 8.2 millones de muertes en todo el mundo en 2012. Por lo tanto, se requiere con urgencia el desarrollo de nuevos tratamientos y terapias, pero dado que muchas terapias resultan altamente tóxicas para los pacientes, la eficacia terapéutica debe equilibrarse con los efectos secundarios y tóxicos derivados de la propia terapia.

Los enfoques binarios para la terapia contra el cáncer, en los que dos componentes del tratamiento de forma individual presentan baja toxicidad pero al combinarse presentan efecto terapéutico, son estrategias prometedoras para mejorar los resultados terapéuticos y reducir los efectos secundarios.

Una opción es la terapia de captura de neutrones de boro (BNCT). Esta terapia se basa en la alta propensión del boro-10 (^{10}B) a capturar neutrones térmicos, lo que da como resultado la reacción nuclear $^{10}B(n, \alpha, \gamma)^{7}Li$. Las partículas alfa y los iones de ^{7}Li presentan una transferencia de energía lineal muy elevada, y alcances en el rango del diámetro de una sola célula. Por lo tanto, si se acumula una cantidad suficiente de ^{10}B de manera selectiva o preferente en las células tumorales y posteriormente se irradia la zona tumoral con neutrones, es posible generar daño selectivo en el tumor, con afectación mínima del tejido sano circundante (Figura 1).

La aplicación de la BNCT se ha visto limitada por una serie de problemas, entre ellos la inconveniencia de requerir una fuente de neutrones, lo que obligaba a realizar las pruebas en las inmediaciones de un reactor nuclear. Sin embargo, este inconveniente ha sido mitigado recientemente por la instalación de aceleradores hospitalarios capaces de generar haces de neutrones de alta intensidad. La segunda limitación se debe a la necesidad de desarrollar fármacos que puedan depositar un número suficiente de átomos de ^{10}B específicamente (o preferentemente) en células o tejidos tumorales. Históricamente, se han explotado el metabolismo acelerado y la sobreexpresión de ciertos receptores de membrana que tienen lugar en las células tumorales, para generar fármacos con alto contenido en boro y capaces de acumularse en el

tumor, si bien los resultados no han sido muy prometedores y en la actualidad sólo hay dos compuestos que se utilizan en el entorno clínico. Además, éstos muestran poca especificidad y su aplicación se limita a un número restringido de tumores.

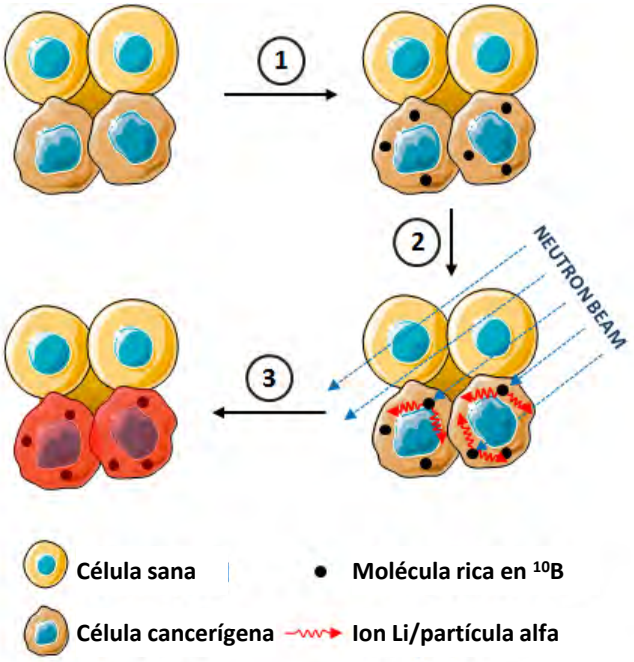

Figura 1. Esquema del principio de la BNCT. Si se acumula una cantidad suficiente de ^{10}B de manera selectiva o preferente en las células tumorales y posteriormente se irradia la zona tumoral con neutrones, es posible generar daño selectivo en el tumor, con afectación mínima del tejido sano circundante.

Los avances recientes en el área de la nanotecnología han abierto nuevos horizontes para la BNCT. Los nanomateriales, tras ser administrados por vía intravenosa, tienen la capacidad de acumularse de forma pasiva en los tumores gracias al llamado efecto *enhanced permeability and retention* (EPR). Durante el crecimiento tumoral, se produce neo-angiogénesis, de modo que se generan nuevos vasos sanguíneos de forma rápida y generalmente desestructurada. Por ese motivo, los vasos sanguíneos son imperfectos, dejando huecos por los cuales los nanomateriales pueden permear. Este hecho, unido a un drenaje linfático deficitario, facilita la acumulación de nanomateriales en los tumores.

El efecto EPR ha contribuido a que una de las mayores aplicaciones de los nanomateriales en biomedicina sea en el desarrollo de fármacos para diferentes tipos de cáncer. En este contexto, el desarrollo de fármacos con aplicación en BNCT no ha quedado al margen, y se han descrito un

gran número de nanosistemas ricos en boro que podrían solventar el problema histórico asociado a la BNCT.

En esta tesis doctoral, se pretende el desarrollo de diversos nanosistemas base oro, con un alto contenido en boro, como posibles candidatos para su aplicación en BNCT. Con el fin de probar su capacidad de acumularse en el tejido diana (tumor), se han desarrollado diferentes estrategias de marcaje con isótopos emisores de positrones (PET), con el fin de permitir su monitorización tras administración a animales utilizando tomografía por emisión de positrones.

En primera instancia (trabajo incluido en el capítulo 3), se optó por la utilización de nanopartículas (NPs) de oro (AuNPs) de un tamaño de núcleo alrededor de 20 nm, ya que este es un tamaño adecuado para la acumulación de nanomateriales en tumores debido al efecto EPR. Con el fin de conferir estabilidad *in vivo* a las NPs, se decidió incorporar polietilenglicol (PEG) en la superficie de las NPs. Asimismo, se incorporó el anión cobalto bis(dicarballuro), denominado comúnmente COSAN, un clúster de boro y carbono que contiene 18 átomos de boro en la estructura. El anclaje de ambos (PEG y COSAN) en la superficie de las NPs se llevó a cabo mediante la bien conocida química de tioles. Las NPs resultantes se caracterizaron mediante un conjunto de técnicas, incluyendo microscopía electrónica de transmisión (TEM), dispersión dinámica de luz, espectrofotometría UV-Vis, espectroscopía Raman y espectroscopía fotoelectrónica de rayos X. Los análisis demostraron la formación de NPs con diámetro de núcleo de 19.2±1.4 nm, diámetro hidrodinámico de 37.8±0.5 nm, y un valor de potencial zeta de −18.0±0.7 mV a pH neutro. Además, quedó confirmada la presencia de boro en la superficie. Con el fin de permitir la realización de estudios *in vivo* mediante PET, se abordó la incorporación del isótopo emisor de positrones yodo-124 tanto en el núcleo (mediante adsorción aniónica sobre la superficie de oro) como en la corteza (mediante incorporación del átomo de yodo sobre el clúster de boro). Para determinar el tiempo de circulación en sangre y la capacidad de los nanosistemas de acumularse en el tumor, se realizaron ensayos en un modelo tumoral de ratón, generado mediante inoculación subcutánea de células HT 1080 (fibrosarcoma). Los estudios PET demostraron una rápida acumulación de las NPs en el hígado, con la consecuente baja biodisponibilidad, que resultó en última instancia en una muy baja acumulación en el tumor. Sin embargo, los estudios efectuados con el doble marcaje secuencial demostraron una buena estabilidad de los nanosistemas *in vivo*.

Los resultados obtenidos en el capítulo 3 sugirieron la necesidad de modificar las características de las NP para prolongar el tiempo de circulación y mejorar la acumulación en tumor. En consecuencia, se optó en este segundo trabajo (incluido en el capítulo 4) por preparar y caracterizar NPs similares a las incluidas en el capítulo 5, pero con dos tamaños de núcleo diferentes, alrededor de los 3 y los 10 nm. En este caso, se optó por una estrategia para el marcaje radioactivo basado en la incorporación del isótopo emisor de positrones cobre-64 (^{64}Cu) en el núcleo de las NPs, para de este modo minimizar la pérdica del radioisótopo durante los estudios *in vivo*. Las NPs diseñadas demostraron una baja toxicidad *in vitro* en tres líneas celulares, y una buena capacidad de internalización en la línea celular MKN45 (carcinoma gástrico). Tras efectuar el marcaje con buena eficiencia, se abordaron estudios de imagen utilizando PET-CT en un modelo murino de cáncer, generado mediante inoculación de células MKN45 en ratones inmunodeprimidos. Los estudios efectuados con las NPs con tamaño de núcleo de ca. 10 nm mostraron una rápida acumulación en el hígado, resultando en una baja biodisponibilidad y en consecuencia en una baja acumulación en el tumor a los diferentes tiempos de estudio (1-48h). Sin embargo, las NPs con tamaño de núcleo de ca. 3 nm mostraron una mayor circulación en sangre, una menor retención en el hígado y una mayor acumulación en el tumor (Figura 2), con valores de 5.3±1.3 %de dosis inyectada por cm^3 a las 24 horas tras administración. Posteriormente, se observe una disminución progresiva en este tejido.

A pesar de la mejora en la acumulación tumoral obtenida en el capítulo 4, la concentración de boro en el tumor puede considerarse insuficiente para abordar los experimentos de eficacia terapéutica únicamente atendiendo a la modalidad de BNCT. Por lo tanto, el siguiente paso fue diseñar agentes terapéuticos que permitieran la combinación de BNCT con otra modalidad terapéutica. Aprovechando la capacidad de los *nanorods* de oro (GNRs) para interactuar con la luz infrarroja para generar calentamiento local, se decidió preparar *nanorods* de oro funcionalizados simultáneamente con PEG y COSAN, de manera similar a lo llevado a cabo en los capítulos anteriores. El hecho de disponer de *nanorods* funcionalizados con moléculas ricas en boro debería permitir combinar dos modalidades terapéuticas, BNCT y terapia fototérmica. La síntesis y funcionalización de los NRs se llevó a cabo mediante métodos previamente establecidos, si bien se ajustaron los parámetros experimentales para obtener nanosistemas con un tamaño de núcleo de 37±3 × 10±1 nm (ratio de aspecto de 3.7), según demostraron los estudios de TEM, y con un potencial-zeta de -12±2 mV. La presencia de boro en la superficie se demostró

mediante análisis por EDX y espectrofotometría UV-Vis. Los GNR resultantes mostraron buena capacidad de internalización en células MKN45 y baja toxicidad tanto en células MKN45 como en fibroblastos dérmicos humanos (células HDFa).

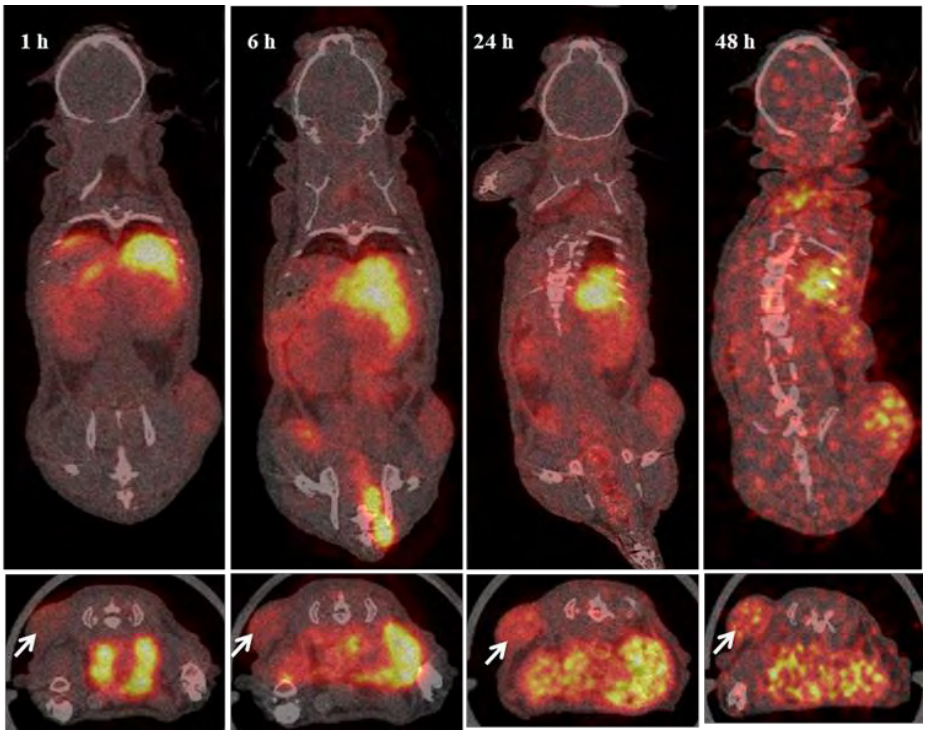

Figura 2. Imágenes PET (vistas coronales y axiales) representativas, obtenidas a las 1, 6, 24 y 48 horas después de la administración de NPs con tamaño de núcleo de ca. 3 nm, marcadas con ^{64}Cu, en un modelo animal de ratón generado por inoculación subcutánea de células MKN-45. Las imágenes PET son proyecciones de máxima intensidad, y se muestran corregistradas con cortes representativos de imágenes CT correspondientes al mismo animal, para facilitar la localización de la señal radiactiva. La posición del tumor se indica con flechas blancas.

Posteriormente, se abordó el marcaje de los GNRs con un isótopo emisor de positrones, en este caso ^{64}Cu, que se incorporó en el núcleo mediante proceso de reducción in situ en presencia de hidracina. El marcaje mostró alta estabilidad en diferentes medios de incubación. Finalmente, se aboradron estudios de biodistribución *in vivo* en un modelo tumoral de ratón generado por inoculación de células MKN45. Los GNRs mostraron una buena acumulación en el tumor, con valores por encima del 3% de dosis inyectada por gramo de tejido, y ratios de concentración respecto a tejido sano favorables a las 24-48 horas tras la administración (Figura 3).

La acumulación en tumor de los GNRs permite anticipar que sería posible llevar a cabo estudios terapéuticos combinando las dos modalidades terapéuticas, BNCT y terapia fototérmica.

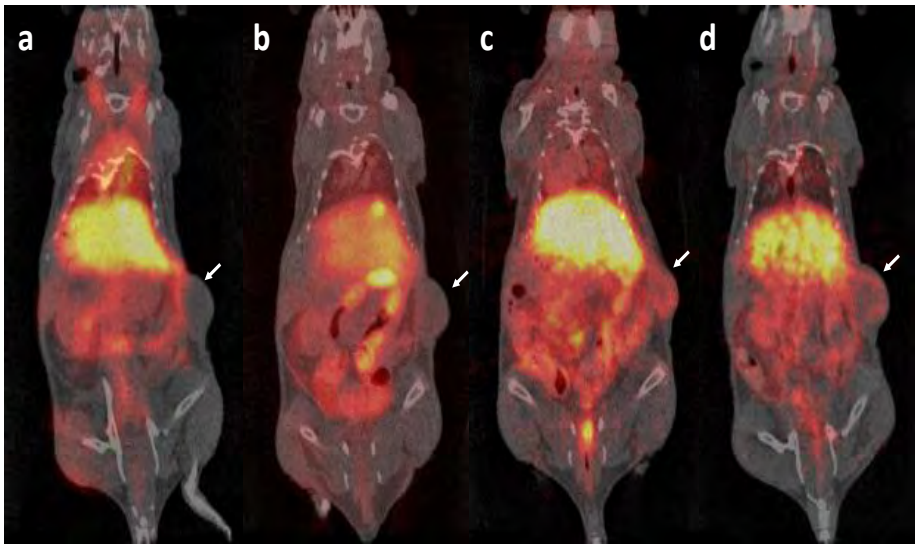

Figura 3. mágenes PET (vistas coronales) representativas, obtenidas a las 1 (a), 4 (b), 24 (c) y 48 (d) horas después de la administración de GNRs marcados con ^{64}Cu, en un modelo animal de ratón generado por inoculación subcutánea de células MKN-45. Las imágenes PET son proyecciones de máxima intensidad, y se muestran corregistradas con cortes representativos de imágenes CT correspondientes al mismo animal, para facilitar la localización de la señal radiactiva. La posición del tumor se indica con flechas blancas.

Chapter 1: General Introduction

1.1 The global burden of cancer

Cancer is a disease that occurs when cellular changes cause the uncontrolled growth and division of cells. According to the World Health Organization (WHO), cancer is still one of the leading causes of death worldwide, accounting for about 1 in every 6 deaths. In 2018, there were 18.1 million new cases of cancer diagnosed around the world and caused 9.6 million deaths [1]. By 2040, the global cancer incidence is expected to reach 27.5 million new cancer cases and 16.3 million cancer deaths, due to the aging of the population. Unfortunately, cancer is a heterogeneous disease, which makes treatment difficult. Currently, chemotherapy, radiotherapy, immunotherapy, and surgery are the main treatment options established in the clinical field. However, the efficacy of all these approaches is compromised by their risk to normal, healthy cells, and their potential to destroy the immune system. Therefore, a large body of cancer therapy research focuses on developing effective alternative treatments that can replace conventional therapies by improving therapeutic efficacy and reducing off-target side effects.

1.2 Boron Neutron Capture Therapy

1.2.1 General description

Boron neutron capture therapy (BNCT) is a promising radiotherapeutic modality to treat cancer. Gordon Locher was the first person to propose the concept of BNCT in 1936 [2]. This binary therapeutic modality is based on the neutron capture and nuclear fission reactions that occur when the non-radioactive stable atom boron-10 (~ 20% of natural boron) is irradiated with low energy thermal neutrons ($E < 0.5$ eV) or high energy epithermal neutrons (0.5 eV $< E < 10$ eV) to yield high energy alpha particles ($\alpha^{2+} = {}^{4}He^{2+}$) and recoil lithium ions (${}^{7}Li^{3+}$) (Figure 1.1). Alpha particles and ${}^{7}Li$ recoil ions have high linear energy transfer (LET) properties (150 keV μm^{-1} and 175 keV μm^{-1}, respectively) and path lengths in the range of 4 to 10 µm. Thanks to their strong ionization capacity, these particles are capable to create localized damage within the diameter of a single cell. Hence, if cancer cells selectively accumulate a sufficient amount of ${}^{10}B$ and are irradiated with thermal or epithermal neutrons, the ions produced as a consequence of the ${}^{10}B(n, \alpha, \gamma){}^{7}Li$ nuclear reaction trigger cell death, while sparing healthy surrounding tissue and decreasing unwanted off-target side effects (Figure 1.2).

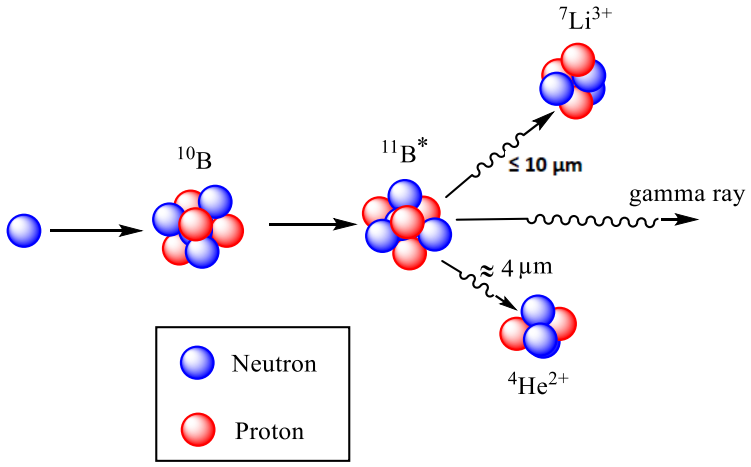

Figure 1.1. $^{10}B(n, \alpha, \gamma)^{7}Li$ nuclear reaction. The neutron is captured by the boron-10 atom, resulting in the formation of an unstable ^{11}B atom which rapidly undergoes a fission reaction with subsequent emission of one alpha particle, one recoil lithium ion and one gamma ray.

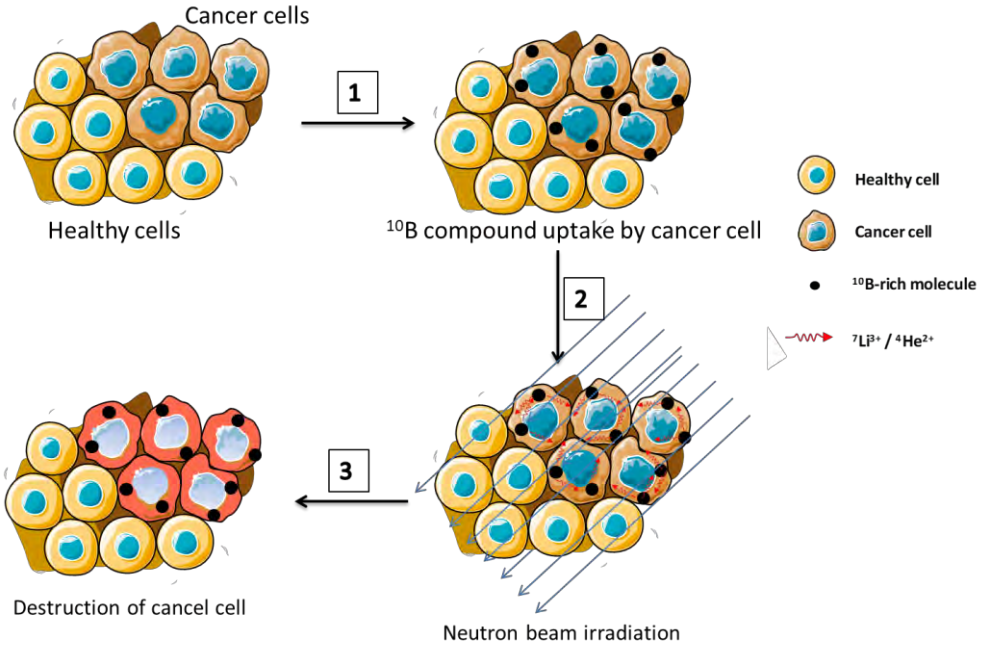

Figure 1.2. The principle behind BNCT: ^{10}B atoms preferentially accumulate in cancer cells (1). Neutron beam irradiation (2) produces the rapid nuclear reaction $^{10}B(n, \alpha, \gamma)^{7}Li$. Alpha particles and ^{7}Li ions have high linear energy transfer, triggering cell damage while sparing healthy surrounding tissue.

1.2.2 Boron delivery agents: Ideal properties

To find application in BNCT, drugs must fulfill certain requirements: (i) they should be able to selectively accumulate 20-35 µg of ^{10}B (natural abundance of ^{10}B 19.9%) per gram of tumor,

preferentially inside the cells, in order to guarantee that a sufficient amount of neutrons is absorbed producing the above mentioned nuclear reaction; (ii) they should show rapid clearance from blood and healthy tissues, in order to prevent damage in surrounding tissue during neutron irradiation; it is generally accepted that tumor-to-normal tissue (TtT) and tumor-to-blood (TtB) concentration ratios above 4-to-1 are sufficient to minimize off-target damage; (iii) they must exhibit low systemic toxicity since they are usually injected intravenously; and (iv) ideally, they should incorporate a means for external tracking in real time, in order to identify the optimal time window for neutron irradiation after administration of the drug. To date, many different drug candidates over a wide range of molecular modalities have been developed. A brief overview of the most relevant examples is provided below from an historical perspective.

1.2.3 First and second-generation boron delivery agents.

First compounds proposed as BNCT drug candidates were small molecules containing boron atoms in their structure. In the 1950s and early 1960s, BNCT clinical trials were conducted using boric acid and some of its derivatives. These chemical compounds were nonselective and had poor tumor retention. Hence, low TtT ratios could be achieved [3, 4]. In the 1960s, second-generation compounds covering a wide variety of small molecules emerged, being the two most prominent examples sodium mercaptoundecahydro-*closo*-dodecaborate ($Na_2B_{12}H_{11}SH$), commonly known as sodium borocaptate or BSH [5], and the boron-containing amino acid (L)-4-dihydroxy-borylphenylalanine [6], known as boronophenylalanine or BPA (Figure 1.3).

BSH, a polyhedral mercaptoboron molecule, was first applied to patients in 1968 [7] for the treatment of tumors in the central nervous system (CNS). Subsequent clinical trials using this boron-rich compound were focused in the treatment of patients with brain tumors [8-10], while BPA was also evaluated in patients suffering from malignant melanoma [11]. Despite the positive results, the major drawback of both BSH and BPA is the low selectivity and the significant inter-subject variability in tumor uptake, especially in brain tumors, as demonstrated by Goodman and co-workers. In a biodistribution and pharmacokinetic study involving 20 patients with high-grade gliomas [8], the authors found that boron concentrations varied among patients who received the same dose of BSH. Additionally, heterogeneous tumor accumulation was also observed. In spite of these drawbacks, BSH and BPA are still the only compounds used in the clinical field [12], suggesting the need for further investigation.

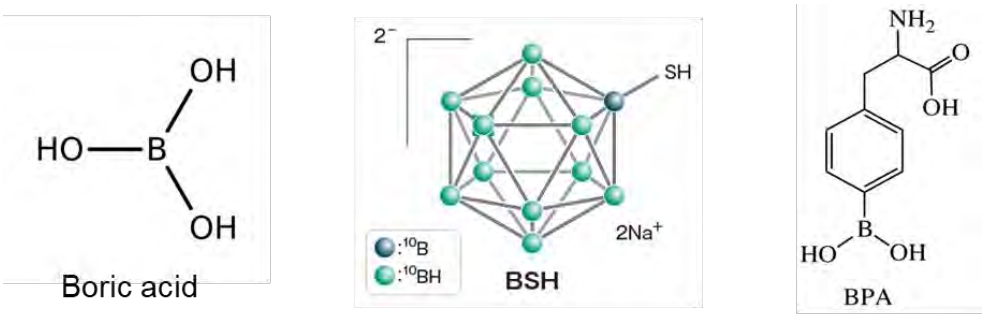

Figure 1.3. Chemical structures of boric acid (left), sodium borocaptate (BSH, middle) and boronophenylalanine (BPA, right).

1.2.4 *Third*-generation boron delivery agents.

Polyhedral heteroboranes, and more specifically dicarba-*closo*-dodecaboranes (commonly referred to as carboranes) with the general formula $C_2B_{10}H_{12}$, have been extensively used as boron-rich structures for the preparation of third-generation boron delivery agents. Carboranes exist as *ortho*-, *meta*-, and *para*-isomers (Figure 1.4), which differ in the relative positions of the carbon atoms in the cluster. The cobalt *bis*(dicarbollide) anion $[3,3'\text{-}Co(1,2\text{-}C_2B_9H_{11})_2]^-$ (Figure 1.4) is a stable complex in which the cobalt atom is held between two η^5-bonding $[C_2B_9H_{11}]^{2-}$ ligands derived from *nido*-carborane, which can be obtained by withdrawing one of the boron atoms adjacent to both C_c atoms in the *o*-carborane cluster [13].

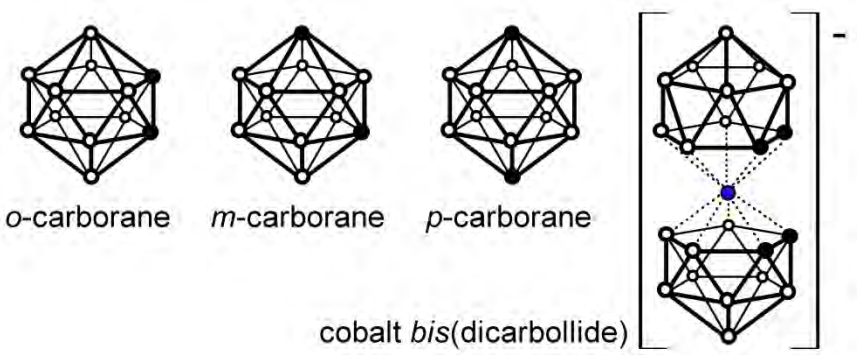

Figure 1.4. Chemical structure of *ortho*-, *meta*- and *para*-carborane and the cobalt *bis*(dicarbollide) anion. White dots denote B-H; black dots denote C-H; blue dot denotes Co(III).

Third-generation compounds mainly consist of a stable boron group or cluster connected via a hydrolytically stable linkage with a low molecular weight biomolecule, which is expected to aid

in tumor accumulation by acting as a vector. Commonly used vectors include amino acids [14, 15], peptides [16, 17], nucleosides [18], carbohydrates [19] and porphyrins [20, 21].

The use of boron-rich antibodies (Abs) has also been proposed, due to their exquisite selectivity towards the epitope. It is estimated that a boronated Ab should contain 10^3 ^{10}B atoms per Ab unit to provide a therapeutic dose to the tumor [22], but the incorporation of such a large amount of boron results in a significant loss of immunoreactivity and hence therapeutic efficacy might be compromised.

In spite of more than 50 years of efforts and considerable advances, a third generation compound suitable for application in the clinical practice has not been found. At his point, the emergence of nanotechnology opened new opportunities in the pursuit of effective and safe boron delivery agents.

1.2.5. Nanostructures for BNCT

Nanomedicine involves the use of nanoscale materials, e.g. nanoparticles (NPs), for the diagnosis, monitoring and/or treatment of diseases. Nanoparticles are generally defined as small particles with dimensions approximately from 1 to 100 nm according to the American Society for Testing and Materials (ASTM international 2006). NPs have unique physical and chemical properties compared to their bulk materials, including a large surface area-to-volume ratio, and exclusive optical and electrical properties [23]. Due to their small size, and depending on their composition and surface-functionalization, NPs can show high biocompatibility and can carry a significant amount of cargo. Hence, they have been proposed as drug delivery agents, especially in cancer applications because of their capacity to passively accumulate in tumor tissue. Indeed, tumor growth is accompanied by angiogenesis. In this process, rapid blood vessel formation leads to imperfect vessel walls with large fenestrations, which facilitate extravasation of large circulating entities (e.g. NPs) from the blood vessel to the tissue. This, together with a compromised lymphatic drainage, favors tumor accumulation of nanomaterials after intravenous administration. This process is known as enhanced permeability and retention or EPR [24] (Figure 1.5).

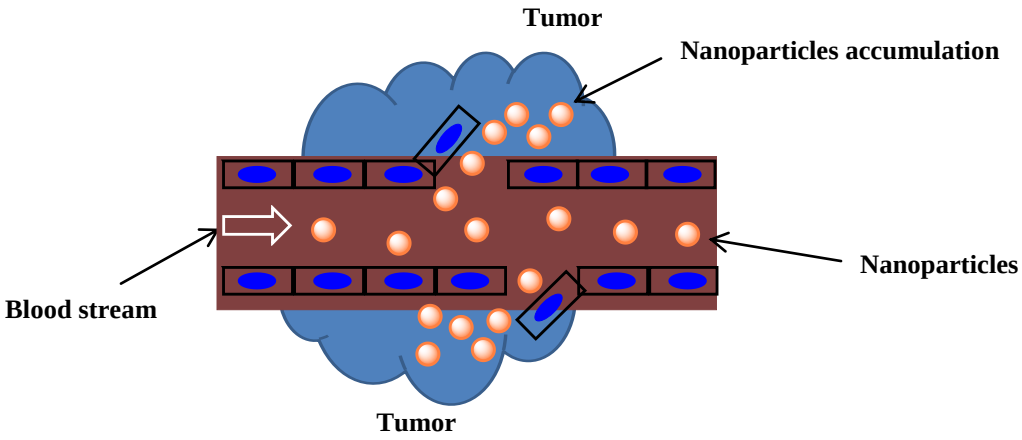

Figure 1.5. Schematic illustration showing nanoparticles accumulation in tumor due to enhanced permeability and retention (EPR) effect.

The passive targeting via enhanced permeability and retention effect has been widely exploited to accumulate different drugs in tumors, also in the context of BNCT. The clearest example on the use of nanosized materials to achieve high accumulation of boron in tumors are liposomes, which proven capable to accumulate large amounts of drugs in cancer cells [25-27]. Moreover, liposomes can be conveniently functionalized with antibodies, peptides, or other targeting moieties which may enhance retention in the tumor or cell internalization via specific interaction with receptors over-expressed in cancer cells [28, 29]. Similar to other drugs, BNCT agents can also be encapsulated inside liposomes, which passively accumulate in the tumor where the cargo is released via diffusion through the liposome or by degradation. This has been demonstrated in several works, showing promise for their translation to the clinical setting [30]. For example, Hawthorne and coworkers have designed a liposome system containing boron not only in the aqueous core but also in the lipid bilayer, which showed BNCT efficacy in a mouse model of mammary adenocarcinoma [31] (Figure 1.6a).

Other nanosystems have been employed to accumulate boron atoms in tumors, taking advantage of the EPR effect. One example is dendrimers, which thanks to their structure can be functionalized with a large number of boron cages. These can be attached to antibodies, in order to achieve high boron content without severely compromising the immunoreactivity of the antibody. In one of the most representative examples reported so far, the boronated

polyamidoamine dendrimer BD-C225 was linked with cetuximab (Figure 1.6b). This compound showed BNCT efficacy in EGFR gene-transfected rat glioma cells [32]

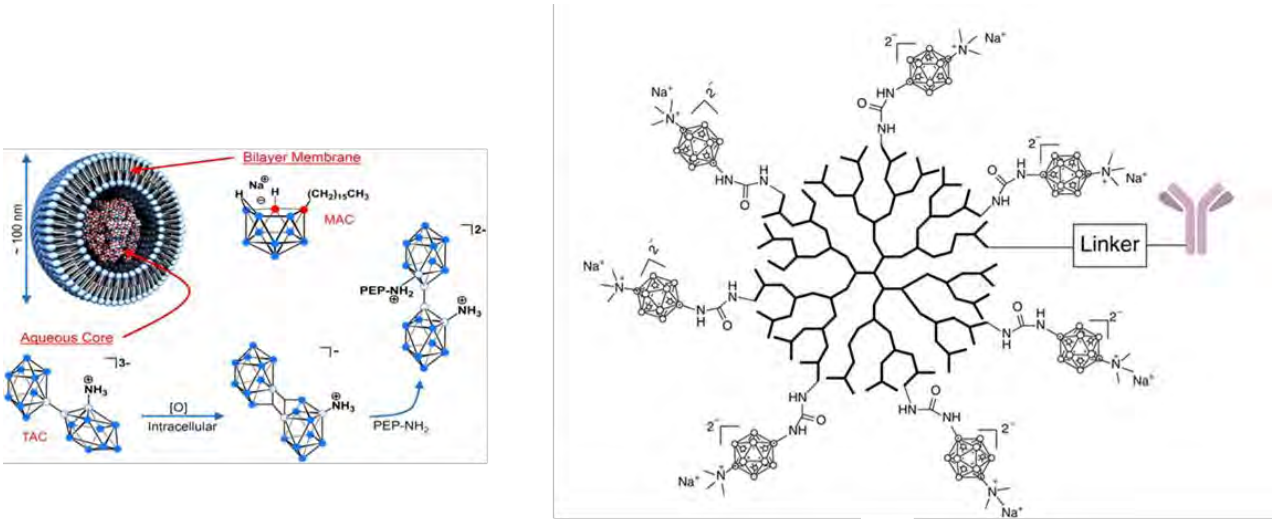

Figure 1.6. Schematic representation of boronated liposomes (a) and boronated polyamidoamine dendrimer (BD-C225) (b). Reprinted with permission from original sources [31] and [33].

Carbon nanotubes (CNTs) have also attracted great attention in biomedical applications due to their unique properties such as high thermal stability, magnetic properties, excellent conductivity, and superb chemical and mechanical properties [34]. CNTs are widely used in therapeutic drug delivery due to their high surface area and nanodimensionality, which allows them to adsorb or conjugate with a wide variety of therapeutic drugs. Additionally, surface engineered (i.e., functionalized) CNTs enhance their solubility and biocompatibility, resulting in low cytotoxic effects in therapeutic drug delivery [35]. In the context of BNCT, CNTs have been modified with *nido*-carborane units [36]. These water-soluble CNTs were tested in 3T3 fibroblasts and HL60 cells, where it was found that CNTs were able to transport large amount of functional groups into cells without apparent toxicity (Figure 1.7a).

Besides CNTs, boron nitride nanotubes (BNNTs) have also been proposed as BNCT drug candidates due to their inherent boron content. For example, transferrin coated boron nitride nanotubes (tf-BNNTs) were tested on human umbilical vein endothelial cells (HUVEC), as model of the BBB endothelium. Results revealed that transferrin played a key role during internalization of tf-BNNTs by HUVEC [37] (Figure 1.7b).

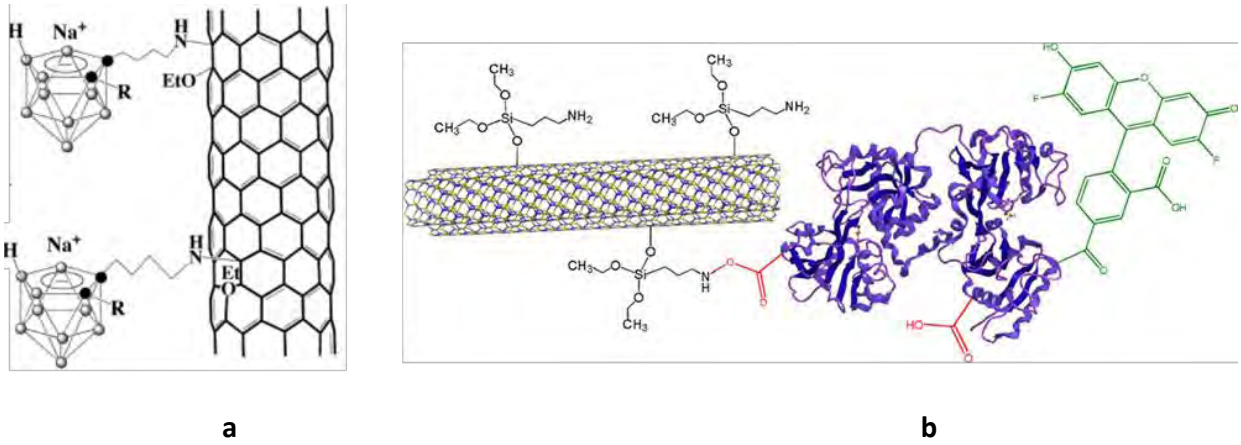

a b

Figure 1.7. Carbon nanotubes (CNTs) decorated with *nido*-carboranes (a) and transferrin conjugated BNNTs (b). Reprinted with permission from original sources [36] and [37]

Boron phosphate (BPO_4) has also been used for the preparation of nanosized BNCT agents. In one example of targeted approach, folic acid conjugated BPO_4 NPs were prepared with amine terminated BPO_4 and folic acid via condensation reaction [38]. However, these functionalized BPO_4 NPs showed high cytotoxicity in several cell lines.

Besides the above mentioned examples, other boron rich nanosystems have been prepared and eventually evaluated in the context of BNCT. These include magnetic nanoparticles [39], borosilicate nanoparticles [40], and polymeric NPs [41, 42].

1.2.6. Gold nanoparticles: potential boron carriers for BNCT

Gold nanoparticles (AuNPs) are extensively investigated NPs and have potential applications in medicine due to their unique physical and chemical properties, which significantly differ from the bulk material. The attractive features of AuNPs include their low level of toxicity, easy modification, biocompatibility, tunable stability and optical properties, and small dimensions. Additionally, they have straightforward functionalization chemistry through the well-known sulfur-gold bond formation. These unique features turn AuNPs into excellent candidates for a wide range of biomedical applications including drug delivery, cancer treatment, biomedical imaging, diagnosis and many others.

There are several ways of synthesizing AuNPs. They can be divided into physical, chemical and biological methods, although the most common approach is via chemical methods, which offer the possibility to precisely controlling the size and shape of the NPs. Indeed, AuNPs with different shapes can be synthesized including nanospheres, nanoshells, nanorods, nanoclusters, nanocages, and nanostars, among others [43-45] (Figure 1.8).

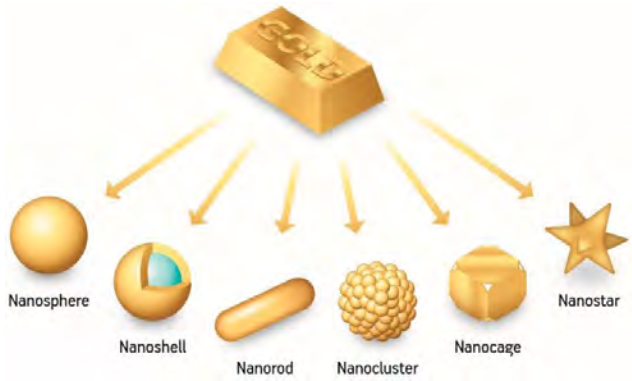

Figure 1.8. Different forms of gold nanoparticles (reprinted with permission from original source [45])

Among different forms of AuNPs, gold nanospheres are the simplest nanostructures of gold and can be synthesized by controlled reduction of an aqueous solution of $HAuCl_4$ using a reducing agent such as citrate ion (sodium salt of citric acid) [46]. Citrate ion acts both as a reducing agent and also as particle stabilizer. The size of gold nanospheres can be easily tuned by varying the amount of reducing agent and gold precursor. This method has greatly impacted the preparation of biomedical-grade AuNPs in the range of 20 nm. Brust *et al.* developed a one pot protocol to synthesize gold nanospheres in the range of 1.5 nm to ~6 nm. In this preparation, the aqueous $HAuCl_4$ solution is transferred to an organic phase (e.g. toluene) using tetraoctylammonium bromide (phase-transfer agent) and reduced with $NaBH_4$ in the presence of a thiol ligand (stabilizer) [47]. In this process, the thiol ligand/gold stoichiometry affects the size of the nanospheres. To get smaller and monodisperse gold nanospheres, faster addition of the reducing agent in a cooled solution to the thiol/gold precursors is mandatory. Later, this method was modified in different ways to achieve shape and size control, as well as to incorporate functionalities on the surface.

Gold nanospheres exhibit a strong absorption band in the visible region due to the collective oscillations of electrons in the conduction band in strong resonance with frequencies of visible

light. This phenomenon is called surface plasmon resonance (SPR) (Figure 1.9a, A). This effect induces a strong absorption of the light that depends on different properties including size, shape, surface functionality and aggregation state of the particles; when the size of the gold nanosphere is increased, the plasmon shifts towards higher wavelengths (Figure 1.9b, B).

Gold nanorods (GNRs), which are rod-shaped nanomaterials, have gained special attention in biological/biomedical fields, especially in the context of photothermal therapy, biosensing, imaging, and gene delivery for the treatment of cancer. Because of their rod-like shape, SPR spectrum exhibits two absorption bands: the first band stems from the visible region (around 520 nm) due to the interaction of light with the electrons from the diameter width, and the second one, red-shifted, stems from the NIR region (around 780 nm) due to the interaction of light with electrons from the length width of the nanorods (Figure 1.9b, B). The aspect ratio of GNRs affects the absorption spectra, with higher aspect ratios resulting in a shift towards higher wavelength values.

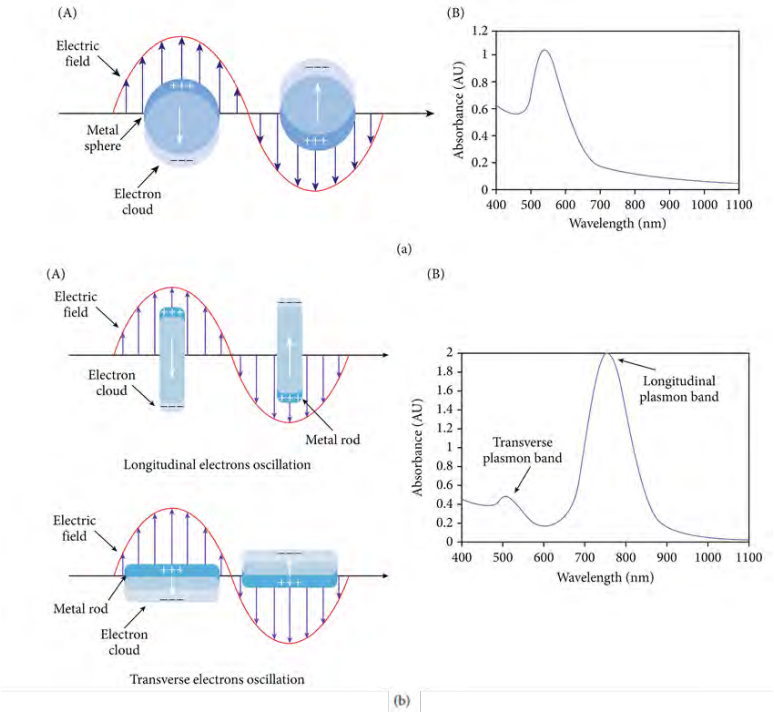

Figure 1.9. (a, A) Schematic representation of LSPR excitation for gold nanospheres; (a, B) typical LSPR absorption band of gold nanospheres; (b, A) Schematic illustration of LSPR excitation for GNRs and (b, B) LSPR absorption bands of GNRs: longitudinal and transverse plasmon bands corresponding to the electron oscillation along the long axis (b, A (top)) and the short axis (b, A (below)) of GNR, respectively (reprinted with permission from original source[48])

Several methods have been reported to synthesize GNRs, including both seed-mediated and seedless mediated methods [49, 50]. The seed-mediated growth method is the most widely used approach to synthesize GNRs with different aspect ratios by changing the stoichiometry of gold seeds and gold tetrachloride in the presence of the surfactant. In this method, a known amount of gold seeds are added to the growth solution which contains cetyltrimethylammonium bromide (CTAB) as the surfactant. The seeded crystals grow into GNRs with a certain aspect ratio with the help of surfactant. Recently, Ye *et al.* reported a new method for the synthesis of GNRs by seed-mediated growth method [51]. In this method, aromatic salicylates are used as an additive to improve the CTAB-micelle interaction, leading to a more stable structure, and resulting in the formation of monodispersed GNRs with high yield.

The use of gold-based nanomaterials in the context of BNCT is not widely exploited, although some examples can be encountered in the literature. In one of the first examples reported in which gold NPs were proposed as potential BNCT agents, Cioran *et al.* described the use of mercaptocarborane as a capping agent on the AuNPs via Au-thiol interaction (Figure 1.10a) [52]. These NPs displayed high cellular uptake due to the oxidation of NPs. However, these NPs showed high toxicity towards HeLa cells. In another study, *ortho*-carborane moieties were incorporated onto PEG-stabilized AuNPs through click chemistry. The addition of PEG resulted in water soluble functionalized AuNPs. The stability of these NPs and their capacity to accumulate in tumors, however, remains to be investigated (Figure 1.10b) [53].

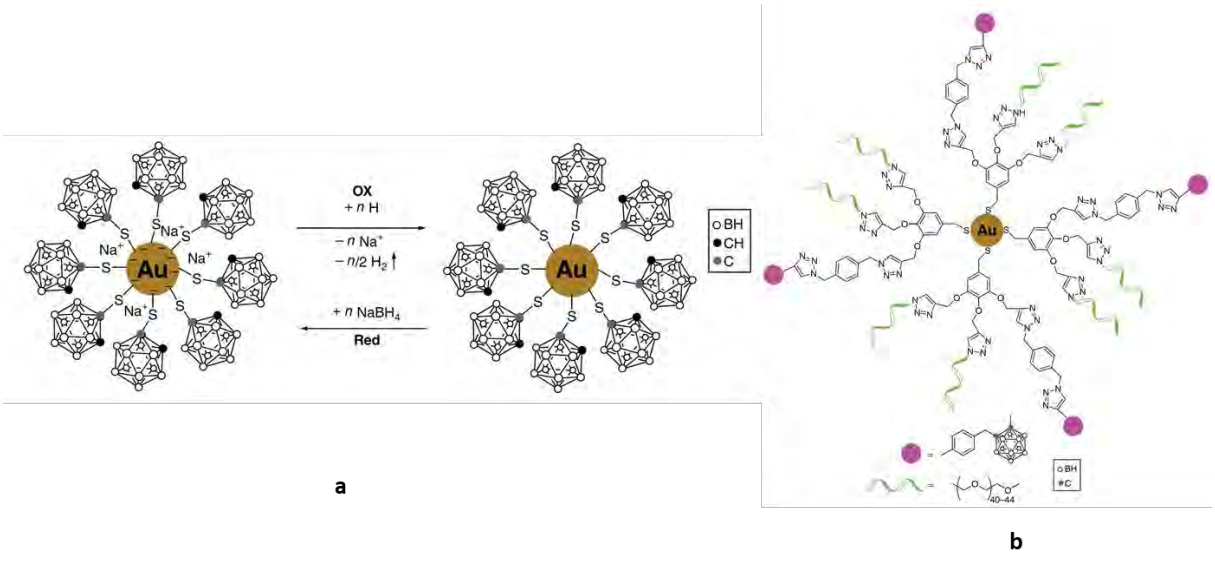

Figure 1.10. Mercaptoborane-capped AuNPs (a) and PEG-stabilized AuNPs incorporating *ortho*-carboranes (b) (reprinted with permission from original source [33])

1.3. Tracking NPs in vivo: Nuclear Imaging

As mentioned in the previous sections, nanoparticles (NPs) have been widely applied as drug delivery agents, especially in cancer applications where they can preferentially accumulate in the tumor thanks to the EPR effect. However, in most scenarios NPs are extremely difficult to detect and quantify once distributed in a biological system. Hence, the determination of the pharmacokinetic properties and biological fate of NPs becomes an extremely challenging task. Such determination is especially relevant in the context of BNCT, because neutron irradiation needs to be applied when the concentration of boron in the tumor is maximum, and the concentration of boron both in blood and in surrounding tissue are low, the latter to prevent off-target side effects. Hence, a suitable tool for the determination, *in vivo* and in real time, of the concentration of boron in at the whole body level is paramount in order to predict therapeutic efficacy and select the optimal time-window for neutron irradiation.

When using small experimental animals (e.g. rodents such as mice and rats), this information can be obtained after animal sacrifice by classical chemical analysis of the different organs to identify elements or molecules from the nanoparticles. The results can then be extrapolated to other animals to evaluate treatment efficacy. However, this requires animal sacrifice, and hence results have to be extrapolated from one group of individuals to other groups, as the biodistribution is not evaluated in a case-by-case basis. Additionally, natural or background levels of chemical components may be mistakenly considered as the signature of NPs presence. Finally, this approach cannot be translated to the clinical setting and is ethically questionable in large animal species.

One alternative to overcome this problem consists of labeling the NPs with radionuclides that can lead to their detection in biological systems by means of nuclear imaging techniques, this is, Positron Emission Tomography (PET) or Single Photon Emission Computerized Tomography (SPECT), which are *in vivo*, minimally invasive and very sensitive molecular imaging techniques. The most critical part in this approach is the incorporation of the radionuclide into the NP, and to date different strategies have been developed. The selection of the strategy for the radiolabeling depends on many different factors, e.g. the radionuclides available, the chemical composition of the NPs or the physical half-lives of the radionuclides. In the current PhD thesis, PET imaging has been used to assess the biodistribution of newly developed NPs and to

investigate tumor accumulation. Because of this, a brief introduction covering the principles of nuclear imaging and PET in particular are included below. A brief description of the radionuclides used in the context of the PhD thesis and the most common labeling strategies applied with those radionuclides is also included.

1.3.1. Positron emission tomography

Nuclear imaging techniques rely on the administration of small amounts of radioactive materials called radiotracers or radiopharmaceuticals, i.e., a compound labeled with a positron or gamma-emitting radionuclide. When a positron or gamma-emitter disintegrates, high energy gamma rays are ultimately generated. Gamma rays can travel through biological tissues without suffering significant scatter or attenuation. These gamma rays (or high energy photons) can be detected by specific equipment in such way that the original concentration of the radiotracer can be accurately quantified using specific tomographic reconstruction algorithms. Positron emission tomography (PET), single photon emission computed tomography (SPECT) and planar scintigraphy are nuclear imaging techniques. Nowadays, these techniques are available in combination with anatomical imaging such as computerized tomography (CT) or magnetic resonance imaging (MRI).

Positron emission tomography (PET) is the most sensitive nuclear imaging technique. This technique relies on the detection of the coincident high energy gamma rays (or high energy photons) resulting from the emission of a positron emitting radiotracer. Typical positron emitters used in the biomedical field include Fluorine-18, Carbon-11, Nitrogen-13, Oxygen-15, Galium-68, Copper-64, Zirconium-89 and Iodine-124.

In positron emission tomography, a PET radiotracer (any molecule labeled with a positron emitter) is administered to the subject under investigation. The spontaneous radioactive decay of a positron emitter produces a positron, which travels a certain distance (positron range; typically a few millimeters in water) to finally annihilate with the electron of a surrounding atom. As a result of the annihilation process, two gamma photons (511 keV each) are emitted in opposite direction (Figure 1.11). These high energy gamma rays can travel though biological tissues without suffering significant attenuation or scattering effects. Hence, they can be detected by an external ring of detectors (placed around the investigated subject) as coincident events. When two detectors detect two gamma rays simultaneously, a line of response is generated, so as the

disintegration took place somewhere within this line. The detection of hundreds of thousands of coincident events permits the accurate reconstruction of three-dimensional images that contain information about the spatiotemporal distribution of the radiotracer within the organism.

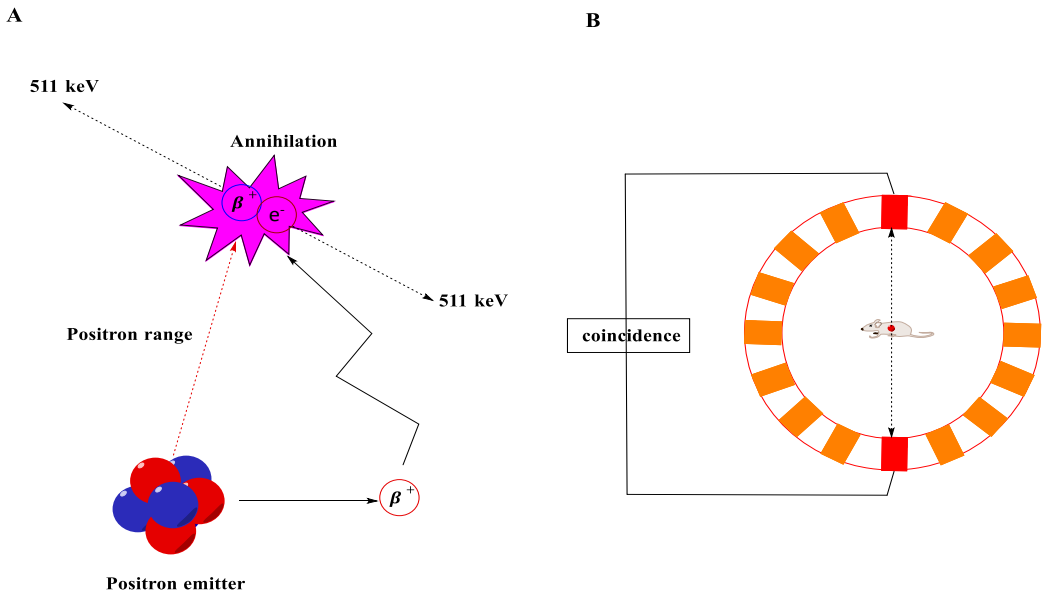

Figure 1.11. Schematic representation of the detection of photons using PET. (A) The positron travels a certain distance (positron range) and annihilates with an electron, resulting in the emission of two gamma rays in opposite direction; (B) the two gamma rays resulting from the annihilation are detected as a coincidence event by two detectors. Hence, a line of response is defined.

In order to get high quality PET images, the selection of the right positron emitter is paramount. In table 1.1, half-life values (time required to decrease the number of radioactive atoms to one half) and the energies of the emitted positrons for the most widely used PET radionuclides in the biomedical field are shown. Both half-life and energy of the emitted positron are indeed key factors to be considered.

The energy of the positron defines the positron range. The longer the positron range is, the higher the distance between the location of the disintegration event and the location of the annihilation. Hence, larger positron energy values usually result in lower resolution images. The other key parameter is physical half-life of the radionuclide, as this should match the biological half-life of the molecule to be investigated, in our case the NPs. If the physical half-life of the radionuclide is too short, NP tracking will be only possible during a short period of time after injection (4-5 half-lives), and hence the biological process will be only partially investigated. If the half-life is too

long, the investigated subject will be submitted to a higher radiation dose and waste disposal will be more costly.

Table 1.1. Physical properties (half-life and positron energy) of the most commonly used positron emitters in biomedicine.

Isotope	Half-Life	ß$^+$ Energy$_{max}$ (ß$^+$ fraction)
^{18}F	109.8 min	0.63 MeV (0.97)
^{11}C	20.4 min	0.96 MeV (1.00)
^{13}N	9.97 min	1.20 MeV (1.00)
^{15}O	122 sec	1.73 MeV (1.00)
^{68}Ga	67.7 min	1.89 MeV (0.89)
^{64}Cu	12.7 hours	0.66 MeV (0.18)
^{89}Zr	78.4 h	0.90 MeV (0.23)
^{124}I	4.18 days	2.14 MeV (0.23)

1.3.2. Positron emitters for NP labeling

When dealing with NPs, as they show long residence time in the body, long-lived radionuclides are perceived to be appropriate. Among the most commonly used positron emitters (see Table 1.1), mainly Copper-64 (^{64}Cu), Iodine-124 (^{124}I) and Zirconium-89 (^{89}Zr) have appropriate physical half-lives for the purpose. In this PhD thesis, Copper-64 and Iodine-124 have been used for radiolabeling the nanosystems. Therefore, the preparation methods, main properties and radiolabeling strategies concerning these radionuclides are briefly presented below.

Copper-64

Copper-64 (^{64}Cu) has a physical half-life of 12.7 h, which enables *in vivo* tracking of the labeled entity over a period of a few days. ^{64}Cu is effectively produced by both reactor- and accelerator-based methods. Reactor based methods usually entail the irradiation of materials with thermal or fast neutrons. Thermal neutrons have relatively low energy; in low energy neutron irradiation processes, the target (irradiated) material is of the same element as the product radionuclide; therefore, low-specific activity radionuclides are obtained. ^{64}Cu, for example, can be produced by irradiation of stable ^{63}Cu (69.1% natural abundance) with thermal neutrons via the ^{63}Cu(n,γ)^{64}Cu nuclear reaction. However, if this approach is used, ^{64}Cu will be "diluted" with the starting ^{63}Cu. Both isotopes cannot be separated, and hence low specific activity of the radionuclide is obtained.

This implies certain limitations, although discussion is beyond the scope of this thesis. For the production of high-specific activity ^{64}Cu, fast neutrons can be used. Unlike a thermal neutron, a highly energetic neutron has sufficient energy to eject a particle from the target nucleus, and the irradiated material can undergo (n,p) reactions. Thus, ^{64}Cu can be efficiently produced from ^{64}Zn via the ^{64}Zn(n,p)^{64}Cu nuclear reaction [54]. The main drawback of this methodology arises from the fact that fast neutron reactions using reactor neutrons are always accompanied by thermal neutron reactions, which may produce significant quantities of undesirable impurities.

Alternatively, ^{64}Cu can be effectively produced using biomedical cyclotrons via the ^{64}Ni(p,n)^{64}Cu nuclear reaction [55]. For the production, enriched ^{64}Ni is electroplated on to a gold disk and is irradiated with 14-16 MeV protons. After irradiation, the target material is dissolved in concentrated HCl and the solution is passed through an ion exchange column with different acid concentrations to separate ^{64}Cu from the target nickel and other impurities. The enriched ^{64}Ni can be successfully recovered and used for subsequent production and labeling experiments.

Despite the half-life of copper-64 is appropriate to investigate chemical species with long residence time in the organism, its decay scheme is far from optimal for PET studies. ^{64}Cu decays by β^- emission to the ground state of ^{64}Zn (β^- = 38.48 %) and by β^+ emission to ^{64}Ni (β^+ = 17.52 %) with 43.8 % electron capture (EC) (Figure 1.12) [56]. The positron-branch makes it a useful candidate for diagnostic imaging, while the beta-minus branch along with the emission of Auger electrons following electron-capture decay make it an attractive candidate also for therapy. However, the low positron branching is a limitation when used exclusively for imaging purposes, as almost 85% of the radioactive decay is not detected by the PET camera.

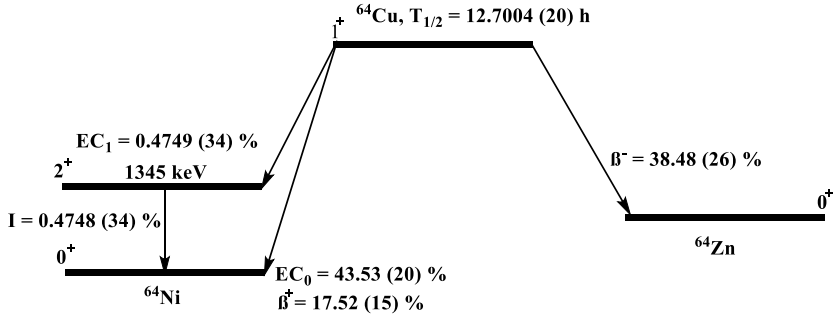

Figure 1.12. ^{64}Cu decay scheme (adapted from [57])

Copper is a thoroughly explored element with well-known coordination chemistry. Because of this, the most traditional approach to attach ^{64}Cu to NPs is via a metal chelator. In this traditional radiolabeling approach, ^{64}Cu is conjugated to the surface of NPs through macrocyclic chelators such as 1,4,7,10-tetraazacyclododecane-1,4,7,10-tetraacetic acid (DOTA), previously attached via covalent bonds to the surface of the NP. Although this approach has the advantage that the radiolabeling is carried out at the very late stage of the process, thus minimizing radiation exposure and loss of radioactivity due to radioactive decay, it also has a few disadvantages, including the possible detachment of radiometal from the complex, that may lead to misinterpretation of the images [58], and the modification of the surface properties of the nanoparticle. As an lternative with particular application to gold NPs, Zhao *et al.* recently reported a chelator-free ^{64}Cu radiolabeling strategy for gold nanoparticles via formation of an Au-^{64}Cu alloy [59]. They were able to radiolabel the AuNPs and investigate the capability of the resulting nanosystems to accumulate in the tumor in a mouse breast cancer model using a PET/CT. This labeling protocol results in the formation of highly stable labeled NPs, paving the way towards reliable *in vivo* evaluation of gold NPs using PET imaging.

Iodine-124

Iodine 124 (^{124}I) is a positron emitter with a long half-life (4.17 days) playing an important role in nuclear medicine for long-term clinical and PET studies. ^{124}I can be produced using different nuclear reactions. Generally, ^{124}I is produced in solid targets. The most widely used strategy is the irradiation of enriched ^{124}Te via the ^{124}Te(p,n)^{124}I or the ^{124}Te(d,2n)^{124}I nuclear reactions [60]. The irradiated material is tellurium or tellurium oxide, and ^{124}I is recovered easily from the irradiated material by dry distillation, or by dissolution of the target in oxidizing alkaline medium followed by reduction of tellurium and iodine and purification using solid phase extraction.

Iodine-124 has complex radioactive decay scheme (Figure 1.13) [61], which includes several high-energy gamma emissions (0.603 MeV, 63.0% abundance) and high energy positron emission (E_{pmax} = 2.14 MeV, 23% abundance). As in the case of ^{64}Cu, the emission spectrum is not optimal for application in PET imaging. However, due to its long half-life, it finds application when the user of more convenient radionuclides (from an emission spectrum point of view) cannot be applied.

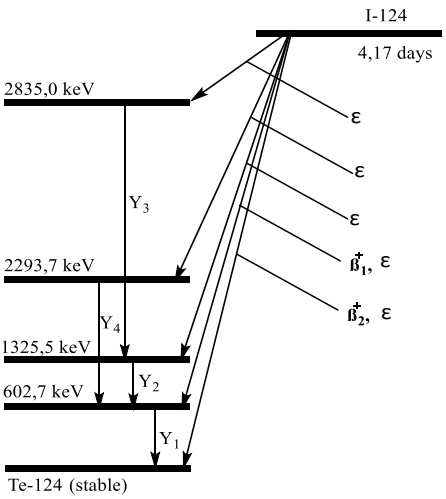

Figure 1.13. Simplified decay scheme of ^{124}I (adapted from [61])

In general terms, radiolabeling with ^{124}I can be approached using three main synthetic routes: (i) direct incorporation into activated aromatic rings by electrophilic substitution using the anionic species of the radionuclide (I^-) in the presence of oxidizing reagents, e.g. chloramine-T or *N*-chloro tosylamide [62]. In this chemical reaction, iodide in oxidation state −1 is oxidized to form a reactive electrophilic species in the oxidation state +1, which simply substitutes an hydrogen atom on aromatic rings containing electron-donating groups. The method is simple and usually high yields are obtained, although the reaction conditions may compromise the stability of the chemical entity to be labeled. Iodogen (1,3,4,6-tetrachloro-3α,6α-diphenyl glycoluril) is another alternative oxidizing agent [63], which was developed to conduct the reaction under milder conditions to prevent the damage of labeled molecules by oxidation. This strategy is widely applied to the molecules like proteins and antibodies containing tyrosine (or histidine) residues; (ii) the covalent attachment of pre-labeled prosthetic groups to the biomolecule. The most common conjugation reagent is N-succinimidyl 3-(4-hydroxyphenyl) propionate (Bolton–Hunter reagent) [64], which readily reacts with primary amines to form the corresponding amides; and (iii) nucleophilic substitution reaction using radioiodine to replace a stable iodine atom (isotopic exchange reaction) in the molecule under investigation [65]. In this isotopic exchange reaction, both starting material and radiolabeled molecule have the same chemical structure, and hence low molar activity values are achieved.

The three methodologies briefly described above have been extremely useful for the radiolabeling of chemical entities over a wide range of molecular modalities, ranging from small

molecules to large proteins and antibodies. In the context of NPs, another strategy has been developed, which has been very useful in the context of this PhD thesis. This methodology is based on the well-known affinity of iodide towards gold. The relative binding strengths of gold halide ions are in the order of I > Br > Cl. Iodine has a high affinity for AuNPs via chemisorption to the particle surface, and hence iodine labeling on gold surface can be achieved quickly and efficiently by simply incubating the nanoparticles with the radioactive anion. This strategy has been exploited using different radioisotopes of iodine, including ^{125}I [66], and ^{131}I [67]. However, to the best of our knowledge, this strategy has not been applied so far to radiolabeling of NPs using the positron emitter ^{124}I.

1.4. References

1. Bray F, Ferlay J, Soerjomataram I, Siegel RL, Torre LA, Jemal A. Global cancer statistics 2018: GLOBOCAN estimates of incidence and mortality worldwide for 36 cancers in 185 countries. *CA: A Cancer Journal for Clinicians*. **2018**;68(6):394-424.

2. Locher GL. Biological effects and therapeutic possibilities of neutrons. *American Journal of Roentgenology Radium Therapy and Nuclear Medicine*. **1936**;36(1):1-13.

3. Farr LE, Sweet WH, Robertson JS, Foster CG, Locksley HB, Sutherland DL, Mendelsohn ML, Stickley EE. Neutron capture therapy with boron in the treatment of glioblastoma multiforme. *The American journal of roentgenology, radium therapy, and nuclear medicine*. **1954**;71(2):279-93.

4. Godwin JT, Farr LE, Sweet WH, Robertson JS. Pathological study of eight patients with glioblastoma multiforme treated by neutroncapture therapy using boron 10. *Cancer*. **1955**;8(3):601-15.

5. Soloway AH, Hatanaka H, Davis MA. Penetration of Brain and Brain Tumor. VII. Tumor-Binding Sulfhydryl Boron Compounds. *Journal of Medicinal Chemistry*. **1967**;10(4):714-7.

6. Snyder HR, Reedy AJ, Lennarz WJ. Synthesis of Aromatic Boronic Acids. Aldehydo Boronic Acids and a Boronic Acid Analog of Tyrosine. *J Am Chem Soc*. **1958**;80(4):835-8.

7. Hatanaka H. A revised boron-neutron capture therapy for malignant brain tumors - II. Interim clinical result with the patients excluding previous treatments. *J Neurol*. **1975**;209(2):81-94.

8. Goodman JH, Yang W, Barth RF, Gao Z, Boesel CP, Staubus AE, Gupta N, Gahbauer RA, Adams DM, Gibson CR, Ferketich AK, Moeschberger ML, Soloway AH, Carpenter DE, Albertson BJ, Bauer WF, Zhang MZ, Wang CC. Boron neutron, capture therapy of brain tumors: Biodistribution, pharmacokinetics, and radiation dosimetry of sodium borocaptate in patients with gliomas. *Neurosurgery*. **2000**;47(3):608-22.

9. Hideghéty K, Sauerwein W, Wittig A, Götz C, Paquis P, Grochulla F, Haselsberger K, Wolbers J, Moss R, Huiskamp R, Frankhauser H, De Vries M, Gabel D. Tissue uptake of BSH in patients with glioblastoma in the EORTC 11961 phase I BNCT trial. *J Neurooncol*. **2003**;62(1-2):145-56.

10. Katalin Hideghéty WS, Andrea Wittig, Claudia Götz, Philippe Paquis, Frank Grochulla, Klaus Haselsberger, John Wolbers, Ray Moss, Rene Huiskamp, Heinz Fankhauser, Martin de Vries & Detlef Gabel. Tissue uptake of BSH in patients with glioblastoma in the EORTC 11961 phase I BNCT trial. *J Neuro-Oncol* **2003**;62:145-56.

11. Mishima Y, Ichihashi M, Hatta S, Honda C, Yamamura K, Nakagawa T, Obara H, Shirakawa J, Hiratsuka J, Taniyama K, Tanaka C, Kanda K, Kobayashi T, Sato T, Ishida MR, Ujeno Y, Takahashi M, Abe M, Nozaki T. First human clinical trial of melanoma neutron capture. Diagnosis and therapy. *Strahlenther Onkol*. **1989**;165(2-3):251-4.

12. Hu K, Yang Z, Zhang L, Xie L, Wang L, Xu H, Josephson L, Liang SH, Zhang MR. Boron agents for neutron capture therapy. *Coord Chem Rev*. **2020**;405.

13. Hawthorne MF, Young DC, Wegner PA. Carbametallic Boron Hydride Derivatives. I. Apparent Analogs of Ferrocene and Ferricinium Ion. *J Am Chem Soc*. **1965**;87(8):1818-9.

14. He T, Musah RA. Evaluation of the Potential of 2-Amino-3-(1,7-dicarba- closo-dodecaboranyl-1-thio)propanoic acid as a boron neutron capture therapy agent. *ACS Omega*. **2019**;4(2):3820-6.

15. Li J, Shi Y, Zhang Z, Liu H, Lang L, Liu T, Chen X, Liu Z. A Metabolically Stable Boron-Derived Tyrosine Serves as a Theranostic Agent for Positron Emission Tomography Guided Boron Neutron Capture Therapy. *Bioconjug Chem*. **2019**;30(11):2870-8.

16. Hoppenz P, Els-Heindl S, Kellert M, Kuhnert R, Saretz S, Lerchen HG, Köbberling J, Riedl B, Hey-Hawkins E, Beck-Sickinger AG. A Selective Carborane-Functionalized Gastrin-Releasing Peptide Receptor Agonist as Boron Delivery Agent for Boron Neutron Capture Therapy. *J Org Chem*. **2020**.

17. Worm DJ, Hoppenz P, Els-Heindl S, Kellert M, Kuhnert R, Saretz S, Köbberling J, Riedl B, Hey-Hawkins E, Beck-Sickinger AG. Selective Neuropeptide y Conjugates with Maximized Carborane Loading as Promising Boron Delivery Agents for Boron Neutron Capture Therapy. *J Med Chem*. **2019**.

18. Lesnikowski ZJ. Nucleoside-boron cluster conjugates - Beyond pyrimidine nucleosides and carboranes. *J Organomet Chem*. **2009**;694(11):1771-5.

19. Satapathy R, Dash BP, Mahanta CS, Swain BR, Jena BB, Hosmane NS. Glycoconjugates of polyhedral boron clusters Dedicated to Professor Russell Grimes on the occasion of his 80th birthday. *J Organomet Chem*. **2015**;798:13-23.

20. Ol'Shevskaya VA, Zaitsev AV, Kalinin VN, Shtil AA. Synthesis and antitumor activity of novel tetrakis[4-(closo-carboranylthio)tetrafluorophenyl]porphyrins. *Russ Chem Bull*. **2014**;63(10):2383-7.

21. Vicente MGH, Wickramasinghe A, Nurco DJ, Wang HJH, Nawrocky MM, Makar MS, Miura M. Synthesis, toxicity and biodistribution of two 5,15-di[3,5-(nido-carboranylmethyl)phenyl]porphyrins in EMT-6 tumor bearing mice. *Bioorganic & medicinal chemistry*. **2003**;11(14):3101-8.

22. Alam F, Soloway AH, Barth RF, Mafune N, Adams DM, Knoth WH. Boron Neutron Capture Therapy: Linkage of a Boronated Macromolecule to Monoclonal Antibodies Directed against Tumor-Associated Antigens. *J Med Chem*. **1989**;32(10):2326-30.

23. Bao G, Mitragotri S, Tong S. Multifunctional nanoparticles for drug delivery and molecular imaging. Annu Rev Biomed Eng2013. p. 253-82.

24. Jasim A, Abdelghany S, Greish K. Current Update on the Role of Enhanced Permeability and Retention Effect in Cancer Nanomedicine. Nanotechnology-Based Approaches for Targeting and Delivery of Drugs and Genes2017. p. 62-109.

25. Gifford I, Vreeland W, Grdanovska S, Burgett E, Kalinich J, Vergara V, Wang CKC, Maimon E, Poster D, Al-Sheikhly M. Liposome-based delivery of a boron-containing cholesteryl ester for high-LET particle-induced damage of prostate cancer cells: A boron neutron capture therapy study. *Int J Radiat Biol*. **2014**;90(6):480-5.

26. Lee W, Sarkar S, Ahn H, Kim JY, Lee YJ, Chang Y, Yoo J. PEGylated liposome encapsulating nido-carborane showed significant tumor suppression in boron neutron capture therapy (BNCT). *Biochem Biophys Res Commun*. **2020**;522(3):669-75.

27. Olusanya TOB, Calabrese G, Fatouros DG, Tsibouklis J, Smith JR. Liposome formulations of o-carborane for the boron neutron capture therapy of cancer. *Biophys Chem*. **2019**;247:25-33.

28. Gabizon A, Price DC, Huberty J, Bresalier RS. Effect of Liposome Composition and Other Factors on the Targeting of Liposomes to Experimental Tumors: Biodistribution and Imaging Studies. *Cancer Res*. **1990**;50(19):6371-8.

29. Saraf S, Jain A, Tiwari A, Verma A, Panda PK, Jain SK. Advances in liposomal drug delivery to cancer: An overview. *J Drug Deliv Sci Technol*. **2020**;56.

30. Pan XQ, Wang H, Shukla S, Sekido M, Adams DM, Tjarks W, Barth RF, Lee RJ. Boron-containing folate receptor-targeted liposomes as potential delivery agents for neutron capture therapy. *Bioconjug Chem*. **2002**;13(3):435-42.

31. Kueffer PJ, Maitz CA, Khan AA, Schuster SA, Shlyakhtina NI, Jalisatgi SS, Brockman JD, Nigg DW, Hawthorne MF. Boron neutron capture therapy demonstrated in mice bearing EMT6 tumors following selective delivery of boron by rationally designed liposomes. *Proceedings of the National Academy of Sciences of the United States of America*. **2013**;110(16):6512-7.

32. Barth RF, Yang W, Adams DM, Rotaru JH, Shukla S, Sekido M, Tjarks W, Fenstermaker RA, Ciesielski M, Nawrocky MM, Coderre JA. Molecular targeting of the epidermal growth factor receptor for neutron capture therapy of gliomas. *Cancer Res*. **2002**;62(11):3159-66.

33. Xuan S, Vicente MdGH. Recent Advances in Boron Delivery Agents for Boron Neutron Capture Therapy (BNCT). In: Hey-Hawkins E, Viñas C, editors. Boron-Based Compounds2018. p. 298-342.

34. Sharma P, Mehra NK, Jain K, Jain NK. Biomedical applications of carbon nanotubes: A critical review. *Curr Drug Del*. **2016**;13(6):796-817.

35. Bhirde AA, Patel V, Gavard J, Zhang G, Sousa AA, Masedunskas A, Leapman RD, Weigert R, Gutkind JS, Rusling JF. Targeted killing of cancer cells in vivo and in vitro with EGF-directed carbon nanotube-based drug delivery. *ACS Nano*. **2009**;3(2):307-16.

36. Zhu YH AT, Carpenter K, Maguire J, Hosmane N, Takagaki M. Substituted carborane-appended water soluble single-wall carbon nanotubes: new approach to boron neutron capture therapy drug delivery. *J Am Chem Soc*. **2005**;127:9875–80.

37. Ciofani G, Del Turco S, Genchi GG, D'Alessandro D, Basta G, Mattoli V. Transferrin-conjugated boron nitride nanotubes: Protein grafting, characterization, and interaction with human endothelial cells. *International Journal of Pharmaceutics*. **2012**;436(1-2):444-53.

38. Achilli C, Grandi S, Ciana A, Guidetti GF, Malara A, Abbonante V, Cansolino L, Tomasi C, Balduini A, Fagnoni M, Merli D, Mustarelli P, Canobbio I, Balduini C, Minetti G. Biocompatibility of functionalized boron phosphate (BPO<inf>4</inf>) nanoparticles for boron neutron capture therapy (BNCT) application. *Nanomedicine: Nanotechnology, Biology, and Medicine*. **2014**;10(3):589-97.

39. Oleshkevich E, Morancho A, Saha A, Galenkamp KMO, Grayston A, Crich SG, Alberti D, Protti N, Comella JX, Teixidor F, Rosell A, Viñas C. Combining magnetic nanoparticles and icosahedral boron clusters in biocompatible inorganic nanohybrids for cancer therapy. *Nanomedicine: Nanotechnology, Biology, and Medicine*. **2019**;20.

40. Grandi S, Spinella A, Tomasi C, Bruni G, Fagnoni M, Merli D, Mustarelli P, Guidetti GF, Achilli C, Balduini C. Synthesis and characterisation of functionalized borosilicate nanoparticles for boron neutron capture therapy applications. *Journal of Sol-Gel Science and Technology*. **2012**;64(2):358-66.

41. di Meo C, Panza L, Campo F, Capitani D, Mannina L, Banzato A, Rondina M, Rosato A, Crescenzi V. Novel types of carborane-carrier hyaluronan derivatives via "click chemistry". *Macromolecular Bioscience*. **2008**;8(7):670-81.

42. Xiong H, Zhou D, Qi Y, Zhang Z, Xie Z, Chen X, Jing X, Meng F, Huang Y. Doxorubicin-Loaded Carborane-Conjugated Polymeric Nanoparticles as Delivery System for Combination Cancer Therapy. *Biomacromolecules*. **2015**;16(12):3980-8.

43. Venditti I. Engineered gold-based nanomaterials: Morphologies and functionalities in biomedical applications. a mini review. *Bioengineering*. **2019**;6(2).

44. Yang X, Yang M, Pang B, Vara M, Xia Y. Gold Nanomaterials at Work in Biomedicine. *Chemical Reviews*. **2015**;115(19):10410-88.

45. De Freitas LF, Varca GHC, Batista JGS, Lugão AB. An overview of the synthesis of gold nanoparticles using radiation technologies. *Nanomaterials*. **2018**;8(11).

46. Turkevich J, Stevenson PC, Hillier J. A study of the nucleation and growth processes in the synthesis of colloidal gold. *Discussions of the Faraday Society*. **1951**;11:55-75.

47. Brust M, Walker M, Bethell D, Schiffrin DJ, Whyman R. Synthesis of thiol-derivatised gold nanoparticles in a two-phase liquid-liquid system. *Journal of the Chemical Society, Chemical Communications*. **1994**(7):801-2.

48. Meng L, Zhang J, Li H, Zhao W, Zhao T. Preparation and Progress in Application of Gold Nanorods. *Journal of Nanomaterials*. **2019**;2019.

49. Jana NR, Gearheart L, Murphy CJ. Wet chemical synthesis of high aspect ratio cylindrical gold nanorods. *Journal of Physical Chemistry B*. **2001**;105(19):4065-7.

50. Ali MRK, Snyder B, El-Sayed MA. Synthesis and optical properties of small Au nanorods using a seedless growth technique. *Langmuir*. **2012**;28(25):9807-15.

51. Ye X, Jin L, Caglayan H, Chen J, Xing G, Zheng C, Doan-Nguyen V, Kang Y, Engheta N, Kagan CR, Murray CB. Improved size-tunable synthesis of monodisperse gold nanorods through the use of aromatic additives. *ACS Nano*. **2012**;6(3):2804-17.

52. Cioran AM, Musteti AD, Teixidor F, Krpetić Z, Prior IA, He Q, Kiely CJ, Brust M, Viñas C. Mercaptocarborane-capped gold nanoparticles: Electron pools and ion traps with switchable hydrophilicity. *Journal of the American Chemical Society*. **2012**;134(1):212-21.

53. Li N, Zhao P, Salmon L, Ruiz J, Zabawa M, Hosmane NS, Astruc D. "Click" star-shaped and dendritic PEGylated gold nanoparticle-carborane assemblies. *Inorganic Chemistry*. **2013**;52(19):11146-55.

54. Zinn KR, Chaudhuri TR, Cheng TP, Steven Morris J, Meyer WA. Production of no-carrier-added ^{64}Cu from zinc metal irradiated under boron shielding. *Cancer*. **1994**;73(3 S):774-8.

55. Ohya T, Nagatsu K, Suzuki H, Fukada M, Minegishi K, Hanyu M, Fukumura T, Zhang MR. Efficient preparation of high-quality ^{64}Cu for routine use. *Nuclear Medicine and Biology*. **2016**;43(11):685-91.

56. Bé MM, Cassette P, Lépy MC, Amiot MN, Kossert K, Nähle OJ, Ott O, Wanke C, Dryak P, Ratel G, Sahagia M, Luca A, Antohe A, Johansson L, Keightley J, Pearce A. Standardization, decay data measurements and evaluation of ^{64}Cu. *Applied Radiation and Isotopes*. **2012**;70(9):1894-9.

57. Martín IG, Frigell J, Llop J, Marradi M. Radiolabelling of NPs using radiometals: ^{99m}Tc, ^{68}Ga, ^{67}Ga, ^{89}Zr, and ^{64}Cu. Isotopes in Nanoparticles: Fundamentals and Applications2016. p. 183-229.

58. Iceta LG, Gómez-Vallejo V, Koziorowski JM, Llop J. Radiochemical stability studies of radiolabelled nanoparticles. Isotopes in Nanoparticles: Fundamentals and Applications2016. p. 429-53.

59. Zhao Y, Sultan D, Detering L, Cho S, Sun G, Pierce R, Wooley KL, Liu Y. Copper-64-alloyed gold nanoparticles for cancer imaging: Improved radiolabel stability and diagnostic accuracy. *Angewandte Chemie - International Edition*. **2014**;53(1):156-9.

60. Lambrecht RM, Sajjad M, Qureshi MA, Al-Yanbawi SJ. Production of iodine-124. *Journal of Radioanalytical and Nuclear Chemistry Letters*. **1988**;127(2):143-50.

61. Preylowski V, Schlögl S, Schoenahl F, Jörg G, Samnick S, Buck AK, Lassmann M. Is the Image Quality of I-124-PET Impaired by an Automatic Correction of Prompt Gammas? *PLoS ONE*. **2013**;8(8).

62. Hunter WM, Greenwood FC. Preparation of iodine-131 labelled human growth hormone of high specific activity. *Nature*. **1962**;194(4827):495-6.

63. Fraker PJ, Speck Jr JC. Protein and cell membrane iodinations with a sparingly soluble chloroamide, 1,3,4,6-tetrachloro-3a,6a-diphenylglycoluril. *Biochemical and Biophysical Research Communications*. **1978**;80(4):849-57.

64. Bolton AE, Hunter WM. The labelling of proteins to high specific radioactivities by conjugation to a ^{125}I containing acylating agent. Application to the radioimmunoassay. *Biochemical Journal*. **1973**;133(3):529-38.

65. Wager KM, Jones GB. Radio-Iodination methods for the production of SPECT imaging agents. *Current Radiopharmaceuticals*. **2010**;3(1):37-45.

66. Walsh AA. Chemisorption of iodine-125 to gold nanoparticles allows for real-time quantitation and potential use in nanomedicine. *Journal of Nanoparticle Research*. **2017**;19(4).

67. Zhang Y, Yin L, Xia X, Hu F, Liu Q, Qin C, Lan X. Synthesis and bioevaluation of Iodine-131 directly labeled cyclic RGD-PEGylated gold nanorods for tumor-targeted imaging. *Contrast Media and Molecular Imaging*. **2017**;2017.

Chapter 2: Motivation and objectives

2.1. Motivation

This PhD thesis has been conducted in the Radiochemistry and Nuclear Imaging Group at CIC biomaGUNE, led by Dr. Llop. One of the main research lines of the group during the last years has been focused in merging the experience gained in boron chemistry and radiochemistry, with the ultimate goal of developing potential therapeutic agents with application in boron neutron capture therapy (BNCT), and evaluate their suitability in relevant animal models using *in vivo* imaging techniques, mainly positron emission tomography (PET) in combination with anatomical techniques, i.e. computerized tomography (CT).

Previous works performed by other PhD students in the group have focused on the development of small molecules containing boron clusters and labeled with positron emitters [1-5]. Despite some of these compounds could be successfully labeled, preliminary evaluation *in vivo* showed in most of the cases unfavorable pharmacokinetic properties.

Recently, and taking advantage of the knowledge gathered at CIC biomaGUNE in the area of nanotechnology, the Radiochemistry and Nuclear Imaging Group has progressively incorporated nanoparticles in the development of drug candidates for BNCT, often in collaboration with other groups within the institute. This PhD thesis is the first example in the group of gold nanoparticles (AuNPs) used as boron carriers.

The first approach (described in chapter 3) was the development of spherical AuNPs with a core diameter close to 20 nm (as we expected this to be an ideal particle size for tumor accumulation) functionalized simultaneously with Poly(ethylene glycol) methyl ether thiol and the inorganic, boron-based molecule cobalt *bis*(dicarbollide), [3,3'-Co(1,2-$C_2B_9H_{11})_2]^-$, commonly known as COSAN. The resulting multifunctionalized NPs were radiolabeled with ^{124}I to enable *in vivo* tracking. Additionally, and in order to investigate also the biological fate and stability of the NPs *in vivo*, the radiolabel was incorporated both at the core and at the shell of the NPs. Whole body imaging studies using PET demonstrated good stability of the NPs, although low accumulation was observed in the tumor when evaluated in a mouse xenograft model, generated by subcutaneous inoculation of HT 1080 (human fibrosarcoma) cells. Additionally, accumulation of radioactivity was observed in stomach and thyroid gland at long times after administration,

suggesting progressive release of the radiolabel. This work, which was recently published [6], suggests that: (i) particle size was not appropriate for tumor accumulation, as major accumulation was observed in the liver; and (ii) the labeling strategy should be improved.

In view of these previous results, we tackled the investigation of spherical particles with two different sizes, around 3 and 10 nm core size, respectively. Additionally, we modified the labeling strategy, by incorporating the radionuclide (in this case, ^{64}Cu) at the core of the NPs. We also decided to change the tumor model, and assayed a xenograft mouse model generated by subcutaneous administration of MKN45 (human gastrointestinal adenocarcenoma) cells. In this case, whole body imaging studies using PET demonstrated the increased capacity of the newly developed particles to accumulate in the tumor, with higher accumulation for the smaller NPs. Additionally, combination of PET studies with *ex vivo* inductively coupled plasma-mass spectrometry (ICP-MS) studies demonstrated good correlation, proving thus the stability of the label and the reliability of PET results. The manuscript corresponding to this work is currently under preparation.

In spite of the improved results, tumor accumulation was not sufficient to guarantee therapeutic efficacy. In view of this, we decided to investigate boron-rich gold-based nanosystems enabling dual therapeutic approaches, i.e. BNCT combined with photothermal therapy (chapter 5). With that aim, we developed and evaluated in the same tumor model gold nanorods (GNRs) again functionalized simultaneously with PEG and COSAN. The resulting multifunctionalized GNRs were radiolabeled with ^{64}Cu following a parallel strategy to that used in chapter 4. *In vivo* PET studies confirmed good tumor accumulation. Although not proven, the presence of boron-rich GNRs in the tumor should enable combined therapy. This work, which should prove efficient therapeutic effect, is currently ongoing in the research group, although the results have not been included in this PhD thesis.

2.2. Objectives

The main goal of the PhD thesis was to develop gold-based, boron-rich nanosystems as therapeutic agents suitable for BNCT. To achieve this ambitious goal, the following specific objectives were defined:

1. To synthesize, functionalize and characterize water soluble and biocompatible AuNPs containing PEG and boron-rich clusters with potential application in BNCT.
2. To evaluate cytotoxicity and cellular uptake of the multifunctionalized AuNPs in relevant cancer cell lines.
3. To develop the radiolabeling strategies for the incorporation of positron emitters in the nanoparticles to enable subsequent investigation *in vivo* using nuclear imaging techniques.
4. To evaluate stability and pharmacokinetic properties of the novel multifunctionalized AuNPs using positron emission tomography (PET) in relevant tumor models.

2.3. References

1. Gõmez-Vallejo V, Vázquez N, Gona KB, Puigivila M, González M, Sebastián ES, Martin A, Llop J. Synthesis and in vivo evaluation of ^{11}C-labeled (1,7-dicarba-closo-dodecaboran-1-yl)-N-{[(2S)-1-ethylpyrrolidin-2-yl]methyl} amide. *Journal of Labelled Compounds and Radiopharmaceuticals*. **2014**;57(4):209-14.

2. Gona KB, Gómez-Vallejo V, Padro D, Llop J. [^{18}F]Fluorination of o-carborane via nucleophilic substitution: Towards a versatile platform for the preparation of ^{18}F-labelled BNCT drug candidates. *Chemical Communications*. **2013**;49(98):11491-3.

3. Gona KB, Thota JLVNP, Baz Z, Gómez-Vallejo V, Llop J. Straightforward synthesis of radioiodinated C_c-substituted o-carboranes: Towards a versatile platform to enable the in vivo assessment of BNCT drug candidates. *Dalton Transactions*. **2015**;44(21):9915-20.

4. Gona KB, Thota JLVNP, Baz Z, Gómez-Vallejo V, Llop J. Synthesis and ^{11}C-radiolabelling of 2-carboranyl benzothiazoles. *Molecules*. **2015**;20(5):7495-508.

5. Gona KB, Zaulet A, Gómez-Vallejo V, Teixidor F, Llop J, Viñas C. COSAN as a molecular imaging platform: Synthesis and "in vivo" imaging. *Chemical Communications*. **2014**;50(77):11415-7.

6. Pulagam KR, Gona KB, Gómez-Vallejo V, Meijer J, Zilberfain C, Estrela-Lopis I, Baz Z, Cossío U, Llop J. Gold nanoparticles as boron carriers for boron neutron capture therapy: Synthesis, radiolabelling and in vivo evaluation. *Molecules*. **2019**;24(19).

Chapter 3: Gold nanoparticles as boron carriers for BNCT (I)

3.1. Introduction

As mentioned in the introductory section of this PhD thesis, boron neutron capture therapy (BNCT) is a binary radio-therapeutic modality for the treatment of different types of cancer, mainly high grade gliomas and head and neck cancers [1]. Historically, the delivery of a sufficient amount of ^{10}B atoms into tumor tissue ((~10^9 atoms/cell, tumor-to-blood and tumor-to-normal tissue boron concentration ratios >3), which is paramount for effective BNCT, has been one of the main limitations for the unconditional establishment of BNCT in the clinics. Indeed, despite decades of effort, only two agents are routinely used in BNCT clinical trials: sodium mercaptoundecahydro-closo-dodecaborate (BSH) and L-4-dihydroxyborylphenylalanine (BPA) [2]. Additionally, their use is quite limited due to the low tumor-to-blood and tumor-to-healthy tissue ^{10}B ratios achieved. As a consequence, there is an urgent need for the development of new therapeutic boron delivery systems.

The hurdle of optimal boron drug delivery has long been recognized in the BNCT community. Taking advantage of the recent developments in nanotechnology, different classes of nanomaterial-based drug delivery systems have been evaluated and positioned as promising boron carriers, as nanosystems can carry a large amount of boron atoms selectively to the tumor cells via enhanced permeability retention effect (EPR) (see chapter 1 for more details). Surprisingly, despite showing unique physical and chemical properties that include biocompatibility, low toxicity, and tunable surface functionalities, gold nanomaterials have been barely exploited in this context [3-5].

Among all gold nanosystems, spherical AuNPs have received considerable interest since their successful synthesis was first described in 1951 [6]. Most commonly used spherical AuNPs are in the range of few nm to 100 nanometers. Generally, non-PEGylated AuNPs are rapidly uptaken by the reticuloendothelial system (RES, currently known as the mononuclear phagocyte system, MPS) and are rapidly eliminated from blood circulation to the liver, spleen, lungs or bone marrow. Hence, they are not bioavailable anymore and tumor uptake is severely hampered. To overcome this problem, most gold nanostructures are functionalized with thiol-terminated polyethylene glycol (PEG), which is one of the most commonly used biopolymers to

functionalize the surface of AuNPs. Multiple studies have shown that the PEG polymer on AuNPs surface increases biological half-life by reducing the opsonization process (Figure 3.1), thus preventing uptake by macrophages, allowing the AuNPs to remain in the blood pool and accumulate in tumors through passive targeting [7, 8].

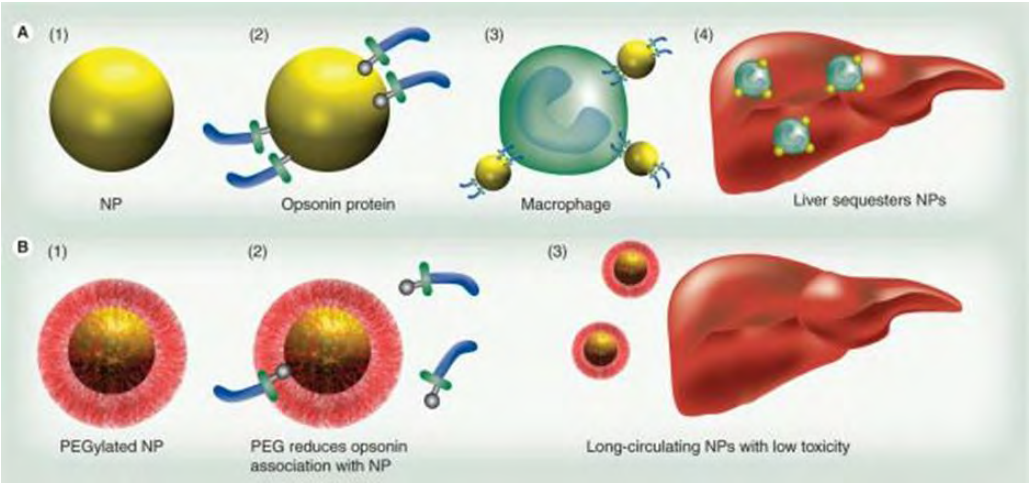

Figure 3.1. Polyethylene glycol (PEG) prevents uptake by the reticuloendothelial system. (A) Nanoparticles (1) are coated with opsonin proteins (2) and associate with macrophages (3) for transit to the liver (4). Macrophages stationary in the liver, known as Kupffer cells, also participate in nanoparticle scavenging; (B) coating nanoparticles with PEG (1) prevents opsonization (2), resulting in decreased liver accumulation (3) and increased availability of the nanoparticles for imaging or therapy (reprinted with permission from original source [9]).

As a first approach for the development of gold NP-based BNCT agents, we decided to work with spherical gold particles functionalized with PEG, the latter to achieve prolonged circulation time. As a boron source, we decided to incorporate a boron cluster. Indeed, boron clusters such as carboranes, metallacarboranes, and other polyhedral boron hydrides have been attached to biologically active molecules capable to selectively accumulate in tumor cells [10]. Among the different possibilities, we selected the cobalt *bis*(dicarbollide) anion $[3,3'\text{-}Co(1,2\text{-}C_2B_9H_{11})_2]^-$ (COSAN). COSAN and its derivatives have attracted considerable attention for the development of pharmaceutical agents due to their high thermal and chemical stability, rich boron content, and low toxicity. Due to their negative charge covering the whole molecule, COSAN derivatives exhibit both electrostatic interactions and non-bonding intermolecular interactions between its weakly polarized B-H and C-H bonds. Due to this dual nature, COSAN derivatives possess both hydrophobic and hydrophilic character, being soluble in both water and oils. These properties,

together with its rich derivative chemistry, turn COSAN derivatives into valuable building blocks for the preparation of boron-rich drugs with potential application in BNCT.

In this chapter, we discuss the preparation, characterization and evaluation of size and shape-tuned gold NPs functionalized simultaneously with Poly(ethylene glycol) methyl ether thiol and COSAN. To attach the COSAN cluster to the NPs, thiolated COSAN derivatives were prepared. The thiolated group was incorporated into one of the boron atoms of one of the $[C_2B_9H_{11}]^{2-}$ ligands using an inert spacer. Concretely, we prepared the cyclooxonium derivative using tetrahydropyran, which was subsequently used to produce the thiolated COSAN derivative, which was ultimately attached to PEG-stabilized AuNPs via thiol-gold chemistry. The resulting functionalized AuNPs were radiolabeled with ^{124}I to enable *in vivo* imaging using PET, using two different strategies; namely, the radiolabel was incorporated either on the surface of the gold core or covalently attached to the COSAN structure. To incorporate the radiolabel on the COSAN structure, a new COSAN derivative incorporating one iodine atom directly attached to one of the boron atoms of the cluster was synthesized, and successfully radiolabeled with ^{124}I via palladium catalyzed iodine exchange reaction. To incorporate the label on the gold core, chemisorption was used, as this strategy has proven efficient with other radioisotopes of iodine [11]. Finally, whole body imaging studies using Positron Emission Tomography (PET) were carried out in a mouse cancer model, generated by subcutaneous inoculation of HT 1080 (human fibrosarcoma) cells, in order to assess the *in vivo* stability of multifunctionalized AuNPs and their capability to accumulate in the tumor by passive targeting.

3.2. Objectives

The specific objectives of this chapter are:

1- To synthesize and characterize stable and biocompatible spherical AuNPs functionalized with PEG and COSAN.

2- To perform radiolabeling studies for the incorporation of positron emitters in the core and shell of the multifunctionalized AuNPs.

3- To evaluate pharmacokinetic properties of the novel multifunctionalized AuNPs using positron emission tomography (PET) in a human fibrosarcoma mouse tumor model.

3.3. Results and discussion

3.3.1. Synthesis of COSAN derivatives

The first step for the preparation of the multifunctionalized gold NPs was the development of the appropriate COSAN derivatives. First, COSAN derivatives bearing a thiol group were synthesized following a previously published methodology [12] with minor modifications (Scheme 3.1).

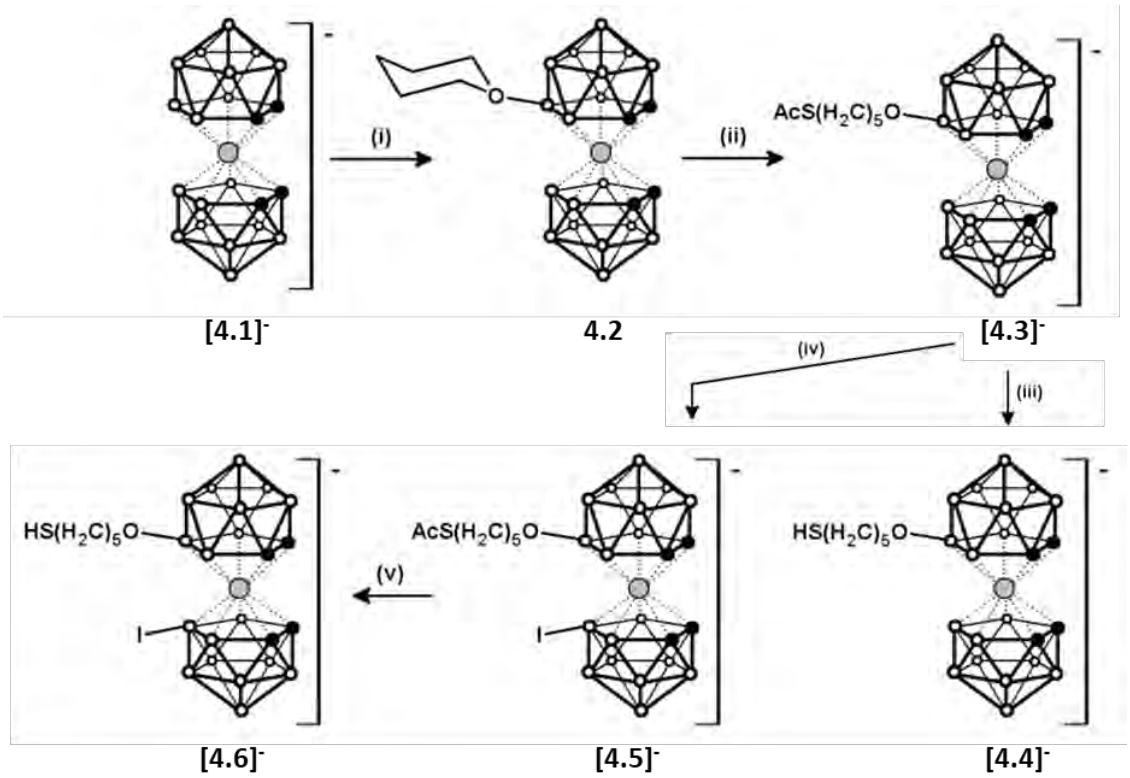

Scheme 3.1. Synthesis of functionalized COSAN derivatives **4.2**, **[4.3]**$^-$, **[4.4]**$^-$, **[4.5]**$^-$ and **[4.6]**$^-$. (i) THP, dimethylsulphate, H_2SO_4; (ii) DMF, KSAc; (iii) NaOMe, MeOH; (iv) CH_3CN, NaI, Chloramine-T; (v) NaOMe, MeOH

To conduct this reaction, we took advantage of the fact that boron atoms of the cobalt *bis*(dicarbollide) anion possessing high electron density can be easily functionalized with an inert spacer. B-substitution is explained by electrophile-induced nucleophilic substitution (EINS) mechanism. It involves the abstraction of the B–H hydrogen by an electrophile and subsequent attack by the nucleophile present in the reaction mixture. EINS mechanism has been described with different nucleophiles, such as tetrahydrofuran, tetrahydropyran and 1,4-dioxane, resulting

in the formation of charge-compensated derivatives. In our case, nucleophilic ring opening reaction of COSAN derivative (**4.2**; synthesized as previously described [12]) with potassium thioacetate (KSAc) in DMF yielded **[4.3]**$^-$ with overall yield of 52%. The reaction of **[4.3]**$^-$ with sodium methoxide in methanol at room temperature yielded **[4.4]**$^-$ in almost quantitative yield.

In parallel, COSAN derivatives bearing simultaneously a thiol group and an iodine atom were also synthesized the latter to enable radiolabeling with the positron emitter ^{124}I before attachment to the AuNPs (shell labeling) using isotopic exchange. The incorporation of the iodine atom was achieved by reaction of **[4.3]**$^-$ with sodium iodide, chloramine-T and acetic acid in acetonitrile overnight at room temperature to yield **[4.5]**$^-$ in 69% yield after purification. Basic hydrolysis of **[4.5]**$^-$ in sodium methoxide and methanol yielded the thio-derivative **[4.6]**$^-$ ready for incorporation into NPs or for radiolabeling using isotopic exchange reaction. Characterization using ^{1}H-, ^{11}B-, and ^{13}C-NMR confirmed the presence of the desired compounds (see experimental section for NMR data and Annex I for NMR spectra).

3.3.2. Synthesis of functionalized AuNPs

For successful clinical application, a BNCT drug should deposit a concentration of ^{10}B in the tumor in the range 20-35 μg ^{10}B/g of tissue, although lower amounts might be sufficient if the boron atoms are internalized into cells [13]. Additionally, high tumor-to-normal tissue and tumor-to-blood ratios should be achieved in order to prevent damage to healthy tissue and blood vasculature during neutron irradiation. Achieving these values is highly challenging, and nanotechnology has opened new opportunities due to the well-known EPR effect, which results in passive accumulation of nanosized materials in tumor tissue. Here, and inspired by the work reported by Cioran *et al.* [5, 14] we envisaged the possibility of using gold nanoparticles as boron carriers. Besides the easy functionalization chemistry, gold nanomaterials are chemically inert and non-toxic and both shape and size can be easily tuned [15]. Among all the possibilities, we decided to start with spherical particles with a size within the optimal range to achieve tumor accumulation [16]. In addition to the boron clusters, we decided to incorporate PEG chains on the NP surface in order to enhance the stability of the NPs in biological media and increase circulation time.

AuNPs were prepared by reduction of $HAuCl_4.3H_2O$ with trisodium citrate following a protocol based on the Turkevich method [6]. The aqueous solution of $HAuCl_4.3H_2O$ was heated to the

boiling point while stirring vigorously and then trisodium citrate was added quickly. A color change from pale yellow to deep red occurred within 10 minutes, indicating the formation of citrate-AuNPs. The solutions were kept at the boiling point for 15 minutes to assure the completion of the reaction and finally allowed to cool to room temperature (Figure 3.1).

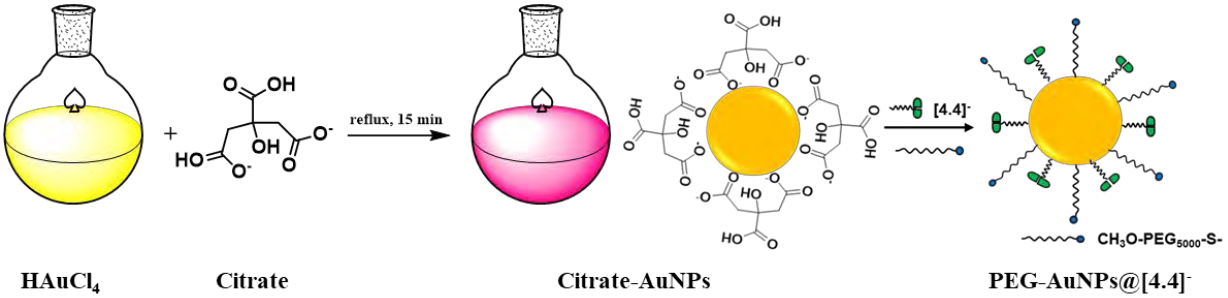

Figure 3.1. Schematic representation of the preparation of citrate-AuNPs and PEG-AuNPs@[4.4]$^-$

The formation of citrate-AuNPs was confirmed by UV-absorption spectroscopy and transmission electron microscopy (TEM). UV-absorption spectra showed the longitudinal surface plasmon resonance (SPR) band at 524 nm (Figure 3.2a), indicating the formation of AuNPs with particle size in the range of 20 nm. TEM images revealed the presence of non-aggregated citrate-AuNPs with average particle size of 19.2±1.4 nm (Figure 3.2c).

After successful preparation of citrate-AuNPs, the next step was to attach the functionalities, namely PEG and COSAN, on the surface of AuNPs. Thiolated polyethylene glycol ($mPEG_{5k}$-SH) and **[4.4]**$^-$ were covalently attached to the surface of the citrate-AuNPs based on a previously reported methodology with slight modifications [17]. The ultimate goal was to achieve a maximum amount of boron atoms on the surface of the NPs, without compromising stability and aggregation status. Hence, we first performed a set of experiments by using various molar ratios of PEG and COSAN (1:4, 1:6, 1:8, 1:10, 1:12 and 1:14), which were added to the citrate-AuNPs (Au concentration, 1 mg/mL). After addition of PEG and COSAN, the solution was stirred at room temperature for 2 h to allow for complete exchange of the citrate molecules with PEG and COSAN. The PEG-AuNPs@[4.4]$^-$ solutions were then centrifuged and analyzed by ICP-MS to investigate the relative amount (PEG to COSAN) for the resulting PEG-AuNPs@[4.4]$^-$. We found that, in all cases, NPs were stable and dispersible. However, ratios above 1:10 (PEG to COSAN) did not result in an increase in the COSAN concentration on the surface. Under these

conditions, the amount of ligand on the surface of the NPs was 200 µg/mg of gold, which results in a boron concentration of 90 µg per mg of gold.

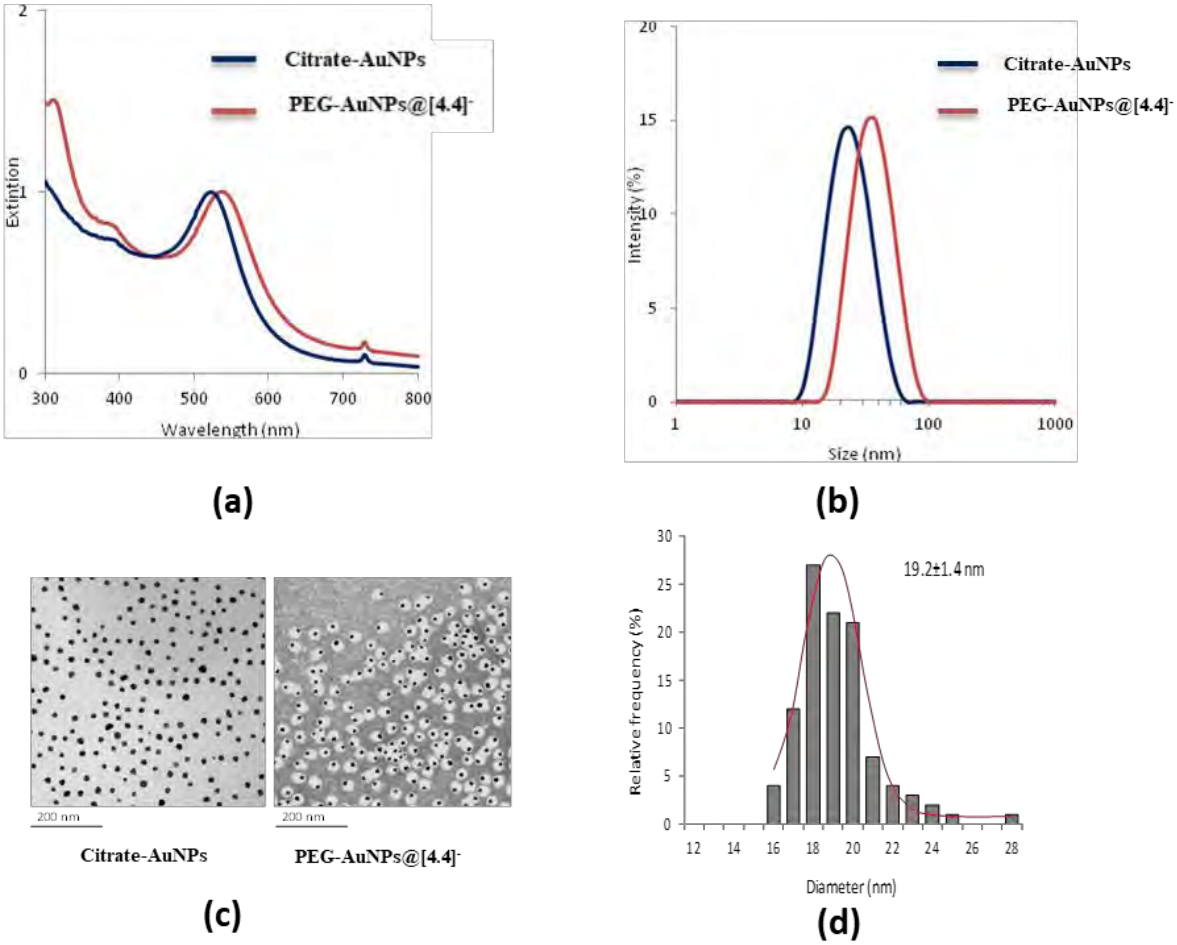

Figure 3.2. (a) UV-Vis spectra corresponding to citrate stabilized AuNPs (AuNPs-Citrate, blue, λmax=524 nm) and PEG-stabilized AuNPs@[4.4]$^-$ (PEG-AuNPs@[4.4]$^-$, red, λmax=531 nm for the gold plasmon; λmax=310 nm corresponds to compound **[4.4]**$^-$); (b) Size distribution ranges as determined by DLS (volume distribution) for AuNPs-Citrate and PEG-AuNPs@[4.4]$^-$ (same color code as in (a)); (c) representative TEM images of AuNPs-Citrate and PEG-AuNPs@[4.4]$^-$; (d) Particle size distribution of PEG-AuNPs@[4.4]$^-$ as determined by TEM.

The characterization of the final particles PEG-AuNPs@[4.4]$^-$ was carried out first using UV-vis spectrophotometry (Figure 3.2a). As it can be seen, the simultaneous incorporation of PEG and COSAN on the surface of the citrate AuNPs resulted in a bathochromic shift in the longitudinal surface plasmon resonance (SPR) band from 524 nm to 531 nm. Noteworthy, another absorption band appeared at ca. 310 nm, close to the maximum absorption of COSAN (314 nm), confirming successful incorporation of the boron cluster on the surface of the AuNPs.

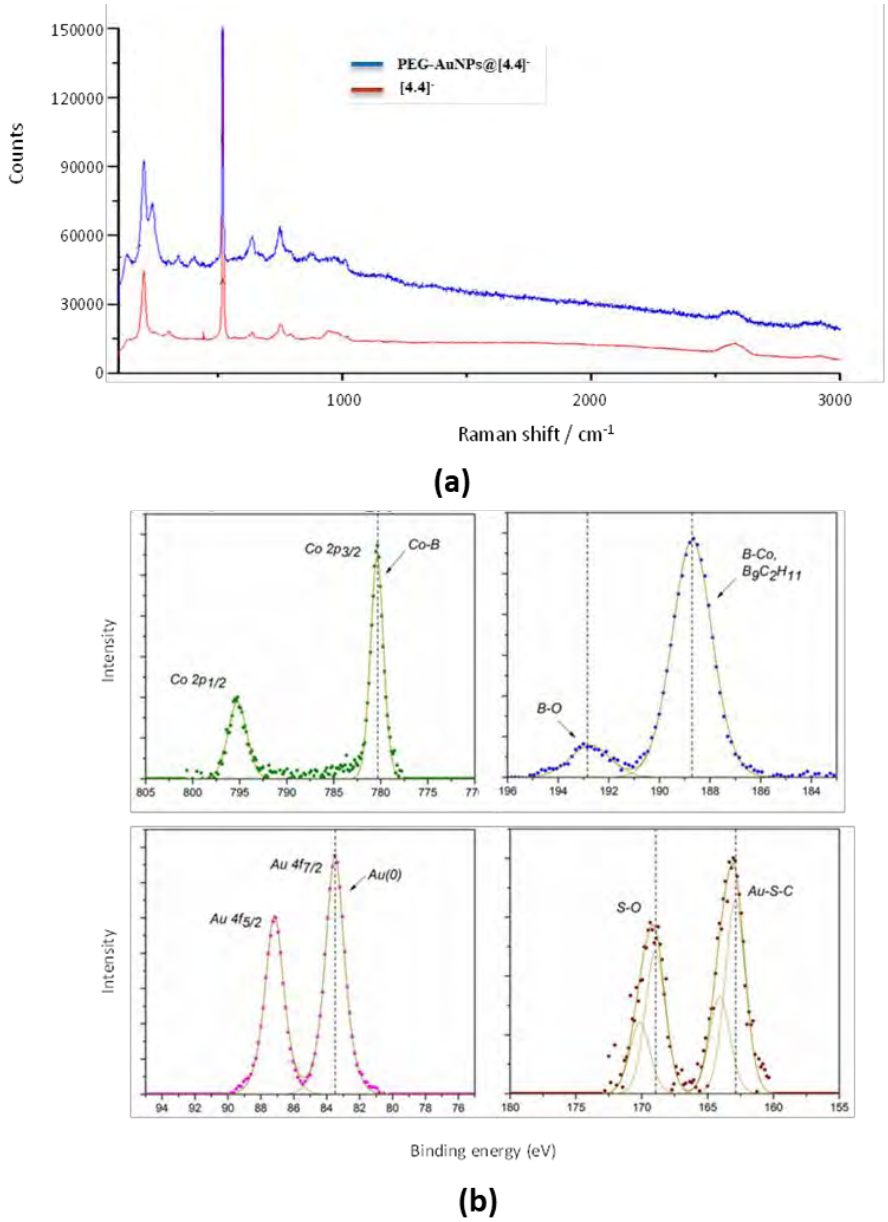

Figure 3.3. Raman spectra for PEG-AuNPs@[4.4]$^-$ (blue) and [4.4]$^-$ (red), (b) XPS spectra of PEG-AuNPs@[4.4]$^-$.

Dynamic light scattering (DLS) analysis performed on citrate-AuNPs and PEG-AuNPs@[4.4]$^-$ showed a monodisperse distribution with average hydrodynamic diameter of 24.4±0.5 nm and 37.8±0.5 nm respectively (Figure 3.2b). The increase in hydrodynamic size from 24.4±0.5 nm and 37.8±0.5 nm is largely due to the addition of PEG molecule, as the small size of the COSAN

moiety (~ 1-2 nm) is expected to have a minimal impact on hydrodynamic size when compared to the effect of the large molecule PEG-5000. Transmission electron microscopy (TEM) images show non-aggregated spherical AuNPs before and after PEG and COSAN addition (Figure 3.2c) with average particle core size of 19.2±1.4 nm (Figure 3.2d). Zeta potential measurements of citrate-AuNPs showed a ξ-potential of −32.3±2.5 mV; after incorporation of both PEG and COSAN, PEG-AuNPs@$[4.4]^-$ showed a ξ-potential value of −18.0±0.7 mV at neutral pH, the negative value due to the presence of COSAN anions on the surface of the NPs.

To further confirm the presence of COSAN moieties on the surface of the AuNPs, we performed Raman spectroscopy and X-ray photoelectron spectroscopy (XPS). The Raman spectra of PEG-AuNPs@$[4.4]^-$ showed the presence of absorption bands at 2596−2573 cm^{-1}, corresponding to B−H stretching and confirming the presence of the sandwich complex on the NP surface (Figure 3.3a). Finally, XPS analysis of PEG-AuNPs@$[4.4]^-$ showed a peak at 780.2 eV in the Co spectrum, corresponding to Co-B bonds; peaks at 192.8 and 188.5 eV, corresponding to B-O and C-B bonds; peaks at 87.5 and 83.5 eV, corresponding to Au; and a peak at 162.5 eV, corresponding to Au-S-C bond (Figure 3.3b) [18]. These results confirmed the presence of both cobalt and boron on the surface of AuNPs; altogether, our results confirm that the NPs have a significant boron load and appropriate size for eventual tumor accumulation.

3.3.3. Radiolabeling of AuNPs

One of the main challenges in BNCT is the determination of the biodistribution of the boron carrier after administration, in order to establish the optimal time window for neutron irradiation, for the therapeutic effect to be optimal, while minimizing side effects and destruction of the surrounding healthy tissue (Figure 3.4). This drawback is even more evident when nanomaterials are used as boron carriers, as the determination of the biodistribution and fate of NPs after administration into living systems is extremely challenging. One alternative to overcome this drawback consists of incorporating a positron or gamma emitter into the nanoparticle in order to track the location in a time-resolved fashion using Positron Emission Tomography (PET) or Single Photon Emission Computerized Tomography (SPECT) imaging. This approach has been widely reported in the literature in NPs with very different nature [19, 20]. Additionally, incorporation of the label both at the core and at the shell of NPs can provide very relevant information about the *in vivo* stability of the NPs [21].

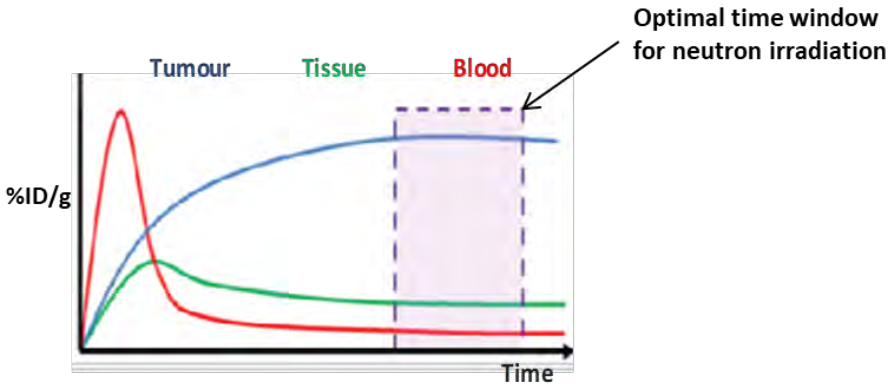

Figure 3.4. Fictitious boron concentration curves vs. time for the tumor (blue), blood (red) and healthy tissue (green). The optimal time-window for the application of neutron irradiation, when the concentration of boron is maximum in the tumor and low in both blood and healthy tissue, is shown.

Here, we decided to tackle the radiolabeling of the NPs using a positron emitter, as PET offers better spatiotemporal resolution and higher resolution than SPECT. We anticipated that the positron emitter ^{124}I (half-life of 4.2 days) was appropriate due to the following reasons: (i) its reasonably long half-life should enable long-term monitoring (up to 2 weeks if needed) of the *in vivo* behavior of the NPs; (ii) due to the versatile chemistry of the radionuclide, it could be incorporated both at the core, taking advantage of the capacity of iodine to absorb onto gold surfaces [11], and on the shell, by generating first a iodinated analogue of COSAN and performing in a second step isotopic exchange reaction, as previously described [22]. Our hypothesis is that the iodinated analogue of COSAN should behave quite similarly to the non-iodinated counterpart, and hence the properties of the AuNPs should not be significantly altered by the incorporation of the label.

We first tackled the incorporation of ^{124}I at the shell (Figure 3.5). With that aim, compound ^{124}I-**[4.5]**$^{-}$ was prepared by isotopic exchange, following a methodology previously described in our group with minor modifications (Scheme 3.2) [22]. In brief, acetonitrile was added to Na[^{124}I]I (obtained from the supplier as a solution in diluted NaOH) and the resulting solution was evaporated to dryness under nitrogen flow. Compound **[4.5]**$^{-}$ was dissolved in acetonitrile was added to the dry residue, together with *trans-bis*(acetate)*bis*[o-(di-o-tolylphosphino)benzyl] dipalladium (II) (Herrmann's catalyst), the later dissolved in toluene. The reaction mixture was heated at 100°C for 5 min, the solvent was removed under a constant helium flow and the

resulting solid was dissolved in acetonitrile and water. The crude solution was passed through a C-18 cartridge (Sep-Pak® Light, Waters) and washed with ultrapure water to remove free iodine-124. The labeled compound, retained in the C-18 cartridge, was finally eluted with acetonitrile, which was finally evaporated to yield the labeled compound as an orange solid.

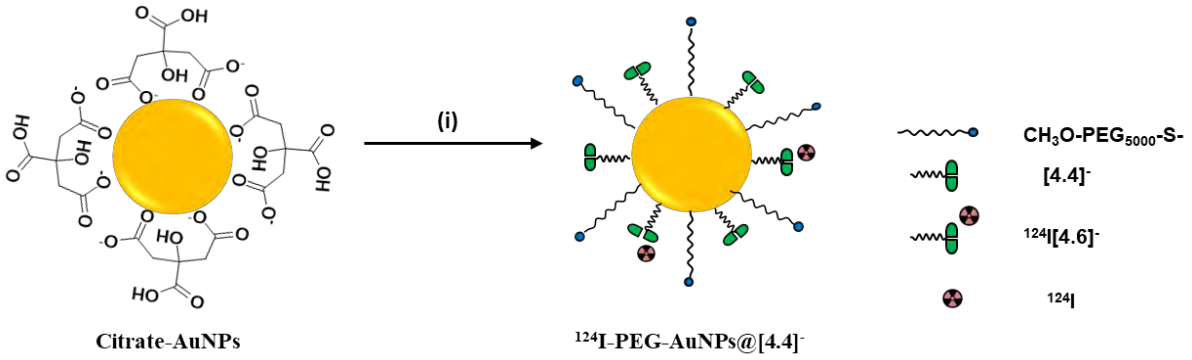

Figure 3.5. Schematic representation for the preparation of shell radiolabeled PEG-AuNPs@$[4.4]^-$. [i] PEG-SH (5 Kda), ^{124}I-$[4.6]^-$ + $[4.4]^-$.

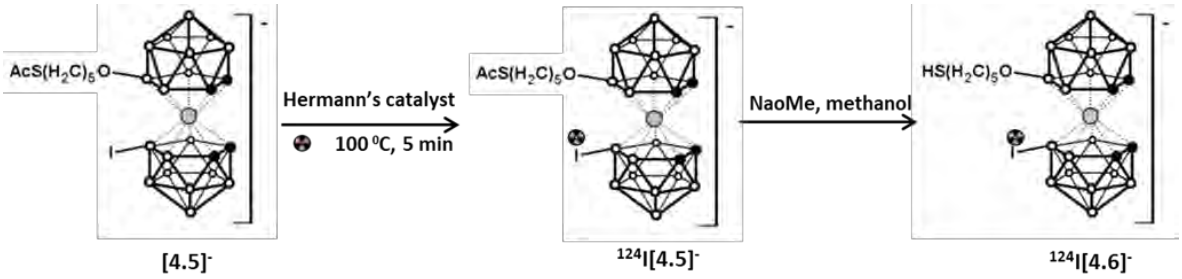

Scheme 3.2. Reaction for the preparation of ^{124}I-$[4.6]^-$

Quality control was performed by high performance liquid chromatography (HPLC) coupled to a radioactivity detector. With that aim, the solid residue was diluted with mobile phase (see experimental section for details) and analyzed. Incorporation ratios of the radiolabel (measured directly from chromatographic profiles, radioactivity detector) of 69±6% were achieved when the reaction was conducted at 100°C for 5 min. These values are in good agreement with those previously described [22]. Purification by semi-preparative HPLC resulted in a solution of chemically and radiochemically pure compound ^{124}I-$[4.5]^-$ (Figure 3.6) with radiochemical yield (non-decay corrected) of ca. 60%.

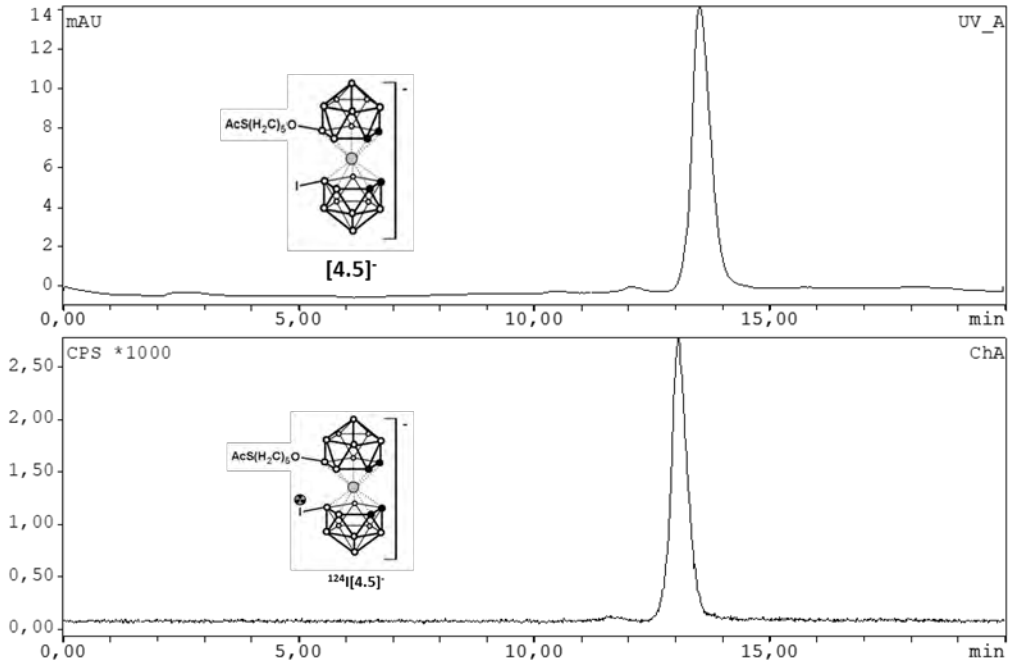

Figure 3.6. Chromatographic profiles (UV and radiometric detection) for reference compound $[4.5]^-$ (top) and purified ^{124}I-$[4.5]^-$ (bottom). The difference in the position of the two peaks is due to the dead volume between the UV and the radioactivity detectors.

The isotopic exchange reaction was carried out using **[4.5]**$^-$, which had the thiol group protected, because the presence of a free thiol group may interfere in the isotopic exchange reaction. Hence, to enable attachment of the labeled COSAN analogue to the gold NPs, deprotection was required. With that aim, ^{124}I-**[4.5]**$^-$ was reacted with sodium methoxide in methanol at room temperature for 6 h, yielding ^{124}I-**[4.6]**$^-$ in quantitative yield, which was used without further purification. The preparation of the radiolabeled AuNPs was carried out following the same process described above, but compound **[4.4]**$^-$ was spiked with **^{124}I-[4.6]**$^-$. Radiolabeling efficiency, calculated as the amount of radioactivity present in the NPs related to the starting amount of **^{124}I-[4.6]**$^-$ was 55%.

The second approach for the preparation of radiolabeled AuNPs was based on the absorption of radioiodine on the surface of the gold core [11, 23]. First, we tried to incorporate radioiodine directly on PEG-AuNPs@$[4.4]^-$ (Figure 3.7). However, low incorporation efficiencies (<10%) were achieved when PEG-AuNPs@$[4.4]^-$ were incubated with the radionuclide. These results are not in agreement with previously reported works, in which almost quantitative labeling yields were obtained [11, 23]. We suspected that the presence of the COSAN anions on the surface of

the NPs hampered the adsorption of radioiodide on the gold surface, probably due to electrostatic repulsion or steric hindrance.

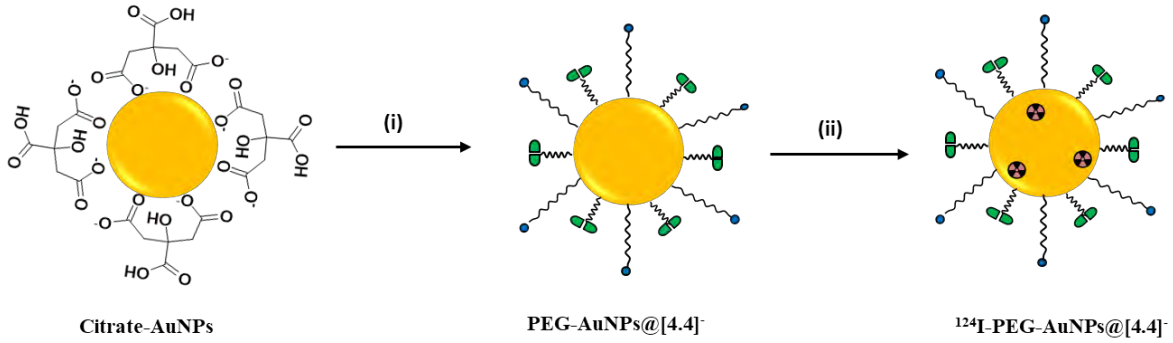

Figure 3.7. Schematic representation for the preparation of core radiolabeled PEG-AuNPs@[4.4]$^-$. [i] PEG-SH (5 Kda), [4.4]$^-$, [ii] [^{124}I]NaI.

To overcome this limitation, we assayed a second strategy, based on the incorporation of the radionuclide on citrate-stabilized NPs, which were functionalized with PEG and COSAN derivatives in a second step.

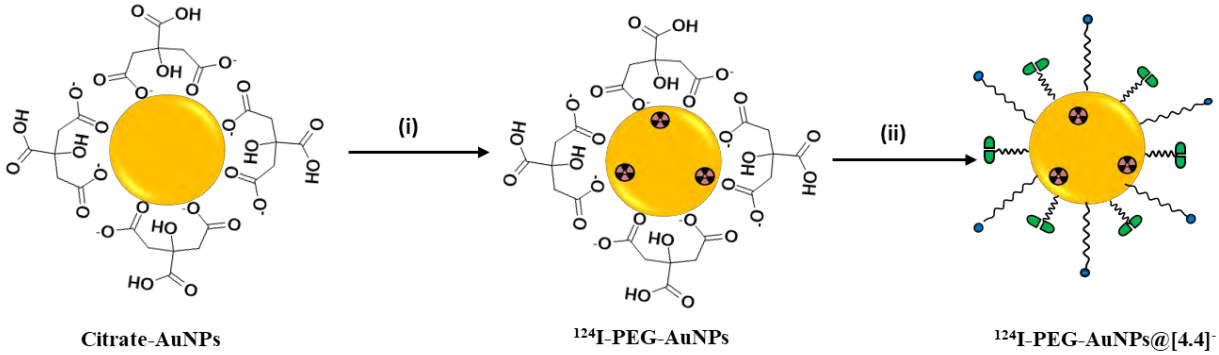

Figure 3.8. Schematic representation for the preparation of core radiolabeled PEG-AuNPs@[4.4]$^-$. [i] [^{124}I]NaI; (ii) PEG-SH (5 Kda), ^{124}I-[4.6]$^-$ + [4.4]$^-$.

With that aim, citrate-stabilized NPs were incubated with radioiodine and incorporation ratios were determined at different incubation times. Experimental results demonstrated that the reaction took place very rapidly, as incorporation ratios >95% were achieved in just 10 minutes of incubation. These results are more in line with those previously reported in the literature. In view of these results, we decided to incorporate the radiolabel on citrate-stabilized NPs and incorporate both the PEG and COSAN derivatives in a second step (Figure 3.8). This approach

was successful and core-labeled NPs with size and zeta-potential values equivalent to those obtained for non-labeled NPs could be determined using DLS.

3.3.4. Radiochemical stability of AuNPs

One of the main limitations of the second labeling approach is the risk of detachment of the absorbed radionuclide. Ideally, radiochemical stability of the labeled particles should be evaluated *in vivo*. However, this is extremely challenging. An alternative approach consists of incubating the labeled particles in different media, trying to mimic *in vivo* conditions [24]. In our case, in order to evaluate the radiochemical stability of core-labeled [^{124}I]PEG-AuNPs@[4.4]$^{-}$, NPs were incubated in different media, including water, saline, PBS (10 mM), DMEM (Cell culture media), plasma and potassium iodide (10 μM).

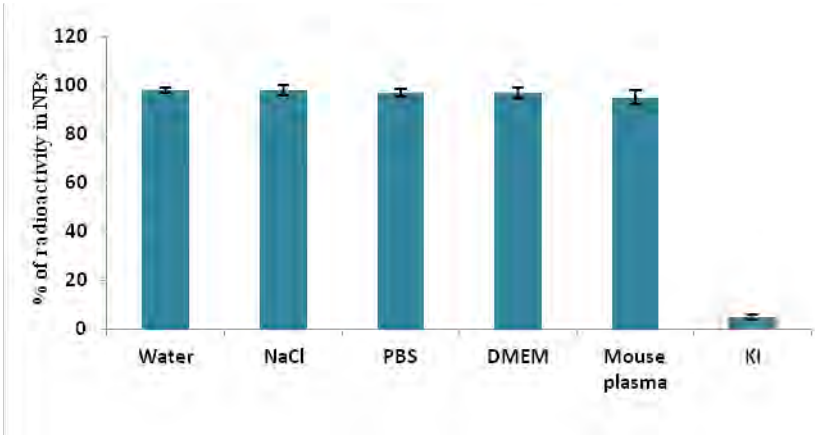

Figure 3.9. Radiochemical stability of core-labeled PEG-AuNPs@[4.4]$^{-}$ in different media for 24 h; Water; NaCl: physiologic saline solution (0.9%); PBS (10 mM); DMEM: Culture media, cocktail of 8 salts, 15 amino acids, 8 vitamins and glucose; KI: potassium iodide solution (10 μM).

After incubation at 37 $^{\circ}$C for 24 h, the NPs were separated from the media by centrifugal filtration and washed three times, and the radiochemical stability was determined as the ratio between the amount of radioactivity in the NPs and the total amount of radioactivity (NPs + media + washings). Good radiochemical stability (>90%) was observed in all media except potassium iodide (Figure 3.9), thus confirming the chemisorption of ^{124}I and the suitability of the labeling strategy for *in vivo* studies.

3.3.5. Biodistribution studies in tumor bearing animals

The capacity of the newly developed AuNPs (PEG-AuNPs@[4.4]$^-$) to accumulate in tumor tissue was investigated in a subcutaneous mouse model generated by inoculation of HT 1080 cells in nude mice. Traditionally, BNCT has been investigated mainly for brain (gliomas) and head & neck cancers. However, this therapeutic approach can in principle be evaluated in any cancer type, and those cancers with high mortality or lack of efficient therapeutic alternatives are worth to be assayed. Hence, we decided to investigate human fibrosarcoma tumor model. This is a quite rare cancer type. However, it is highly aggressive and metastasizes at early stages. The standard therapy, which includes surgical resection and adjuvant chemotherapy, is ineffective due to local recurrence and distant metastasis [25].

Imaging studies performed in mice enabled the determination of the biodistribution pattern of the labeled particles. Additionally, the inclusion of the label in the two different positions (the core and the shell) was used to gain information about the stability of the core-shell structure, an issue that is rarely tackled in preclinical *in vivo* investigations. With that aim, animals were injected with the labeled particles and images were acquired immediately after administration (total acquisition time of 60 min). Additionally, 30 min static acquisitions were recorded also at t=10, 24, 72 and 144 h post-administration (Figure 3.10).

Visual inspection of the images showed a similar biodistribution pattern for both PEG-AuNPs@[4.4]$^-$, irrespectively of the position of the label. High accumulation was observed in the liver at short times after administration (0-1 hour). Delineation of volumes of interest (VOIs) in major organs (lungs, liver, bladder, stomach, kidneys, spleen, tumor, heart and thyroid gland) and determination of the uptake as % of injected dose per cm^3 tissue (%ID/cm^3, see Figure 3.11) revealed similar profiles irrespective of the position of the label, this confirming the *in vivo* stability of the core-shell structure. Major accumulation at short times after administration was observed in the liver. For this organ, values at the first time point were 42.2 ± 4.8 and 39.1 ± 5.8 %ID/cm^3 for core and shell labeled particles, respectively. These values, which are statistically equivalent, progressively decreased with time to reach values close to 10% ID/cm^3 at t=144 h. Accumulation in the stomach peaked at t=24 h after administration, with progressive elimination from this organ at later time points. Accumulation in the lungs was also significant. Of note, the detection of radioactivity in the heart reflects the presence of labeled NPs in the bloodstream,

even at long times after administration. The presence of radioactivity in the bladder at long times after administration confirms slow elimination via urine. This result, together with the detection of radioactive signal in the thyroid gland, suggests the progressive (although very slow) detachment of the radiolabel in both cases (core and shell labeling).

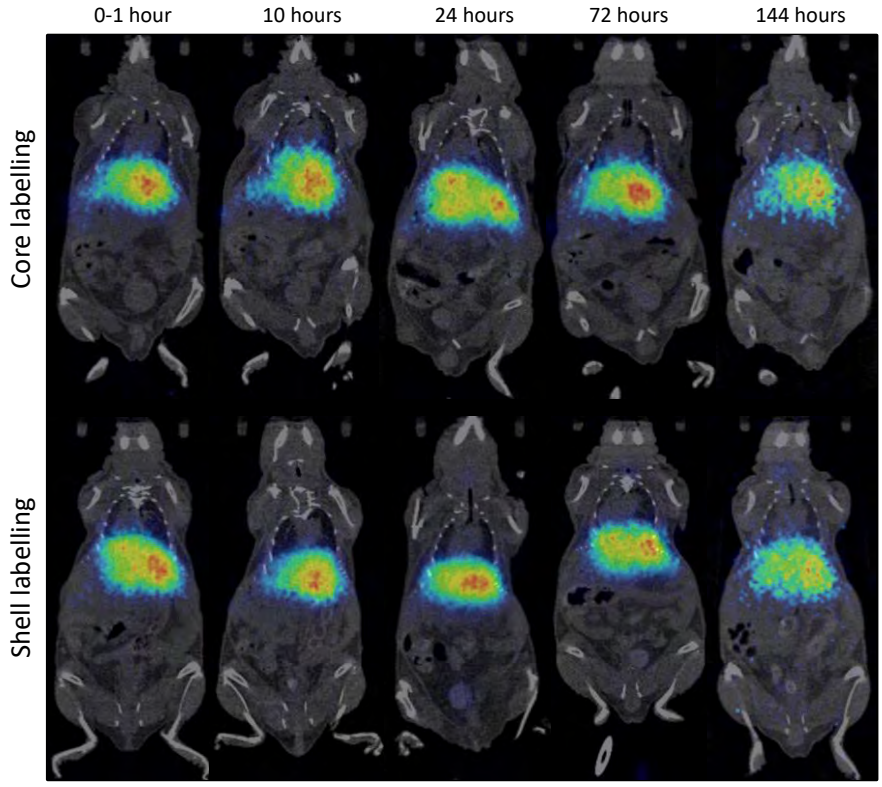

Figure 3.10. PET images (coronal projections) obtained at different time points after intravenous administration of [^{124}I]PEG-AuNPs@[4.4]$^{-}$ labeled at the core and at the shell. PET images have been corregistered with representative CT slices for localization of the radioactive signal. The image labeled as "0-1 hour" corresponds to the image obtained immediately after administration of the labelled NPs (imaging time = 1 hour).

Our biodistribution data, in general terms, correlates well with previous results obtained with negatively charged NPs. In general, it has been found that, upon single intravenous administration, spherical AuNPs localize in liver, kidneys, spleen and lungs, with this phenomenon being size- and shape-dependent. For NPs in our size range, major accumulation should be expected in liver, spleen and lungs, as observed in our studies [26].

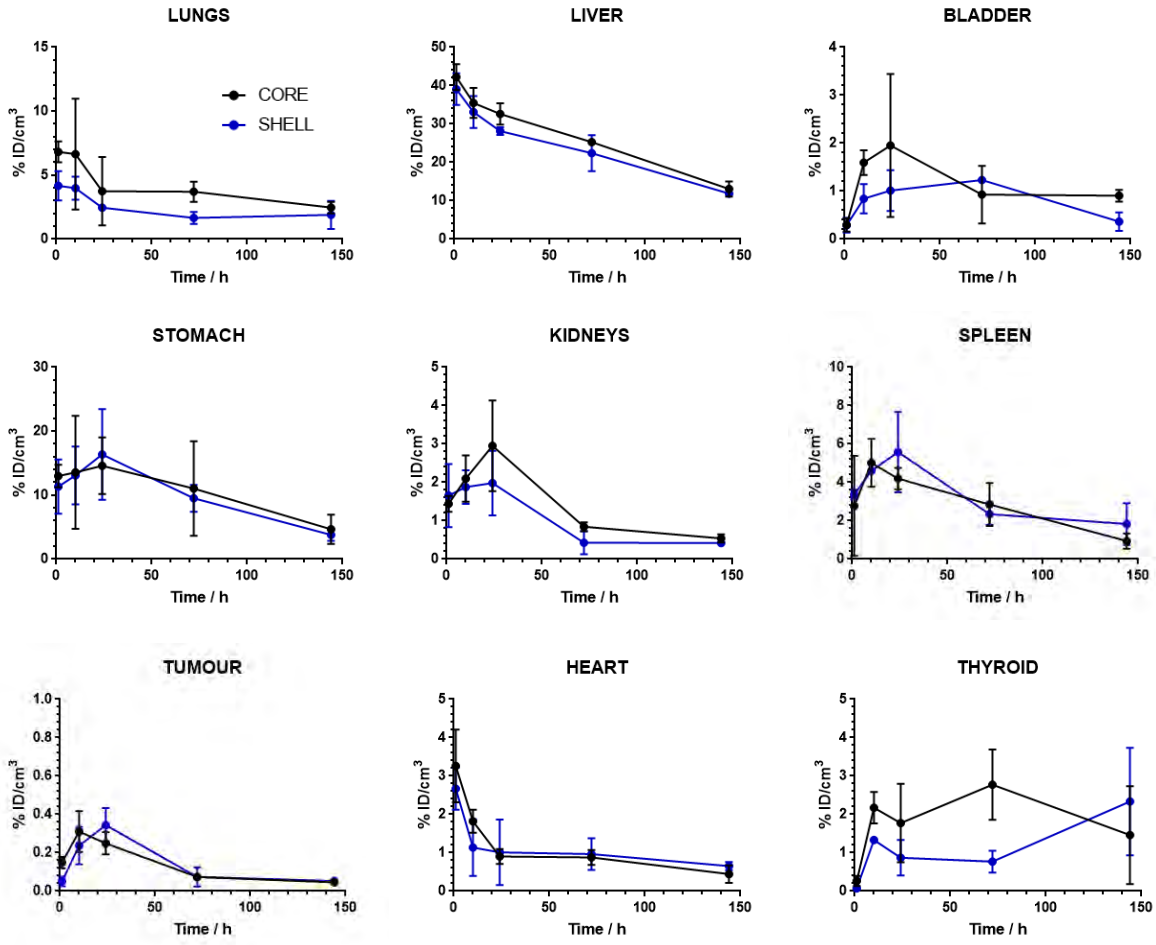

Figure 3.11. Concentration of radioactivity in the different organs as determined from PET images using the two radiolabeling approaches. Values are expressed as %ID/cm^3. Values correspond to mean ± standard deviation, n=2 per labeling strategy and time point.

Next, we conducted *ex vivo* analysis to confirm the NPs accumulation in the liver observed during *in vivo* studies. With that aim, after the last imaging session, animals were sacrificed and the liver organ was collected and investigated using ion beam microscopy (IBM) and confocal Raman microspectroscopy (CRM) (Figure 3.12). These label-free techniques have proven to be efficient for simultaneous quantification and visualization of a variety of NPs in biological environments [27, 28, 29, 30, 31]. The μPIXE spectrum extracted from the region of interest (ROI; see Figure 3.12b) reveals X-ray emission of intrinsic tissues elements, i.e., P, S, Ca etc., as well as of gold. Characteristic Lα, Lβ and Lγ X-ray lines of gold at 9.7 keV, 11.4 keV and 13.4 keV were detected in the ROIs shown as green regions in Figure 3.12a. The structure of several connected hepatic lobules could be identified due to P and S distribution in the PIXE images.

PIXE maps of Au distribution showed a rather homogenous distribution all over those lobules. However, a high resolution image with a size of 100 × 100 µm revealed small gold clusters in the hepatocytes (white circles in Figure 3.12a).

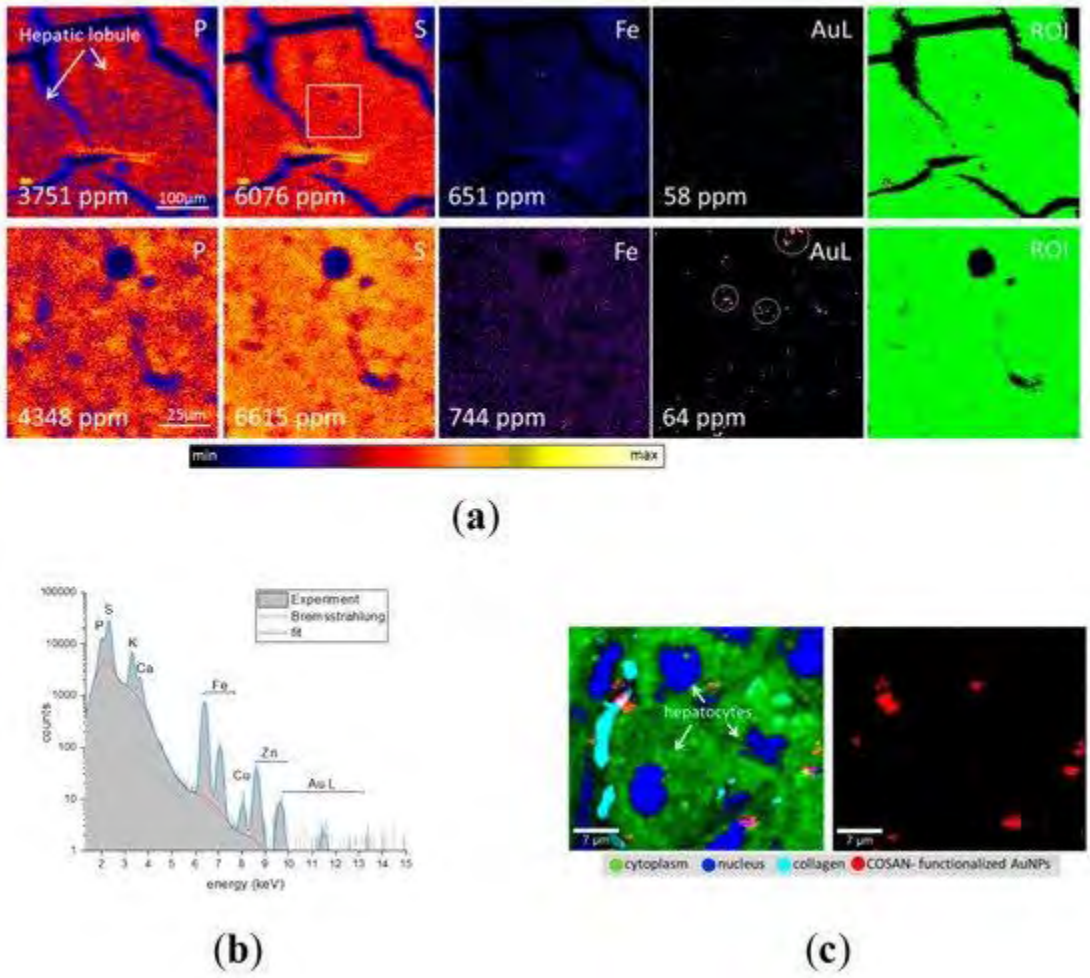

Figure 3.12. (**a**) µPIXE images of intrinsic tissue elements (P, S, Fe) as well as Au in mouse liver at t = 72 h after intravenous administration of [^{124}I]PEG-AuNPs@[**4**]$^{-}$. The area in the white rectangle was subsequently scanned with higher resolution. The concentration of elements was calculated from regions of interest (ROIs) shown in green on the right side. White arrows denote hepatic lobules. White circles show small gold clusters; (**b**) PIXE spectrum extracted from ROIs; (**c**) CRM images of hepatocytes and distribution of [^{124}I]PEG-AuNPs@[**4**]$^{-}$ in in mouse liver at t = 72 h after intravenous administration of [^{124}I]PEG-AuNPs@[**4**]$^{-}$. The color-coded image (left) shows the overlapping of nucleus, cytoplasm, collagen and COSAN- functionalized Au NPs.

CRM imaging was additionally used to visualize the distribution pattern of NPs in the liver at subcellular level (Figure 3.12c). Au NPs were localized in hepatic lobules by using photoluminescence signals of Au. Cytoplasm, nuclei and collagen were visualized on the basis of

Raman fingerprint regions of biomolecules [32, 33, 34], which are predominantly present in the corresponding constituents of cell. As it can be seen, lobules are surrounded by supporting connective tissue, which was identified in CRM imaging by the presence of collagen. Au NPs were found in the cytoplasm of hepatocytes as well as in close vicinity to their nuclei. Some Au NP aggregates were also detected between adjacent lobules showing a co-localization with the connective tissue.

The data obtained in our *in vivo* study confirm that the position of the label does not have an effect on the biodistribution of the NPs, hence confirming that the label is relatively stable *in vivo*. However, the high uptake in the liver already at early times after administration of the NPs compromises the usefulness of our nanosystems for *in vivo* applications. The high uptake in the liver results in a low bioavailability, and as a consequence the circulation time is low and the tumor accumulation is almost negligible, with values below 0.5% ID/cm^3, irrespective of the labeling approach and time point. Considering that the boron load of our NPs is ca. 9% and that the administered dose of NPs was 150 µg (ca. 7.5 mg NP/Kg body weight; 0.675 mg B/Kg body weight), the boron accumulation in the tumor is close to 0.06 µg B/g of tumor. This value is by far too low to plan any therapeutic experiments. The results demand for modifications in the physic-chemical properties of the NPs in order to improve pharmacokinetic properties, which ultimately may lead to increased accumulation in the tumor. This was carried out as described in the following chapters.

3.4. Conclusions

The reaction of citrate-stabilized gold NPs with COSAN bearing a thiol moiety and thiolated polyethylene glycol ($mPEG_{5k}$-SH) yields NPs with ca. 9% boron content on the surface. Radiolabeling of the NPs with the positron emitter ^{124}I could be achieved both at the core (by absorption of ^{124}I on the gold surface) or at the shell (by using isotopic exchange). The labeled particles showed good stability both *in vitro* and *in vivo*, although progressive detachment of the label could be observed *in vivo*. Investigation of the biodistribution pattern in a mouse cancer model using positron emission tomography confirmed high accumulation of the NPs in the liver at short times after administration, and very low accumulation in the tumor, the latter demanding for modification in the physico-chemical properties of the NPs in order to achieve higher tumor uptake.

3.5. Experimental section

3.5.1. Reagents

Cesium cobalt(III) *bis*(dicarbollide) (COSAN) (Katchem Ltd., Prague, Czech Republic), gold(III) chloride trihydrate ($HAuCl_4 \cdot 3H_2O$, Aldrich), sodium citrate tribasic dihydrate (Sigma-Aldrich), poly (ethylene glycol) methyl ether thiol (MW 5000, Sigma-Aldrich) tetrahydropyran (Sigma-Aldrich) and *trans*-*bis*(acetate)*bis*[o-(di-o-tolylphosphino)benzyl] dipalladium (II) (Herrmann's catalyst, Sigma-Aldrich), were used as purchased. All other reagents and anhydrous solvents, stored over 4 Å molecular sieves, were purchased from Aldrich Chemical Co. (Madrid, Spain) and used without further purification. HPLC grade solvents were purchased from Scharlab (Sentmenat, Barcelona, Spain). For radiolabeling experiments, Iodine-124 (^{124}I) was obtained from PerkinElmer. (Le petten, The Netherlands) in 0.2 M NaOH solution.

In chemical reactions, experiments were carried out (except noted otherwise), under dinitrogen atmosphere. Column chromatography was performed using silica gel 60 (Scharlab, Spain). Analytical thin layer chromatography (TLC) measurements were conducted with silica gel 60 F_{254} plates (Macherey-Nagel); and the spots were visualized under UV lamp. Synthesis of compound **4.2** was carried out according to the previously reported protocol [12].

3.5.2. Instrumentation

The ^{1}H-NMR (500 MHz), ^{13}C-NMR (126 MHz) and ^{11}B-NMR (160 MHz) spectra were recorded on a 500-MHz Avance III Bruker spectrometer. All NMR spectra were performed in deuterated solvents at 22°C. The ^{11}B-NMR shifts were referenced to external $BF_3 \cdot OEt_2$, while the ^{1}H and ^{13}C-NMR shifts were referenced to $SiMe_4$. Chemical shifts are reported in units of parts per million downfield from the reference, and all coupling constants are reported in Hertz.

UPLC/ESI-MS analyses were performed using an AQUITY UPLC separation module coupled to a LCT TOF Premier XE mass spectrometer (Waters, Manchester, UK), using an Acquity BEH C18 column (1.7 μm, 5 mm, 2.1 mm) as the stationary phase. The elution buffers were A (water and 0.1% formic acid) and B (Methanol and 0.1% formic acid). The column was eluted with a gradient: t=0 min, 95% A, 5% B; t=0.5 min, 95% A, 5% B; t=5.5 min, 25% A, 75% B; t=16 min, 1% A, 99% B; t=20min, 1% A, 99% B. Total run was 20 min, injection volume was 5 μL and

the flow rate 300 μL/min. The detection was carried out in both negative and positive ion mode, monitoring the most abundant isotope peaks from the mass spectra ($M\text{-}H^+$) or ($M+H^+$).

Transmission electron microscopy (TEM) was performed using a JEOL JEM-1400 plus microscope (Jeol, Tokyo, Japan) working at 120 kV. The carbon film of copper grids (CF400-Cu) was treated under air plasma in a glow discharge system (Emitech K100X, 40mA during 2 min) just before sample preparation. For TEM examinations, a single drop (1 μL) of the NPs solution was placed onto a copper grid coated with a carbon film (Electron Microscopy Sciences). After 1 minute, the drop was removed with filter paper and the sample was incubated with 3 μL of uranyl acetate 0.5% (3 min).

XPS experiments were performed in a SPECS Sage HR 100 spectrometer with a non-monochromatic X ray source (Aluminium Kα line of 1486.6 eV energy and 252 W), placed perpendicular to the analyser axis and calibrated using the 3d5/2 line of Ag with a full width at half maximum (FWHM) of 1.1 eV. The selected resolution for the spectra was 15 eV of Pass Energy and 0.15 eV/step. All measurements were made in an ultra-high vacuum (UHV) chamber at a pressure around 6×10^{-8} mbar. An electron flood gun was used for charge neutralisation. Gaussian Lorentzian functions were used for fittings (after a Shirley background correction) where the FWHM of all the peaks were constrained while the peak positions and areas were set free. Main C1s peak was used for charge reference and set at 284.8 eV.

ICP-MS measurements were performed on a Thermo iCAP Q ICP-MS (Thermo Fisher Scientific GmbH, Bremen, Germany). An ASX-560 autosampler was coupled to the ICP-MS (CETAC Tech, Omaha, NE, USA). UV-Vis spectra were measured in an Agilent 8453 UV-Vis diode-array spectrophotometer. DLS and ξ-potential measurements were performed using a Malvern Zetasizer Nano ZS system (Malvern Instruments, Malvern, UK). The particle size measurement settings were: 3 measurements/14 runs/10s in scattered mode at 173° angle. Measurements were conducted at T=25°C and neutral pH.

Raman characterization was performed with a Renishaw InVia Raman Microscope. A 633 nm laser (50 % power) was used with 10x objective.

3.5.3. Chemistry

Synthesis of **[4.3]**$^-$

To a solution of compound **4.2** (750 mg, 1.209 mmol) in DMF (8 mL), potassium thioacetate (165.7 mg, 1.451 mmol) was added and stirred at room temperature for 14 h. After finalization of the reaction, water (50 mL) was added and extracted with ethyl acetate (3x50 mL). The organic layers were combined and washed with cold water and brine solution before drying over anhydrous sodium sulphate. The solvent was evaporated and the crude was purified using column chromatography (silica gel, 10% MeOH in dichloromethane) to yield a **[4.3]**$^-$ as yellow solid (705 mg, 84%).

^{1}H NMR (500 MHz, Methanol-d_4) δ 4.15 [C_c–*H*, 2H, s], 4.07 [C_c–*H*, 2H, s], 3.49 [CH_2O, 2 H, t], 2.87 [CH_2-S, 2 H, t], 2.31 [CH_3, 3 H, s], 1.59 – 1.54 [CH_2-CH_2-O, 2 H, m], 1.52 – 1.47 [CH_2-CH_2S, 2 H, m], 1.42 – 1.37 [CH_2-CH_2CH_2O, 2 H, m]; ^{11}B NMR (160 MHz, MeOD) δ 23.03[1B, s], 4.63 [1B, d, ^{1}J(B-H)=140.3], 0.48 [1B, d, ^{1}J(B-H)=143.3], -2.10 [1B, d, ^{1}J(B-H)=142.8], -4.59[2B, d, ^{1}J(B-H)=138.7], -8.46 [6B, td, *J* 162.8, 150.9, 63.5], -17.22 [2B, d, ^{1}J(B-H)=154.4], -20.42 [2B, d], -22.59 [1B, d], -28.26 [1B, d, ^{1}J(B-H)=159.4]; ^{13}C NMR (126 MHz, Methanol-d_4): 188.24, 68.93, 53.54, 46.70, 30.89, 29.21, 29.14, 28.61, 25.10; LCMS (ESI) Experimental [M]$^-$ m/z = 482.66 (theoretical [M]$^-$ m/z = 482.98).

Synthesis of **[4.4]**$^-$

To a solution of **[4.3]**$^-$ (890 mg, 1.440 mmol) in methanol (30 mL), sodium methoxide (77.8 mg, 1.440 mmol) was added and stirred at room temperature for 14 h. The reaction mixture was neutralized with IR-120 resin (3g), filtered and washed with 10 mL of methanol. The combined methanol layers were concentrated and purified using column chromatography (silica gel, 12% MeOH in dichloromethane) to yield **[4.4]**$^-$ as a yellow solid (505 mg, 60.5%).

^{1}H NMR (500 MHz, MeOD) δ 4.14 [C_c–*H*, 2H, bs], 4.06 [C_c–*H*, 2H, bs], 3.51 [CH_2O, 2 H, t], 2.50 [CH_2-S, 2 H, t], 1.60 [CH_2-CH_2-O, 2 H, p], 1.58, 1.53 [CH_2-CH_2S, 2 H, dq], 1.42 [CH_2-CH_2CH_2O, 2 H, qd]; ^{11}B NMR (160 MHz, MeOD) δ 23.02 [1B, s], 4.64 [1B, d, ^{1}J(B-H)=140.0], 0.52 [1B, d, ^{1}J(B-H)=142.0], -2.11 [1B, d, ^{1}J(B-H)=144.5], -4.56 [2B, d, ^{1}J(B-H)=142.4], -7.41 [6B, m], -17.20 [2B, d, ^{1}J(B-H)=157.7], -20.46 [2B, d, ^{1}J(B-H)=159.0], -22.05 [1B, d], -28.22

[1B, d, ^{1}J(B-H)=174.3]; ^{13}C NMR (126 MHz, MeOD) δ 69.08, 53.46, 46.70, 33.90, 30.83, 24.71, 23.65. LCMS (ESI) Experimental $[M]^-$ m/z = 440.52 (theoretical $[M]^-$ m/z = 440.94).

Synthesis of **[4.5]$^-$**

To a solution of **[4.3]$^-$** (50 mg, 0.081 mmol) in acetonitrile (2 mL), chloramine-T (37 mg, 0.129 mmol), sodium iodide (15 mg, 0.097 mmol) and acetic acid (130 μL) were added. The reaction mixture was allowed to stir at room temperature for 10 h. After reaction, water (20 mL) was added and extracted with ethyl acetate (3x15 mL), the organic layers were combined and washed with brine solution before drying over anhydrous sodium sulphate. The solvent was evaporated and the crude was purified using column chromatography (silica gel, 10% MeOH in dichloromethane) to yield **[4.5]$^-$** as a yellow solid (25 mg, 41.6%).

^{1}H NMR (500 MHz, MeOD) δ 4.27 [C_c–*H*, 2H, s], 4.13 [C_c–*H*, 2H, s], 3.37 [C*H*$_2$O, 2 H, t], 2.85 [C*H*$_2$-S, 2 H, t], 2.31 [C*H*$_3$, 3 H, s], 1.55 [C*H*$_2$-CH$_2$-O, 2 H, m], 1.45 [C*H*$_2$-CH$_2$S, 2 H, m], 1.36 [C*H*$_2$-CH$_2$CH$_2$O, 2 H, m]; ^{11}B NMR (160 MHz, MeOD) δ 21.47 [1B, s], -0.42[2B, d, ^{1}J(B-H)=145.4], -4.39 [1B, s], -5.71 [4B, d, ^{1}J(B-H)=140.0], -7.27 [4B, d, ^{1}J(B-H)=152.8], -18.07 [2B, d, ^{1}J(B-H)=152.4], -20.04 [2B, d, ^{1}J(B-H)=161.3], -23.45 [1B, d, ^{1}J(B-H)=161.3], -27.37 [1B, d, ^{1}J(B-H)=170.4]; ^{13}C NMR (126 MHz, $CDCl_3$) δ 191.05, 70.24, 58.99, 56.52, 34.78, 33.10, 32.97, 32.52, 29.24. LCMS (ESI) Experimental $[M]^-$ m/z = 606.6 (theoretical $[M]^-$ m/z = 607.6).

Synthesis of **[4.6]$^-$**

To a solution of **[4.5]$^-$** (9 mg, 0.0144 mmol) in methanol (3 mL), sodium methoxide (1 mg, 0.0144 mmol) was added and the resulting solution was allowed to stir at room temperature for 14 h. For the workup, the reaction mixture was neutralized with IR-120 resin (100 mg), filtered and washed with 2 mL of methanol. The combined methanol layer was concentrated and the residue was purified using column chromatography (silica gel, 12% MeOH in dichloromethane) to yield **[4.6]$^-$** as a yellow solid (4.5 mg, 55%).

^{1}H NMR (500 MHz, MeOD) δ 4.28 [C_c–*H*, 2H, s], 4.14 [C_c–*H*, 2H, s], 3.40 [C*H*$_2$O, 2 H, t], 2.67 [C*H*$_2$-S, 2 H, t], 1.66 [C*H*$_2$-CH$_2$-O, 2 H, m], 1.46 [C*H*$_2$-CH$_2$S, 2 H, q], 1.38 [C*H*$_2$-CH$_2$CH$_2$O, 2 H, m]; ^{11}B NMR (160 MHz, MeOD) δ 21.55 [1B, s], -0.34 [2B, d, ^{1}J(B-H)=146.7], -4.32 [1B, s], -5.57 [4B, d, ^{1}J(B-H)=170.0], -6.90 [4B, d], -17.94 [2B, d, ^{1}J(B-H)=167.3], -20.58 [2B, d, ^{1}J(B-H)=153.2], -23.13 [2B, d, ^{1}J(B-H)=266.4], -26.79 [2B, d]; ^{13}C NMR (126 MHz, MeOD) δ 68.68,

56.57, 53.91, 38.38, 31.04, 28.70, 24.81. LCMS (ESI) Experimental $[M]^-$ m/z = 566.64 (theoretical $[M]^-$ m/z = 566.84).

3.5.4. Radiochemistry

The manipulation of radioactive material was carried out in authorised facilities and using the common and personnel protection equipment as described in internal protocols and following current national and international regulations.

Synthesis of ^{124}I-**[4.5]**$^-$

Acetonitrile (200µL) was added to Na[^{124}I]I (50 µL, 37 MBq) and the resulting solution was introduced in a 2.5 mL conic vial. The solvent was evaporated to dryness (100°C, 5 min, constant helium flow at 20 mL/min) and 1 mg of **[4.5]**$^-$ dissolved in acetonitrile (100 µL) was added together with *trans-bis*(acetate)*bis*[o-(di-o-tolylphosphino)benzyl] dipalladium (II) (Herrmann's catalyst, HC, 0.1 mg, 0.101 µmol) dissolved in toluene (100 µL). The reaction mixture was heated at 100°C for 5 min, the solvent was removed under a constant helium flow and the resulting solid was dissolved in 0.5 mL acetonitrile and 30 mL of ultrapure water. The crude solution was passed through a C-18 cartridge (Sep-Pak® Light, Waters) and washed with water (5 mL × 2) to remove free iodine-124. The final product (^{124}I-**[4.5]**$^-$), retained in the C-18 cartridge, was eluted with ethanol (500 µL). The solvent was finally evaporated to dryness. Quality control was performed by radio-HPLC after diluting the solid residue with mobile phase. Analytical conditions were: Stationary phase: Mediterranea Sea18 column (4.6x150 mm, 5 µm particle size, Teknokroma, Spain); mobile phase A: 0.1M ammonium formate (AMF) buffer pH= 3.9; B: acetonitrile; flow rate = 1mL/min; gradient: 0 min: 60% A- 40% B; 2min: 60% A- 40% B; 6min: 20% A- 80% B; 14min: 0% A- 100% B; 16min: 0% A- 100% B; 18min: 60% A- 40% B; 20min: 60% A- 40% B (retention time: 11.5min).

Synthesis of ^{124}I-**[4.6]**$^-$

Dry ^{124}I-**[4.5]**$^-$ obtained from the previous step was dissolved in 250 µL of methanol. Sodium methoxide (2 mg) was added and stirred at room temperature for 6 h. After Completion of the hydrolysis, confirmed by analytical radio-HPLC, reformulation was carried out by dilution with water, retention on a C-18 cartridge (Sep-Pak® Light, Waters), further elution with ethanol (500 µL, Sigma-Aldrich) and evaporation to dryness. Quality control was performed by HPLC.

Analytical conditions were: Stationary phase: Mediterranea Sea18 column (4.6x150 mm, 5 µm particle size, Teknokroma, Spain); mobile phase A: 0.1M ammonium formate (AMF) buffer pH= 3.9; B: acetonitrile; flow rate = 1mL/min; gradient: 0 min: 60% A- 40% B; 2min: 60% A- 40% B; 6min: 20% A- 80% B; 14min: 0% A- 100% B; 16min: 0% A- 100% B; 18min: 60% A- 40% B; 20min: 60% A- 40% B (retention time: 13.1min).

3.5.5. Preparation of AuNPs

Synthesis of citrate-stabilized gold NPs (CIT-AuNPs)

CIT-AuNPs with an average diameter of 18-20 nm and with Au concentration of 1 mg/mL were synthesized following the Turkevich method [6]. In brief, 97.1 mg (0.33 mmol) trisodium citrate dihydrate were dissolved in 150 mL water (concentration = 2.2 mM) and the solution was heated to reflux in a 250 mL three-necked flask equipped with a Dimroth condenser. After 15 min boiling, 1 mL precursor solution ($HAuCl_4 \cdot 3H_2O$ in water, 25 mM) was quickly injected under rapid stirring. When the colour of the solution changed to the characteristic wine-red, which indicates formation of AuNPs, the heating-mantle was switched off but not removed until the temperature of the solution was 70 °C. The resulting NPs were centrifuged at 12000g for 20 min to remove free citrate and resuspended in ultrapure water.

Synthesis of PEG-stabilized, COSAN-functionalized AuNPs (PEG-AuNPs@$[4.4]^-$)

CIT-AuNPs prepared as described above (2 mL) were placed into a vial. Then 100 µL of $mPEG_{5k}$-SH (3 mg/mL) were slowly added under vigorous stirring. After 15 minutes, 100 µL of a fresh solution of **[4.4]**$^-$ in ethanol (3 mg/mL) were quickly added and stirring was maintained for 2h. The resulting NPs were centrifuged at 12000g for 25 min and resuspended in ultrapure water three times.

Synthesis of PEG-AuNPs@$[4.4]^-$ labeled at the core

CIT-AuNPs prepared as described above (2 mL) were placed into a vial. [^{124}I]NaI (15 µL, solution in 0.1M NaOH) was added and the solution was stirred for 10 min. Then, $mPEG_{5k}$-SH (100 µL, 3 mg/mL) was slowly added under vigorous stirring. After 15 minutes, 100 µL of a fresh solution of **[4.4]**$^-$ in ethanol (3 mg/mL) were quickly added and stirring was maintained for

2h. The resulting NPs were centrifuged at 12000g for 25 min and resuspended in ultrapure water three times.

Synthesis of PEG-stabilized, COSAN-functionalized AuNPs labeled at the shell

CIT-AuNPs prepared as described above (1 mL) were placed into a vial. Then, $mPEG_{5k}$-SH (100 µL, 3 mg/mL) was slowly added under vigorous stirring. After 15 minutes, 100 µL of a fresh solution of **[4.4]**$^-$ in ethanol (3 mg/mL) and freshly prepared ^{124}I-**[4.6]**$^-$ (22.2 MBq) dissolved in ethanol (15 µL) were quickly added and stirring was maintained for 2h. The resulting NPs were centrifuged at 12000g for 25 min and resuspended in ultrapure water three times.

3.5.6. *In vivo* experiments

Animals

The animals were maintained and handled in accordance with the Guidelines for Accommodation and Care of Animals (European Convention for Protection of Vertebrate Animals Used for Experimental and Other Scientific Purposes) and internal guidelines. Experimental procedures were approved by the ethical committee and local authorities. All animals were housed in ventilate cages and fed on standard diet *ad libitum*.

HT1080 mouse tumor model development

In order to study the biodistribution of the labeled AuNPs in tumor-bearing mice, Rj:NMRI-*Foxn1*$^{nu/nu}$ female mice (7-8 weeks old, Janvier) were subcutaneously inoculated with 2×10^6 HT1080 tumor cells in to the right flank. Prior to each inoculation, cells were diluted in sterile PBS:Matrigel (1:1) and Mycoplasma test (Lonza) was carried out to ensure that cells were not contaminated. Mice weights were measured daily. Tumors were measured and recorded 3 times per week with a digital caliper and volumes were calculated as V (mm^3) = [(short diameter)^2 x (long diameter)]/2. Biodistribution studies were carried out when tumor volume was approximately 200–300 mm^3 (~15-20 days after tumor inoculation).

Biodistribution studies

PET studies with labeled NPs were carried out in mice (n=2 per compound) using an eXplore Vista-CT small animal PET-CT system (GE Healthcare). Anaesthesia was induced with 5% isoflurane and maintained by 1.5 to 2% of isoflurane in 100% O_2. For intravenous administration

of the radiotracer, the tail vein was catheterized with a 24-gauge catheter and the labeled NPs (3.8±0.6 MBq for NPs labeled at the core; 2.7±0.3 MBq for NPs labeled at the shell, volume=150 μL) were injected concomitantly with the start of a PET dynamic acquisition. Mice were kept normothermic throughout the scans using a heating blanket (Homeothermic Blanket Control Unit; Bruker).

Whole body scans were acquired just after administration during 60 min. At time points 10 h, 24 h, 72 h and 144h, 30 min whole body static acquisitions were performed. All the scans were recorded in the 400-700 KeV energetic window. CT acquisitions were also performed at the end of each PET scan, providing anatomical information for unambiguous localization of the radioactive signal and the attenuation map for PET image reconstruction.

PET images were reconstructed (decay and CT-based attenuation corrected) with filtered back projection (FBP) using a Ramp filter with a cut off frequency of 1 Hz. Images were analysed using PMOD image analysis software (PMOD Technologies Ltd, Zürich, Switzerland). With that aim, volumes of interest (VOIs) were manually drawn in the lungs, liver, bladder, stomach, kidneys, spleen, tumor, heart and thyroid gland using the CT images as anatomical reference. VOIs were then transferred to the PET images and time activity curves (decay corrected) were obtained for each organ as cps/cm^3. Curves were transformed into real activity (Bq/cm^3) curves. Injected dose normalization was finally applied to data to get time activity curves as percentage of injected dose per cm^3 of tissue.

Ex vivo Studies

Ion beam microscopy (IBM) studies were performed at the LIPSION nanoprobe at Leipzig University using a 2.25 MeV proton beam with a spot size of approximately 1 μm and supplied by Singletron™ particle accelerator (HVEE, Amersfoort, NL). Under vacuum of 10^{-6} Torr two ion beam microscope techniques, such as micro-proton induced X-ray emission (μPIXE) and micro-Rutherford backscattering (μRBS), were used simultaneously to study the spatial distribution of elements originated from tissue and NPs. Extracted μRBS spectra from the region of interest were analyzed by using SIMNRA 6.06 software (Dr. Matej Mayer, MPI of plasmaphysic, Garching, GE) to determine accumulated charge, area density (atoms/cm^2) and element matrix composition (C, N, O). These parameters were used as input for μPIXE analysis by means of GeoPIXE 5.1 software (CSIRO Earth Science and Resource Engineering, Clayton,

Australia) to quantify element concentration in the tissue of NP treated mice. The detailed procedure is described elsewhere [29, 35].

Confocal Raman microspectroscopy (CRM) analyses were performed using an Alpha300 R microscope (WITec GmbH, Ulm, Germany) equipped with a 532 nm laser source, a 600 g mm^{-1} grating and a charge-coupled device (CCD) cooled down to −61 °C. All measurements were conducted using a 63x water immersion objective (W Plan-Apochromat 63x/1.0, Zeiss, Oberkochen, Germany). Raman spectra were collected pixel-wise in x-y plane with an integration time of about 70 µs. Acquired spectra were processed using the Project FOUR PLUS 4.0 software (WITec GmbH, Ulm, Germany).

3.6. References

1. Barth RF, Vicente MGH, Harling OK, Kiger Iii WS, Riley KJ, Binns PJ, Wagner FM, Suzuki M, Aihara T, Kato I, Kawabata S. Current status of boron neutron capture therapy of high grade gliomas and recurrent head and neck cancer. *Radiation Oncology*. **2012**;7(1).

2. Sauerwein WAG, Bet PM, Wittig A. Drugs for BNCT: BSH and BPA. Neutron Capture Therapy: Principles and Applications2012. p. 117-60.

3. Brust M, Walker M, Bethell D, Schiffrin DJ, Whyman R. Synthesis of thiol-derivatised gold nanoparticles in a two-phase liquid-liquid system. *Journal of the Chemical Society, Chemical Communications*. **1994**(7):801-2.

4. Ciani L, Bortolussi S, Postuma I, Cansolino L, Ferrari C, Panza L, Altieri S, Ristori S. Rational design of gold nanoparticles functionalized with carboranes for application in Boron Neutron Capture Therapy. *International Journal of Pharmaceutics*. **2013**;458(2):340-6.

5. Cioran AM, Musteti AD, Teixidor F, Krpetić Z, Prior IA, He Q, Kiely CJ, Brust M, Viñas C. Mercaptocarborane-capped gold nanoparticles: Electron pools and ion traps with switchable hydrophilicity. *Journal of the American Chemical Society*. **2012**;134(1):212-21.

6. Turkevich J, Stevenson PC, Hillier J. A study of the nucleation and growth processes in the synthesis of colloidal gold. *Discussions of the Faraday Society*. **1951**;11:55-75.

7. Walkey CD, Olsen JB, Guo H, Emili A, Chan WCW. Nanoparticle size and surface chemistry determine serum protein adsorption and macrophage uptake. *Journal of the American Chemical Society*. **2012**;134(4):2139-47.

8. Van Vlerken LE, Vyas TK, Amiji MM. Poly(ethylene glycol)-modified nanocarriers for tumor-targeted and intracellular delivery. *Pharmaceutical Research*. **2007**;24(8):1405-14.

9. Jokerst JV, Lobovkina T, Zare RN, Gambhir SS. Nanoparticle PEGylation for imaging and therapy. *Nanomedicine*. **2011**;6(4):715-28.

10. Bregadze VI, Sivaev IB. Polyhedral boron compounds for BNCT. Boron Science: New Technologies and Applications2016. p. 181-207.

11. Shao X, Zhang H, Rajian JR, Chamberland DL, Sherman PS, Quesada CA, Koch AE, Kotov NA, Wang X. 125I-labeled gold nanorods for targeted imaging of inflammation. *ACS Nano*. **2011**;5(11):8967-73.

12. Llop J, Masalles C, Viñas C, Teixidor F, Sillanpää R, Kivekäs R. The [3,3′-Co(1,2-$C_2B_9H_{11})_2$]-anion as a platform for new materials: Synthesis of its functionalized monosubstituted derivatives incorporating synthons for conducting organic polymers. *Journal of the Chemical Society Dalton Transactions*. **2003**(4):556-61.

13. Gabel D, Foster S, Fairchild RG. The Monte Carlo simulation of the biological effect of the $^{10}B(n,\alpha)^7Li$ reaction in cells and tissue and its implication for boron neutron capture therapy. *Radiation Research*. **1987**;111(1):14-25.

14. Cioran AM, Teixidor F, Krpetić Ž, Brust M, Viñas C. Preparation and characterization of Au nanoparticles capped with mercaptocarboranyl clusters. *Dalton Transactions*. **2014**;43(13):5054-61.

15. Vigderman L, Zubarev ER. Therapeutic platforms based on gold nanoparticles and their covalent conjugates with drug molecules. *Advanced Drug Delivery Reviews*. **2013**;65(5):663-76.

16. Stylianopoulos T. EPR-effect: Utilizing size-dependent nanoparticle delivery to solid tumors. *Therapeutic Delivery*. **2013**;4(4):421-3.

17. Niţica S, Moldovan AI, Toma V, Moldovan CS, Berindan-Neagoe I, Ştiufiuc G, Lucaciu CM, Stiufiuc R. PE gylated gold nanoparticles with interesting plasmonic properties synthesized using an original, rapid, and easy-to-implement procedure. *Journal of Nanomaterials*. **2018**;2018.

18. NIST X-ray Photoelectron Spectroscopy Database [database on the Internet]. National Institute of Standards and Technology, Gaithersburg MD, 20899 (2000). [cited April 2019].

19. Llop J, Gómez-Vallejo V, Martín IG, Marradi M. Radiolabelling of Nanoparticles Using Radiohalogens, ^{13}N, and ^{11}C. Isotopes in Nanoparticles: Fundamentals and Applications2016. p. 231-60.

20. Martín IG, Frigell J, Llop J, Marradi M. Radiolabelling of NPs using radiometals: ^{99m}Tc, ^{68}Ga, ^{67}Ga, ^{89}Zr, and ^{64}Cu. Isotopes in Nanoparticles: Fundamentals and Applications2016. p. 183-229.

21. Llop J, Jiang P, Marradi M, Gómez-Vallejo V, Echeverría M, Yu S, Puigivila M, Baz Z, Szczupak B, Pérez-Campaña C, Mao Z, Gao C, Moya SE. Visualisation of dual radiolabelled poly(lactide-co-glycolide) nanoparticle degradation in vivo using energy-discriminant SPECT. *Journal of Materials Chemistry B*. **2015**;3(30):6293-300.

22. Gona KB, Zaulet A, Gómez-Vallejo V, Teixidor F, Llop J, Viñas C. COSAN as a molecular imaging platform: Synthesis and "in vivo" imaging. *Chemical Communications*. **2014**;50(77):11415-7.

23. Agarwal A, Shao X, Rajian JR, Zhang H, Chamberland DL, Kotov NA, Wang X. Dual-mode imaging with radiolabeled gold nanorods. *Journal of Biomedical Optics*. **2011**;16(5).

24. Iceta LG, Gómez-Vallejo V, Koziorowski JM, Llop J. Radiochemical stability studies of radiolabelled nanoparticles. Isotopes in Nanoparticles: Fundamentals and Applications2016. p. 429-53.

25. Kaushal A, Citrin D. The Role of Radiation Therapy in the Management of Sarcomas. *Surgical Clinics of North America*. **2008**;88(3):629-46.

26. Arnida, Janát-Amsbury MM, Ray A, Peterson CM, Ghandehari H. Geometry and surface characteristics of gold nanoparticles influence their biodistribution and uptake by macrophages. *European Journal of Pharmaceutics and Biopharmaceutics*. **2011**;77(3):417-23.

Chapter 4: Gold Nanoparticles as boron carriers for BNCT (II)

4.1. Introduction

As mentioned in the previous chapter, gold nanoparticles (AuNPs) have attracted increasing attention in a wide range of biomedical applications due to their unique optical, physical and chemical properties [1, 2]. Due to their non-toxic nature and biocompatibility, we considered them as potential boron carriers for boron neutron capture therapy (BNCT). This said, it is worth mentioning that both the core size and the surface functionalization of the NPs play a pivotal role when applied in biomedicine. First, it is well known that the surface-to-volume ratio of AuNPs is inversely proportional to their size; the smaller the particle, the higher the surface-to-volume ratio, and high surface-to-volume ratios offer the possibility to attach a higher amount of drug, targeting moieties or stabilizers on the surface.

In our particular case, the possibility to incorporate a higher amount of boron on the surface of the particles should lead to higher therapeutic efficacy while using a lower net amount of AuNPs, with the consequent decrease both in cost and eventual off-target side effects.

Besides the above mentioned effect, the size of the AuNPs in drug delivery also plays an important role in the general biodistribution. Small core-sized AuNPs, when properly stabilized, have prolonged plasma circulation time due to the fact that larger AuNPs are more easily cleared by the Mononuclear Phagocytic System (MPS), previously known as reticuloendothelial system (RES). Terentyuk et al. reported that 15 nm AuNPs showed prolonged blood circulation time and concentrations in the plasma than those of 50 and 160 nm 24 h after injection [3]. Therefore, for prolonging circulation of AuNPs and enable higher tumor accumulation, tuning surface functionality and core sizes are important factors.

In the previous chapter, we have evaluated AuNPs (core size 18-21 nm) stabilized with polyethylene glycol (PEG) and functionalized with the boron-rich anion cobalt bis(dicarbollide). The incorporation of the positron emitter ^{124}I enabled the pharmaciokinetic evaluation (biodistribution, elimination) of the NPs by means of Positron Emission Tomography (PET). Additionally, incorporation of the label in different positions (core and shell) confirmed stability *in vivo* of the NPs. Despite the suitability of this approach, high accumulation of the NPs in the liver suggested that the core size was probably too large, resultin in a very low accumulation of

the NPs in the tumor. Additionally, minor accumulation of radioactivity in the stomach and the thyroid gland confirmed progressive detachment of the radiolabel, thus suggesting that the radiolabeling strategy was not optimal. These results pointed to the need to slightly modify particle size and radiolabeling strategy in subsequent studies.

In this chapter, as a second approach for the development of gold NP-based BNCT agents, we decided to prepare spherical gold NPs with smaller sizes, this is, with core sizes of ~3-4 nm (named GNSs) and ~9-11 nm (named GNSm). In both cases, NPs were stabilized with PEG-thiol. For the tracking *in vivo*, the positron emitter copper-64 (^{64}Cu, half-life of 12.7 hours) was incorporated at the core by adapting previously reported methods [4, 5]. As the boron source, we used the boron cluster **[4.4]**$^-$ (see chapter 3) on the gold surface via Au-thiol interaction. PET studies were carried out in a mouse model of human gastrointestinal adenocarcinoma, generated by subcutaneous inoculation of MKN45 human cells in nude mice, in order to assess the *in vivo* stability of the size tuned multifunctionalized GNSs and GNSm and their capability to accumulate in the tumor by passive targeting (Scheme 4.1).

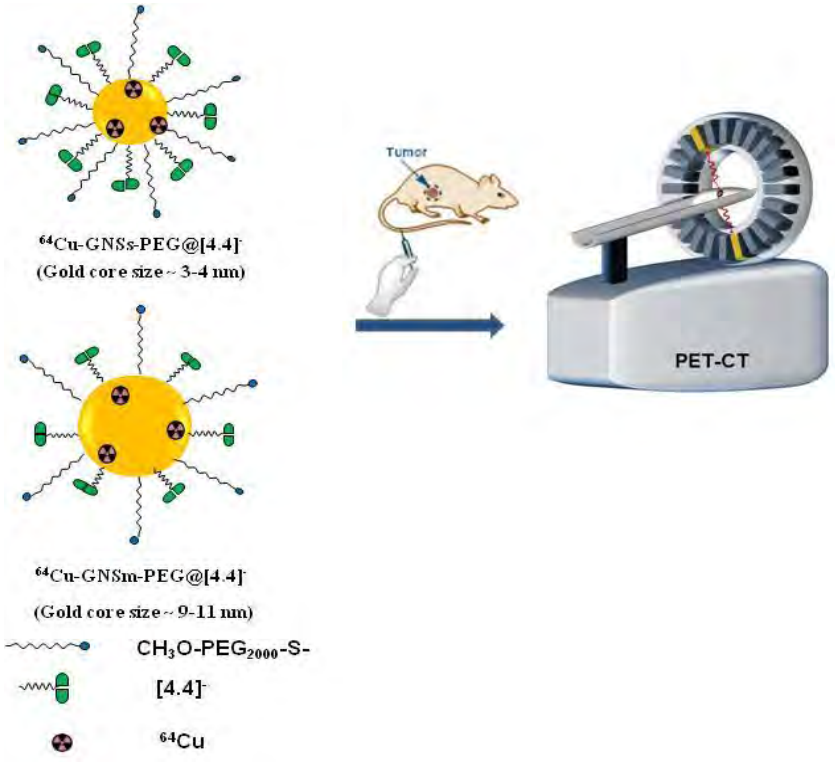

Scheme 4.1. General scheme of the experimental part of this chapter. Radiolabeled multifunctionalized ^{64}Cu alloyed GNSs and GNSm nanosystems were evaluated by positron emission tomography (PET) imaging after intravenous administration in a mouse model of gastrointestinal adenocarcinoma.

4.2 Objectives

The specific objectives of this chapter are:

1- To synthesize and characterize stable and biocompatible copper alloyed, size-tuned small (GNSs) and medium gold nanospheres (GNSm) functionalized with PEG and COSAN.

2- To develop strategies for the radiolabeling of the nanosystems with the positron emitter ^{64}Cu.

3- To perform *in vitro* studies (cytotoxicity and cell internalization) of multifunctionalized GNSs and GNSm in different cell lines.

4- To evaluate the pharmacokinetic properties of the novel multifunctionalized GNSs and GNSm using positron emission tomography (PET) in a human gastrointestinal adenocarcinoma mouse model (MKN45 human cell line) after intravenous administration.

4.3 Results and Discussion

4.3.1 Synthesis and Characterization of the gold nanospheres

The synthesis of [3,3'-Co(1,2-$C_2B_9H_{10}$)(8'-O-$(CH_2)_5$-SH-1',2'-$C_2B_9H_{11}$)]- (**[4.4]**$^-$) was designed to generate thiol group-bearing COSAN derivatives for easy attachment to small sized gold nanospheres (GNSs, core size ~3-4 nm) and medium-sized gold nanospheres (GNSm, core size ~9-11 nm). The boron-rich ligand was prepared as described in Chapter 3.

For the preparation of the nanoparticles, we first tackled the synthesis of stabilized, copper-alloyed small gold nanoparticles (Cu-GNSs@PEG) by using previously published protocols with slight modifications [5]. In brief, non-radioactive copper chloride dihydrate ($CuCl_2.2H_2O$) and $HAuCl_4$ were dissolved in water, followed by the addition of methoxy poly(ethylene glycol) methyl ether thiol (mPEG-SH, 2 kDa). After 2 min, a sodium borohydride ($NaBH_4$) solution was added under quick stirring for 2 min. The reaction was allowed to occur for 2 h at room temperature prior to centrifugation (Figure 4.1).

Next, we prepared copper alloyed medium gold nanoparticles (Cu-GNSm@PEG), also following previously reported methods with slight modifications [6]. In brief, $HAuCl_4$, copper(II) acetylacetonate ([$Cu(acac)_2$]) and 1,2-hexadecanediol were mixed and oleylamine was used as a solvent and reducing agent in the reaction. The reaction solution was heated in a microwave to 160°C with a programmed temperature ramp of 4°C/min. Then, the reaction mixture was held at

160°C for 2 h prior to cooling to room temperature. After centrifugation, the hydrophobic Cu-GNSm NPs were dissolved in hexane to form a homogeneous reddish solution. Subsequently, the hydrophobic Cu-GNSm NPs were modified with a thiol-terminated poly(ethylene glycol) (methoxy-PEG-SH, 2 kDa). With that aim, $mPEG_{2k}$-SH was dissolved in water and added dropwise to the Cu-GNSm NPs in a tetrahydrofuran (THF) solution and stirred for 24 h at room temperature prior to centrifugation to get hydrophilic Cu-GNSm@PEG (Figure 4.2).

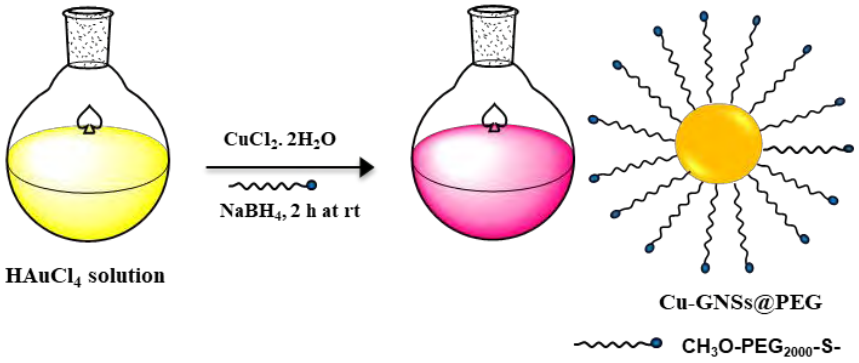

Figure 4.1. Schematic representation of the preparation of Cu-GNSs@PEG.

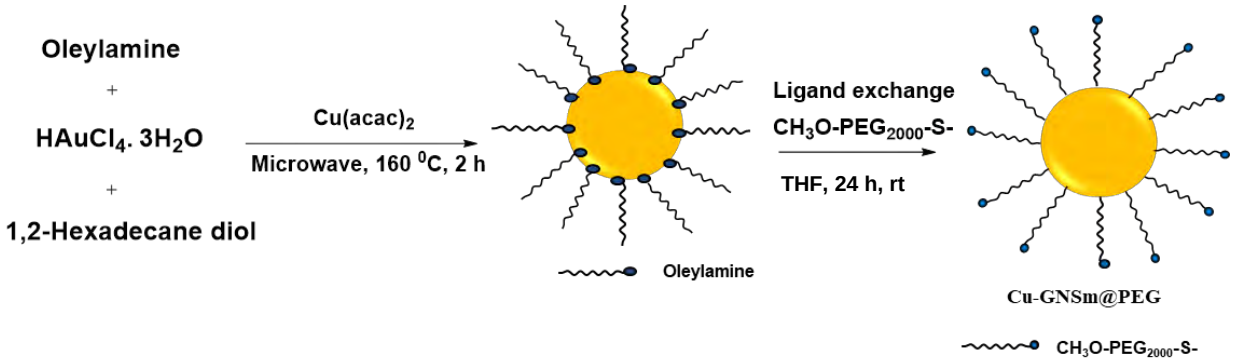

Figure 4.2. Schematic representation of the preparation of Cu-GNSm@PEG

In the next step, PEG-stabilized GNSs and GNSm NPs were functionalized with COSAN-thiol ([**4.4**]$^-$). With that aim, compound [**4.4**]$^-$ was dissolved in ethanol, and this solution was added to the Cu-PEG-GNSs and Cu-PEG-GNSm solution drop-wise. The resulting solution was stirred for 2 h at RT and purified by centrifugation to get Cu-GNSs-PEG@[4.4]$^-$ (Figure 4.3) and Cu-GNSm-PEG@[4.4]$^-$ (Figure 4.4).

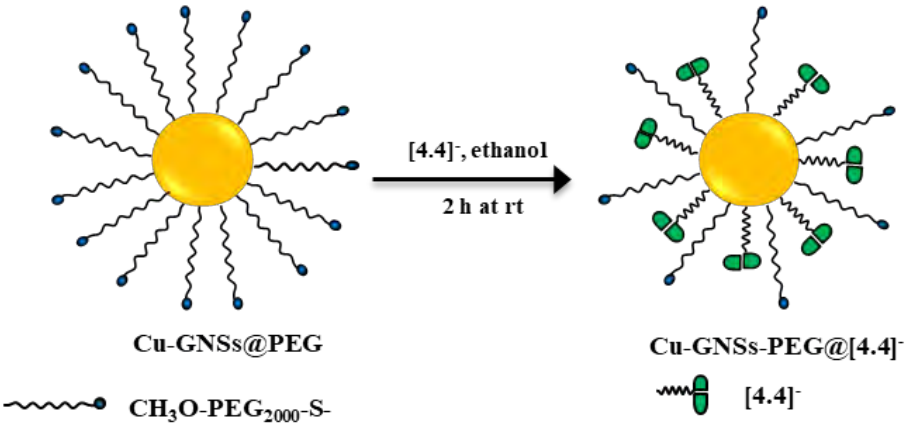

Figure 4.3. Schematic representation of the preparation of Cu-GNSs-PEG@[4.4]$^-$

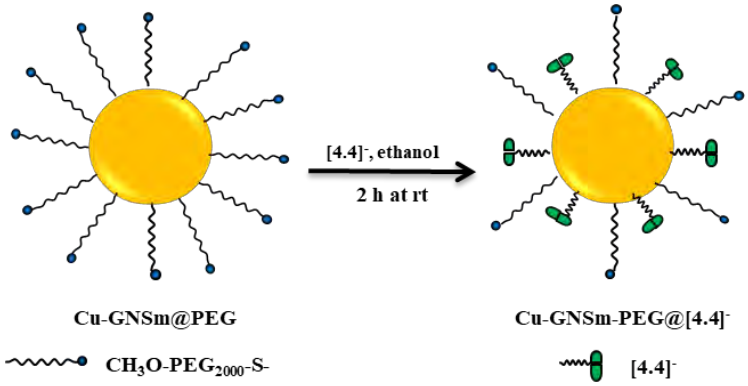

Figure 4.4. Schematic representation of the preparation of Cu-GNSm-PEG@[4.4]$^-$

One of the important parameters to take into consideration when preparing new BNCT drug candidates is the boron-load capacity. In order to check the loading capacity of **[4.4]**$^-$ on Cu-PEG-GNSs and Cu-PEG-GNSm, optimization studies were performed by adding different amounts of **[4.4]**$^-$ (GNSs/GNSm to **[4.4]**$^-$ molar ratios: 1, 2 and 0.66) to the nanosystems. The absorbance and loading capacity of both nanosystems after purification was analyzed by UV-vis absorption spectroscopy (UV-Vis). The surface functionalized nanosystems showed a longitudinal surface plasmon resonance (LSPR) band at 521 nm for Cu-GNSs-PEG@[4.4]$^-$, while for Cu-GNSm-PEG@[4.4]$^-$ the LSPR band observed at 529 nm. Additionally, another absorption band appeared at ca. 310 nm, close to the maximum absorption of COSAN (314 nm), confirming successful attachment of the boron cluster on the surface of the Cu-GNSs-PEG@[4.4]$^-$ and Cu-GNSm-PEG@[4.4]$^-$ nanosystems (Figure 4.5). In all experimental scenarios, NPs showed good stability,

and hence we decided to move forward using the NPs prepared with a GNSs/GNSm to **[4.4]**$^-$ molar ratio of 0.66, as this was expected to result in the higher concentration of boron on the NPs.

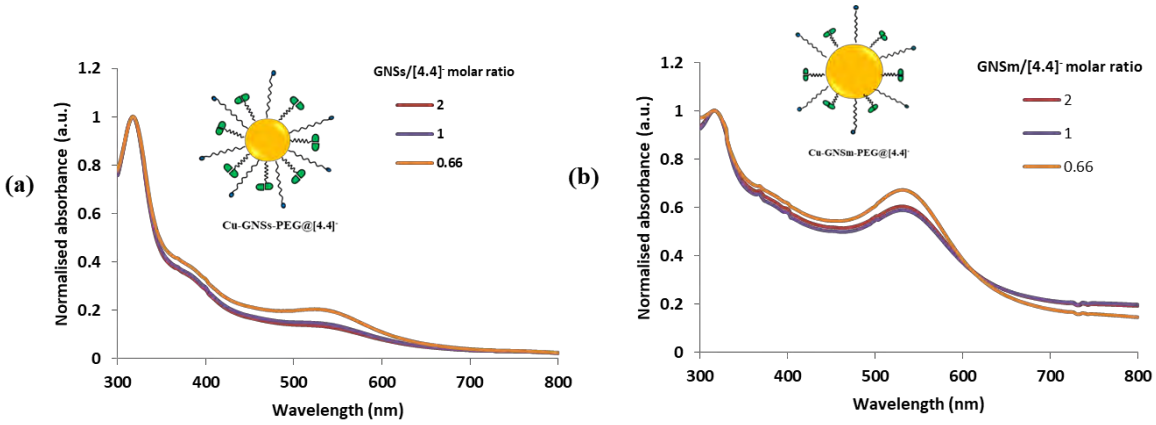

Figure 4.5. UV-vis-NIR spectra of Cu-GNSs-PEG@[4.4]$^-$ and Cu-GNSm-PEG@[4.4]$^-$ with different molar ratios of GNSs or GNSm to [4.4]$^-$.

Transmission electron microscopy (TEM) images showed that Cu-GNSs-PEG@[4.4]$^-$ had uniform distribution with a core diameter of 3.5 ± 1.8 nm (Figure 4.6a) and zeta potential measurements showed a negative ξ-potential of −36.0±2 mV (Figure 4.6b).

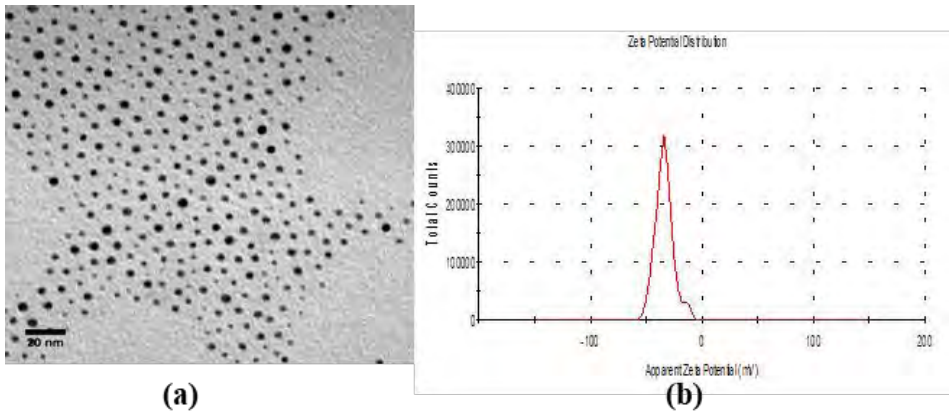

Figure 4.6. Transmission electron micrograph (TEM) (a) and Zeta potential distribution for Cu-GNSs-PEG@[4.4]- (-36±2 mV).

Cu-GNSm-PEG@[4.4]$^-$ showed the similar uniform distribution with a core diameter of 9.5 ± 2.5 nm (Figure 4.7a), and a negative ξ-potential of −19.0±2 mV (Figure 4.7b) at neutral pH. The negative zeta potential values confirm the incorporation of the anionic COSAN complex on the surface of both nanosystems.

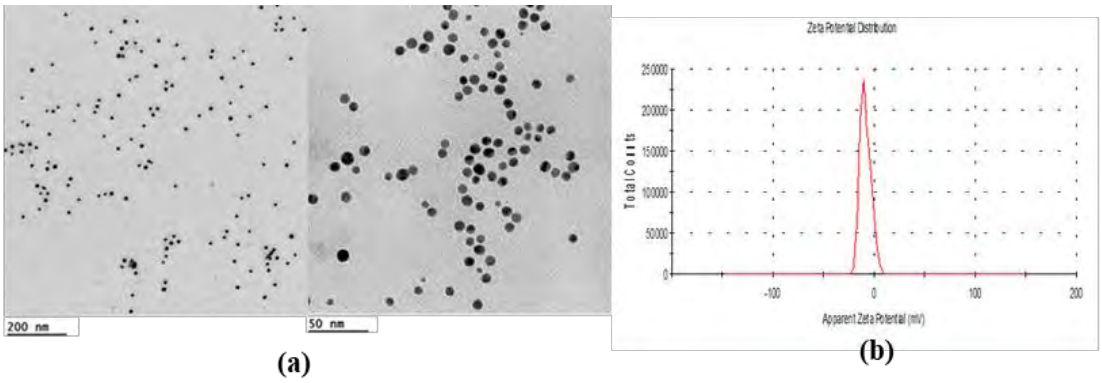

Figure 4.7. Transmission electron micrographs (TEM) (a) and Zeta potential distribution for Cu-GNSm-PEG@[4.4]$^-$ (-19±2 mV) (b).

As additional structural evidence, the presence of COSAN on the surface of gold nanoparticles was confirmed by X-ray photoelectron spectroscopy (XPS). XPS analysis of Cu-GNSs-PEG@[4.4]$^-$ and Cu-GNSm-PEG@[4.4]$^-$ showed boron and cobalt peaks at 780.2 eV and 192.8 eV respectively (Figure 4.8) [7].

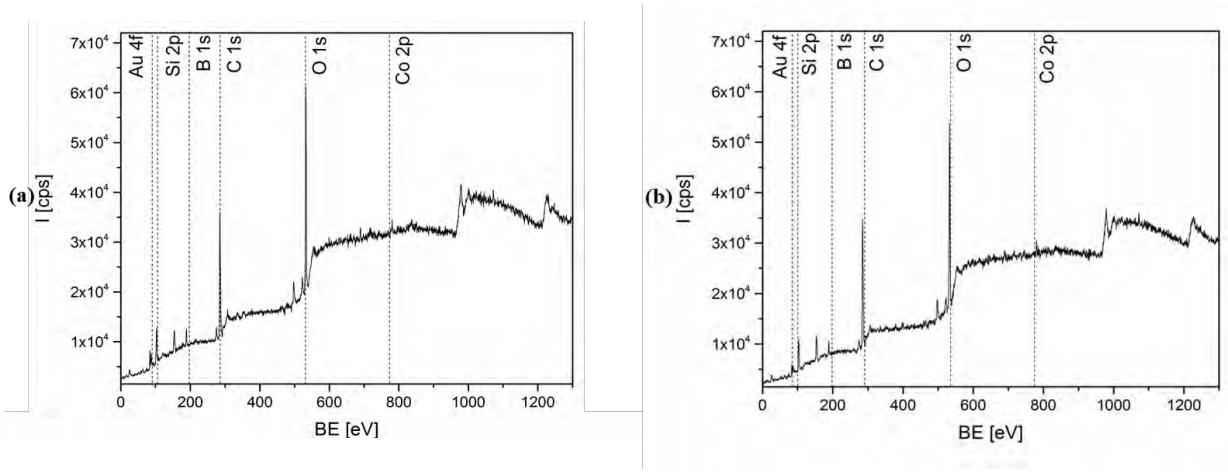

Figure 4.8. XPS spectra of Cu-GNSs-PEG@[4.4]$^-$ (a) and Cu-GNSm-PEG@[4.4]$^-$ (b).

The relative quantification of carbon, oxygen, boron and cobalt present in the samples was carried out (Table 4.1). The quantification data showed that Cu-GNSs-PEG@[4.4]$^-$ have a higher

amount of boron when compared with Cu-GNSm-PEG@[4.4]$^-$. These results confirmed the presence of both boron and cobalt on the surface of both nanosystems.

Table 4.1. Elemental composition of different elements present in the Cu-GNSs-PEG@[4.4]$^-$ and Cu-GNSm-PEG@[4.4]$^-$ nanosystems measured by XPS analysis.

	C(at.%)	O(at.%)	Co(at.%)	B(at.%)
Cu-GNSs-PEG@[4.4]$^-$	46.5	26.1	0.4	13.4
Cu-GNSm-PEG@[4.4]$^-$	48.4	25.4	0.3	8.9

In order to determine the loading capacity of the both nanosystems, ICP-MS analysis were performed to measure the gold and boron content in the final Cu-GNSs-PEG@[4.4]$^-$ and Cu-GNSm-PEG@[4.4]$^-$, (GNSs and GNSm to **[4.4]$^-$** molar ratios 0.66). The amount of **[4.4]$^-$** was in Cu-GNSs-PEG@[4.4]$^-$ estimated to be 472 µg per mg of gold, which results in ca. 210 µg of boron/mg of gold. The amount of **[4.4]$^-$** in Cu-GNSm-PEG@[4.4]$^-$ was calculated to be 348 µg per mg of gold, which results in ca. 155 µg of boron/mg of gold. These results confirm that both Cu-GNSs-PEG@[4.4]$^-$ and Cu-GNSm-PEG@[4.4]$^-$ have a significant boron load and ready for for eventual *in vitro* and *in vivo* studies.

4.3.2. *In vitro* studies

Cytotoxicity studies

To determine cytotoxicity of the Cu-GNSs-PEG@[4.4]$^-$ and Cu-GNSm-PEG@[4.4]$^-$, human dermal fibroblasts (HDFa), MKN-45 gastric adenocarcinoma cells and 3T3 cells (cell line originally established from primary mouse embryonic fibroblast cells) were treated with 20, 40, and 60 µM (gold concentration) of the nanosystems for up to 72 hours prior to analysis using the MTT assay. Both nanosystems did not induce cell death at up to 60 µM (gold concentration) in any of the tested cell lines (Figure 4.9), indicating negligible cytotoxicity.

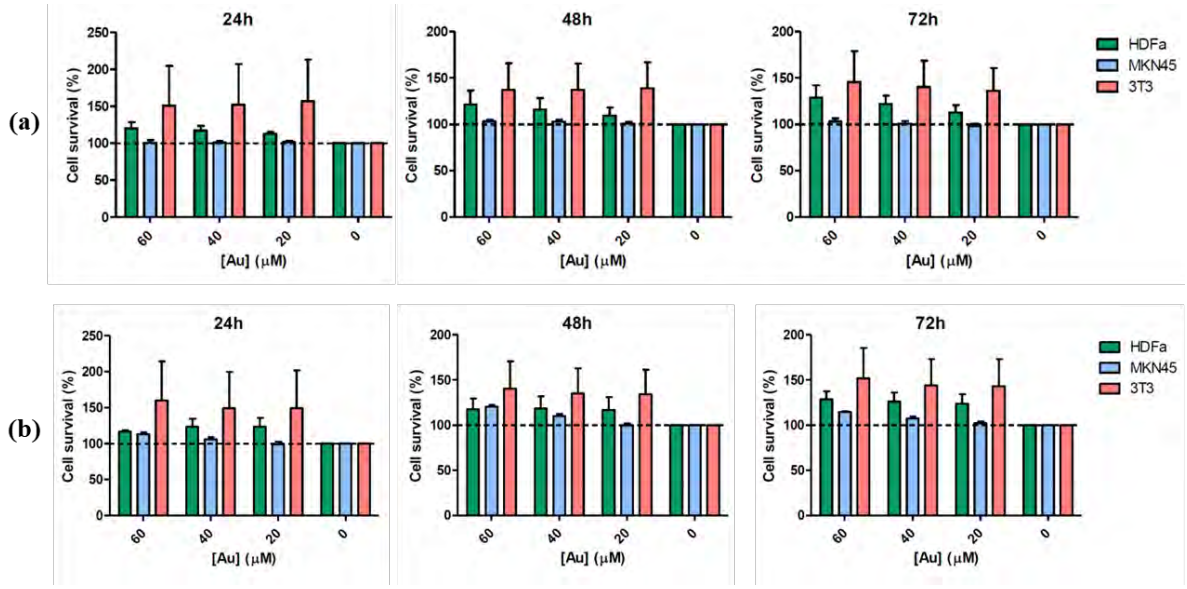

Figure 4.9. Cell viability in the presence of Cu-GNSs-PEG@[4.4]$^-$ (a) and Cu-GNSm-PEG@[4.4]$^-$ (b), for 24, 48 and 72 hours: a) human (HDFa) dermal fibroblasts; b) MKN-45 gastric cell line and c) 3T3 healthy mouse cell line. In all cases, cells were incubated with increasing concentrations of GNSs and GNSm and cell viability was determined by the MTT assay. Data are shown as the mean ± standard deviation of three independent experiments.

Cell internalization studies

The cellular uptake of multifunctionalized GNSs and GNSm was evaluated in MKN-45 cells using fluorescence microscopy. For that purpose, the first step was to incorporate a fluorescent moiety in the NPs. With that aim, Cu-GNSs-PEG@[4.4]$^-$ was reacted with PEG-amine-thiol (5 kDa) at room temperature for 2 h and centrifuged at 14000 rpm for 10 min and washed two times with water. Then, Cyanine 3 N-hydroxysuccinimide ester (Cy3-NHS) dissolved in DMSO was added to the amino-functionalized Cu-GNSs-PEG@[4.4]$^-$ (pH 7.4-8.0) and stirred for 2 h at room temperature. The resulting particles were centrifuged at 14000 rpm for 10 min and washed two times with water. A parallel synthesis strategy was applied to prepare fluorophore-labeled Cu-GNSm-PEG@[4.4]$^-$ NPs.

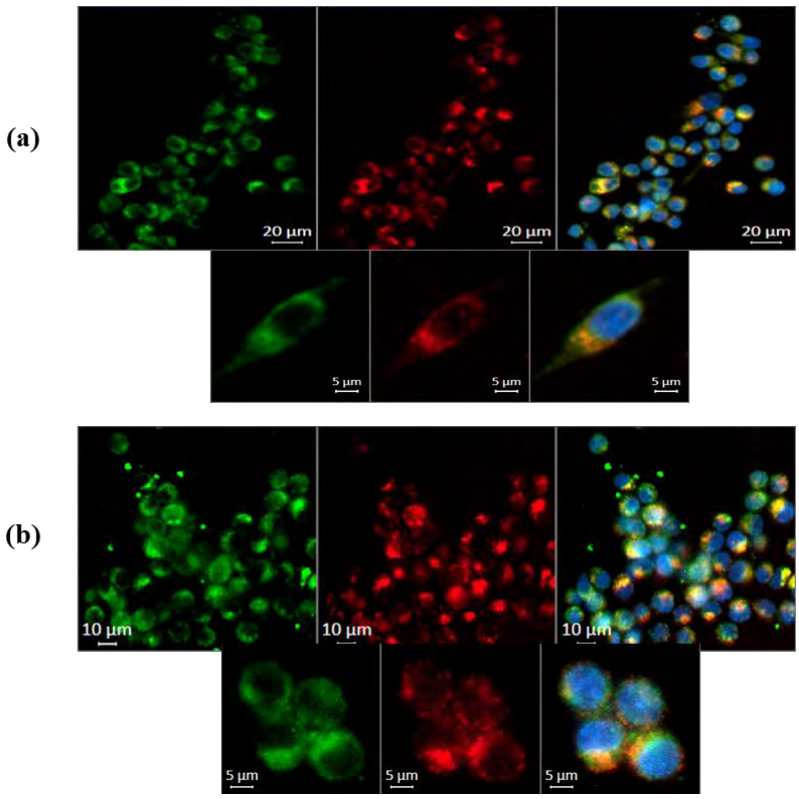

Figure 4.10. Live cell fluorescence microscopy of multifunctionalized GNSs and GNSm after 2 h incubation with MKN45 cells. In green: Cu-GNSs-mPEG@[4.4]$^-$ (a) and Cu-GNSm-mPEG@[4.4]$^-$ (b), fluorophore-labeled with NHS-Cy3, in red: Lysosomes, stained with LysoTracker deep red, in blue: nucleus, stained with Hoechst33342. Merged signals of fluorophore-labeled (a) and (b), colocalizing with lysosomes appear in yellow.

Both fluorophore-labeled NPs (Cu-GNSs-PEG@[4.4]$^-$ and Cu-GNSm-PEG@[4.4]$^-$) were incubated with MKN45 cells for 2 h. To enable visualization of co-localization between the fluorophore-labeled Cu-GNSs-PEG@[4.4]$^-$ and Cu-GNSm-PEG@[4.4]$^-$ with the lysosomes, the lysosomes were stained with Lysotracker-deep-red. Images were taken using a live cell Axio Observer (Zeiss) fluorescence microscope and analyzed by the ZEN-ZEISS software, showing a clear co-localization of Cu-GNSs-PEG@[4.4]$^-$ and Cu-GNSm-PEG@[4.4]$^-$ and the lysosomes (Figure 4.10). Our results confirm that both nanosystems can efficiently internalize in MKN45 cells in 2 hours.

4.3.3. Radiolabeling of nanoparticles

Radiolabeled GNSs and GNSm with the positron emitter ^{64}Cu were synthesized by using previously published protocols with minor modifications [5, 6]. In brief, ^{64}Cu-GNSs-PEG@[4.4]$^-$

labeled NPs were synthesized as Cu-GNSs-PEG@[4.4]$^-$ NPs, but radioactive [^{64}Cu]$CuCl_2$ was added instead of $CuCl_2.2H_2O$ (Figure 4.11). In order to remove all the ^{64}Cu absorbed on (or loosely bound to) the NPs, the synthesized ^{64}Cu-GNSs-PEG NPs were challenged with ethylenediaminetetraacetic acid (EDTA, 10 mM in neutral 50 mM phosphate buffer, 5 μL), and then purified using a centrifuge filter (Amicon, MWCO 10 kDa). The radiochemical purity was above 95%, as determined by instant radio-thin layer chromatography (radioTLC) (Figure 4.12). In the second step [4.4]$^-$ was attached as described in non-radioactive Cu-GNSs-PEG@[4.4]$^-$ preparation (Figure 4.12). After purification, the radiochemical yield of ^{64}Cu-GNSs-PEG@[4.4]$^-$ was 15% and purity was above 98% (Figure 4.13).

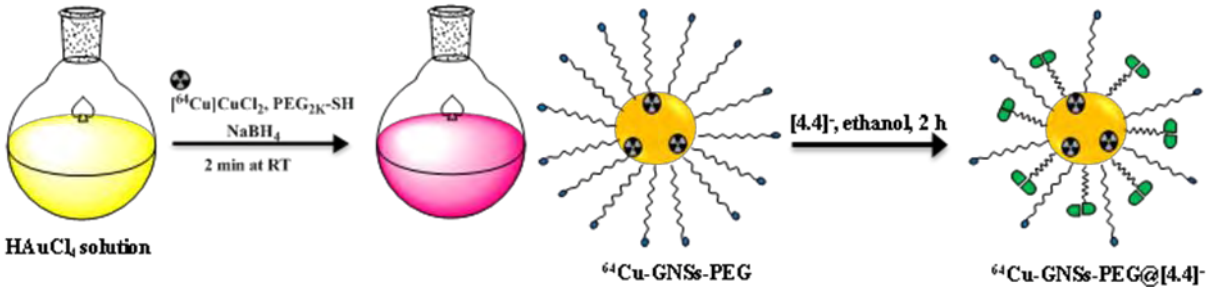

Figure 4.11. Schematic representation of the preparation of ^{64}Cu-GNSs-PEG@[4.4]$^-$.

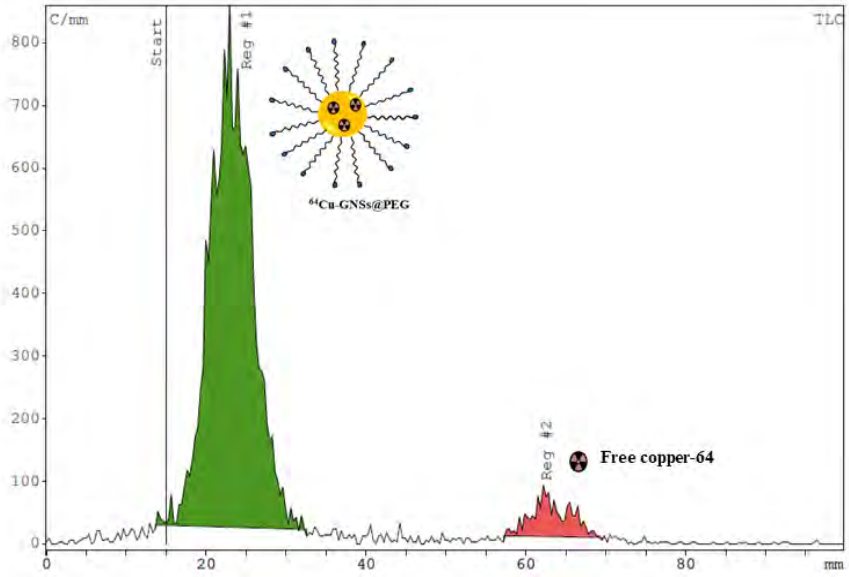

Figure 4.12. Radiochemical purity of ^{64}Cu-GNSs-PEG analyzed by radioTLC.

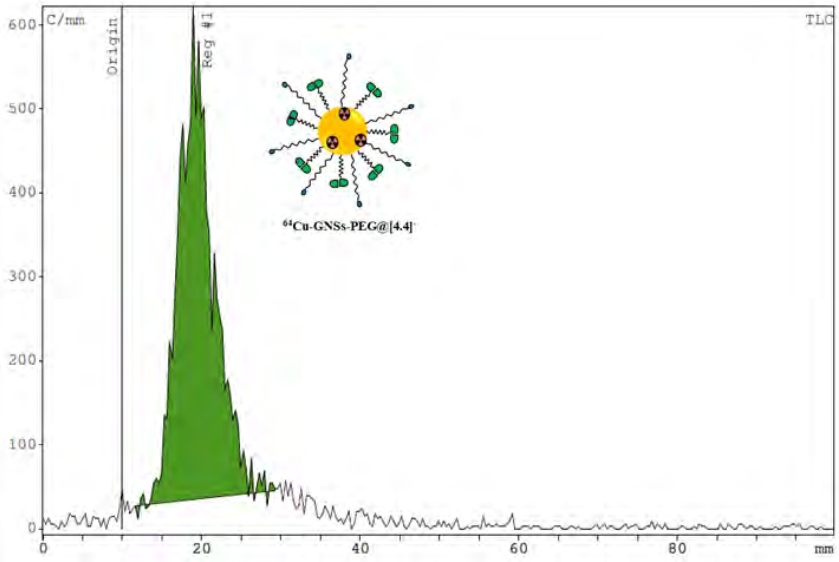

Figure 4.13. Radiochemical purity of ^{64}Cu-GNSs-PEG@[4.4]$^-$ analyzed by radioTLC.

^{64}Cu-radiolabeled GNSm NPs were synthesized following the same protocol used for the preparation of non-radioactive Cu-GNSm-PEG@[4.4]$^-$, although $^{64}CuCl_2$ was added to the reaction mixture. In brief, ^{64}Cu labeled hydrophobic GNSm NPs were prepared by addition of radioactive [^{64}Cu]$CuCl_2$ to the $HAuCl_4$, copper(II) acetylacetonate ([$Cu(acac)_2$]) and 1,2-hexadecanediol solution. To this mixture oleylamine was added. The reaction solution was heated in a microwave to 160°C with a programmed increase of 4°C/min. The reaction was then held at 160°C for 2 h, and was then cooled to room temperature. After centrifugation, the hydrophobic ^{64}Cu-GNSm NPs were obtained and dissolved in hexane to form a homogeneous reddish solution. The synthesized ^{64}Cu-GNSm NPs were further functionalized with PEG and COSAN-SH by following the same procedure as nonradioactive Cu-GNSm-PEG@[4.4]$^-$ (Figure 4.14). The radiochemical yield of ^{64}Cu-GNSm-PEG@[4.4]$^-$ was 18% (non-decay corrected) and radiochemical purity was determined by radioTLC as above 98% (Figure 4.15).

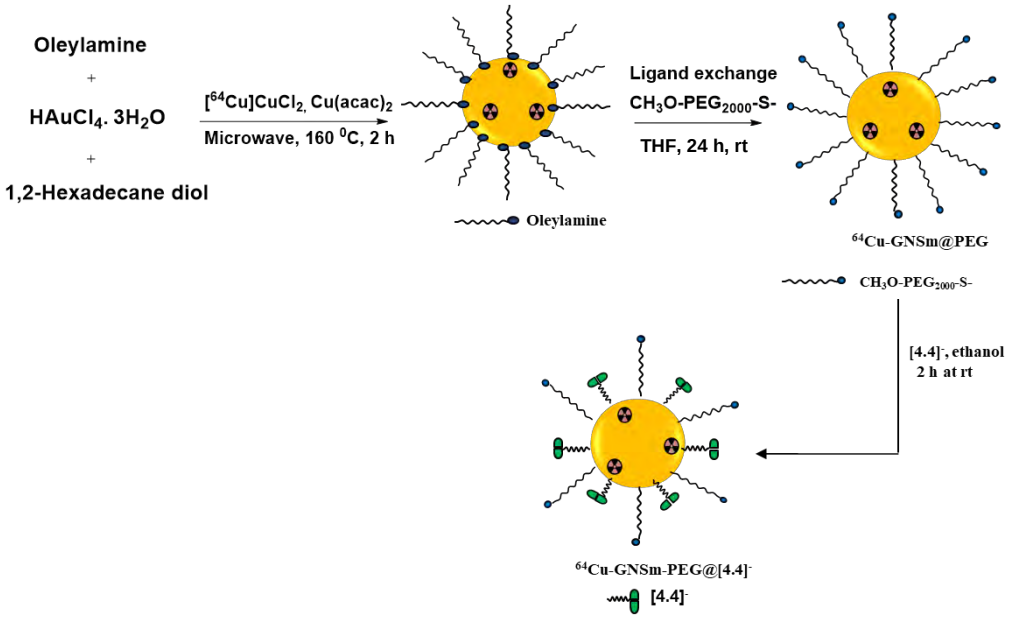

Figure 4.14. Schematic representation of the preparation of ^{64}Cu-GNSm-PEG@[4.4]$^-$

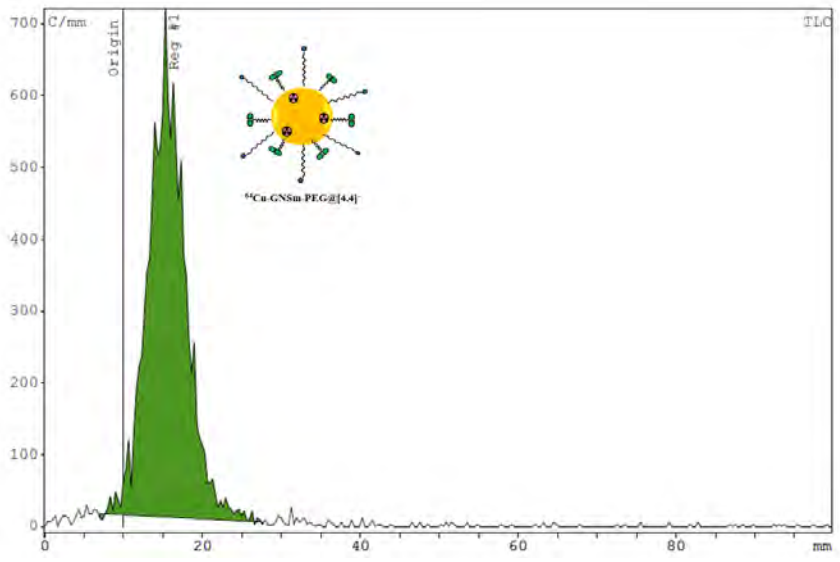

Figure 4.15. Radiochemical purity of ^{64}Cu-GNSm-PEG@[4.4]$^-$ analyzed by radioTLC.

4.3.4. Radiochemical stability

Radiochemical stability of both ^{64}Cu-GNSs-PEG@[4.4]$^-$ and ^{64}Cu-GNSm-PEG@[4.4]$^-$ nanosystems was tested in phosphate buffered saline (PBS), PBS with a challenging agent (ethylenediaminetetraacetic acid; EDTA, 2.5 mM), saline solution (0.9% NaCl), saline solution with EDTA and mouse serum. The stability was checked by incubating the nanoparticles at 37°C

for up to 48 h. Both nanosystems showed excellent stability in all the media without any significant detachment of ^{64}Cu from the gold core (Figure 4.16).

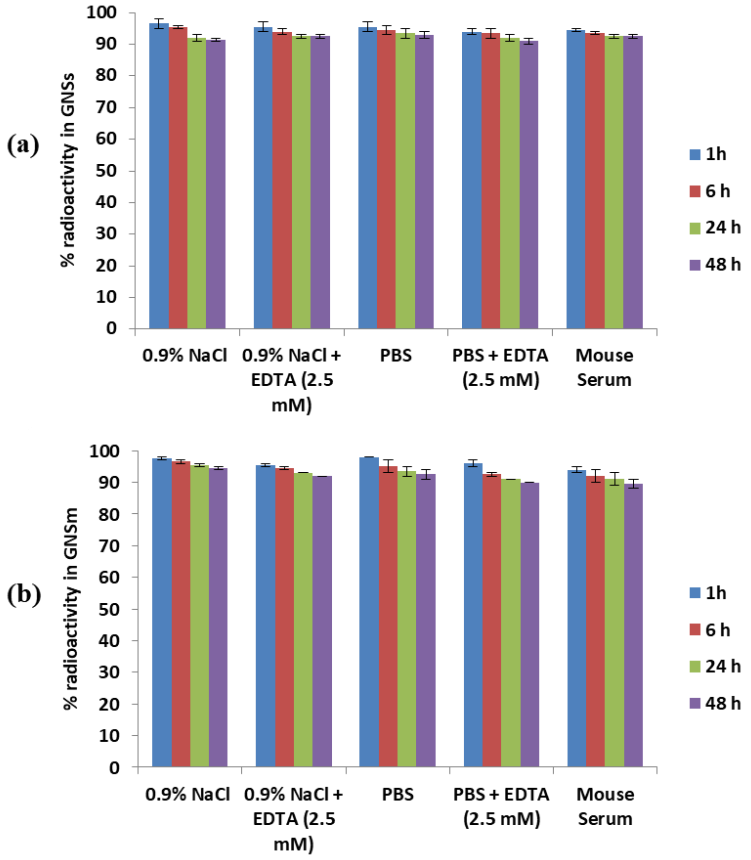

Figure 4.16. Radiochemical stability of ^{64}Cu-GNSs-mPEG@[4.4]$^-$ (a) and ^{64}Cu-GNSm-mPEG@[4.4]$^-$ (b) at different incubation times (1, 6, 24 and 48 h) in physiological saline (0.9% NaCl), physiological saline solution containing EDTA (0.9% NaCl + 2.5 mM EDTA), phosphate buffered saline (PBS), phosphate buffered saline containing EDTA (PBS + 2.5 mM EDTA), and mouse serum.

4.3.5 *In vivo* biodistribution studies

The *in vivo* distribution of the labeled particles, ^{64}Cu-GNSs-PEG@[4.4]$^-$ and ^{64}Cu-GNSm-PEG@[4.4]$^-$, was carried out using PET in combination with Computerized Tomography (CT). To evaluate the capacity of the nanosystems to accumulate in tumor, a human gastrointestinal adenocarcinoma mouse model (generated by subcutaneous inoculation of MKN45 cells) was used. The general biodistribution of both radiolabeled nanosystems and the accumulation in the tumor after intravenous administration were determined by acquiring static PET images at different time points (1, 6, 24 and 48 hours; see Figures 4.17 and 4.20 for representative images).

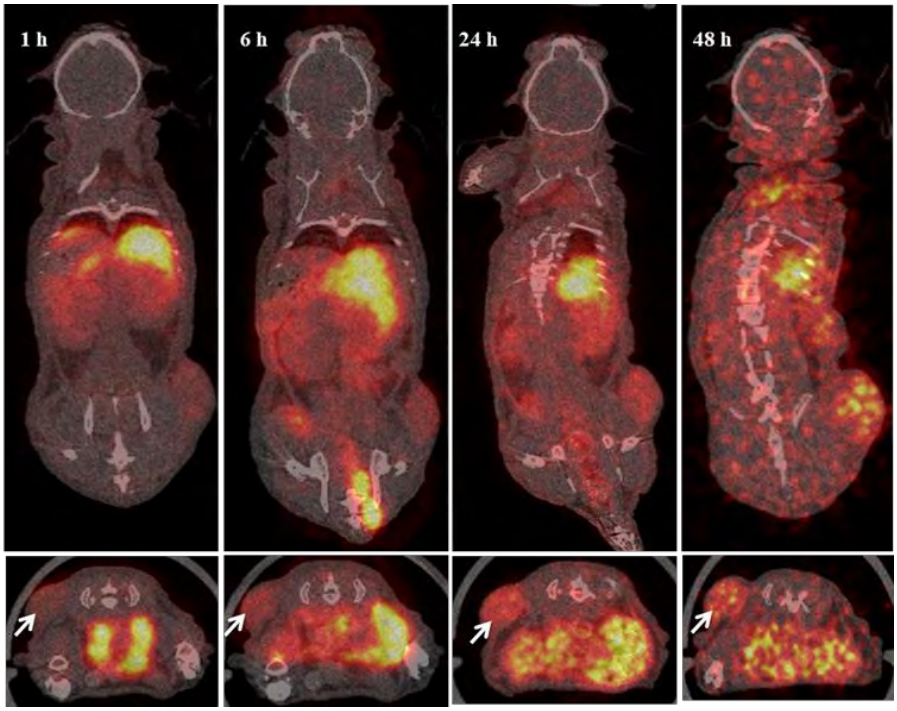

Figure 4.17. Representative PET images (coronal and axial views) obtained at 1, 6, 24, and 48 hours after administration of ^{64}Cu-GNSs-PEG@[4.4]$^-$ in mice bearing MKN-45 tumor. Maximum intensity projection (MIP) PET images were co-registered with representative CT coronal slices. The position of the tumor is indicated with white arrows.

Volumes of interest (VOIs) were drawn in major organs and tumor tissue based on reconstructed CT images, and used to quantify PET images. The amount of radioactivity in each region was determined as percentage of injected dose per cubic centimeter of tissue (%ID/cm^3) (Figure 4.18). In the case of ^{64}Cu-GNSs-PEG@[4.4]$^-$ NPs, at t = 1 hour time point, high amount of radioactivity was observed in the heart (13.29±3.0 %ID/cm^3), indicating the presence of a significant amount of labeled GNSs in the blood pool. This value progressively decayed with time, to reach a value of 2.27±1.0 %ID/cm^3 at t = 48 hours.

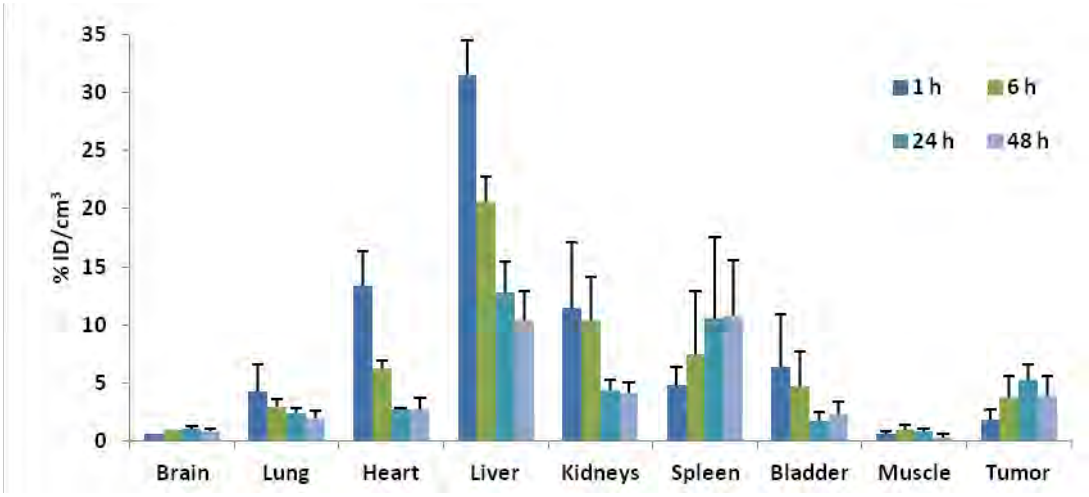

Figure 4.18. Accumulation of ^{64}Cu-GNSs-PEG@[4.4]$^{-}$ in different organs at different time points after intravenous administration, analyzed by PET imaging (values are expressed as mean ± standard error mean, n = 3).

At t = 1 hour, high accumulation of GNSs was observed in liver (31.42±3.0 %ID/cm^3), while accumulation in lungs (4.33±2.3 %ID/cm^3) and spleen (4.82±1.6 %ID/cm^3) was lower. In the liver and lungs, a progressive decrease of radioactivity concentration was observed over time, reaching values of 10.37±2.5 %ID/cm^3 and 1.96±0.7 %ID/cm^3, respectively, at t = 48 hours (Figure 4.18). These results suggest that GNSs NPs were moderately sequestrated by organs of the mononuclear phagocyte system (MPS). Lower accumulation in kidneys (i.e. 4.15±0.9 %ID/cm^3), and no significant elimination via urine were observed. A progressive accumulation of GNSs in spleen was observed over time. Noteworthy, the concentration of radioactivity in the tumor progressively increased with time (Figure 4.19) to reach the maximum value at t = 24 hours (5.3±1.3 %ID/cm^3) and slowly decreased afterwards (3.92±1.7 %ID/cm^3 at t = 48 hours).

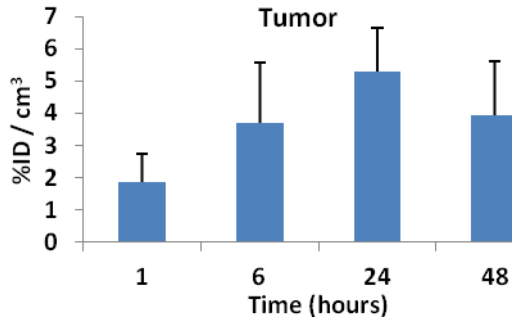

Figure 4.19. Accumulation of ^{64}Cu-GNSs-PEG@[4.4]$^{-}$ in tumor at different time points after administration (1, 6, 24 and 48 h).

In the case of ^{64}Cu-GNSm-PEG@[4.4]$^{-}$ NPs, high accumulation was observed in the liver at all times) and low accumulation was observed in all other major organs (Figures 4.20 and 4.21). The concentration of radioactivity in the tumor increased to 1.3±1.1 %ID/cm^3 at t = 48 hours (Figure 4.22).

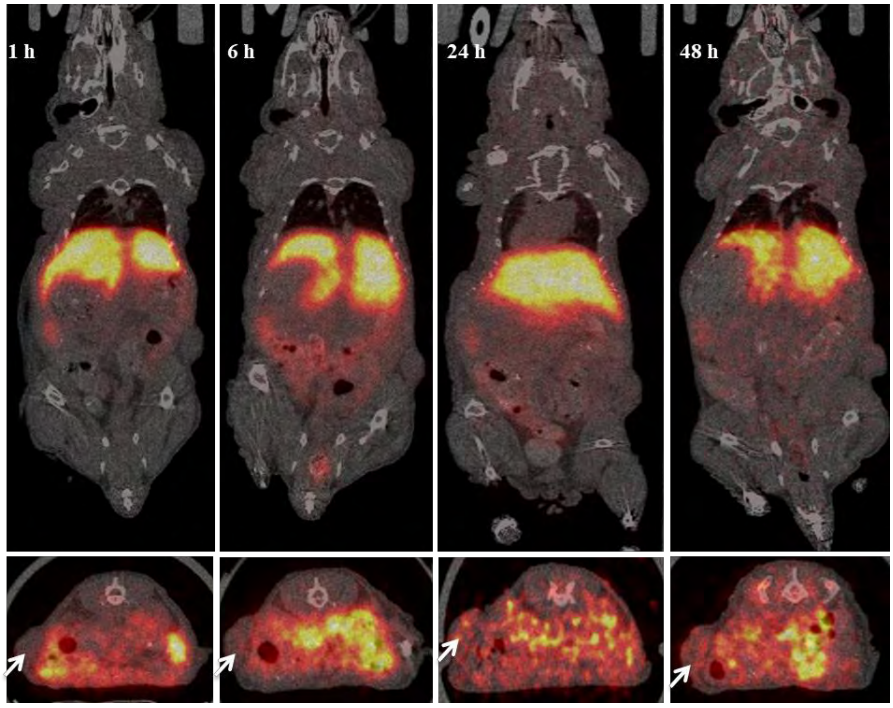

Figure 4.20. Representative PET images (coronal and axial views) obtained at 1, 6, 24, and 48 hours after administration of ^{64}Cu-GNSm-PEG@[4.4]$^{-}$ in mice bearing MKN-45 tumor. Maximum intensity projection (MIP) PET images were co-registered with representative CT coronal slices. The position of the tumor is indicated with white arrows.

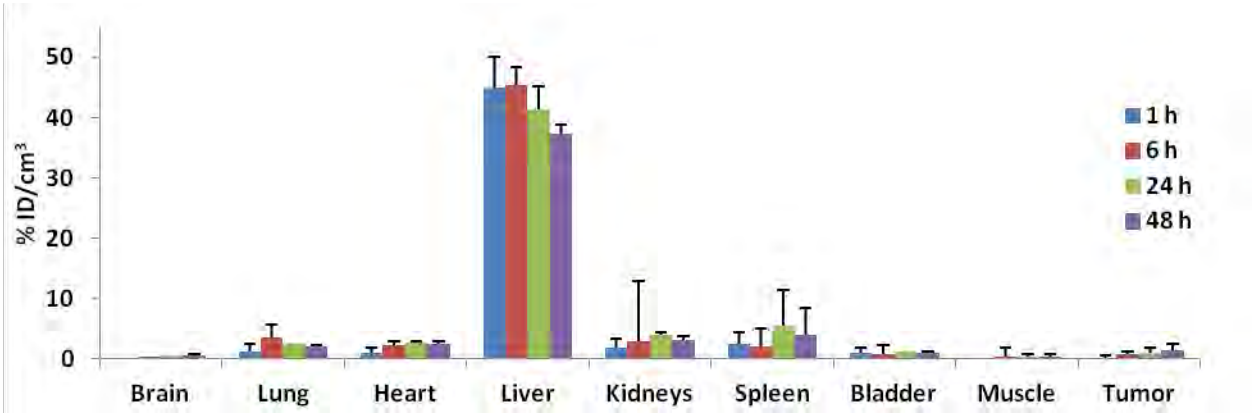

Figure 4.21. Accumulation of ^{64}Cu-GNSm-PEG@[4.4]$^{-}$ in different organs at different time points after intravenous administration, analyzed by PET imaging (values are expressed as mean ± standard error mean, n = 3).

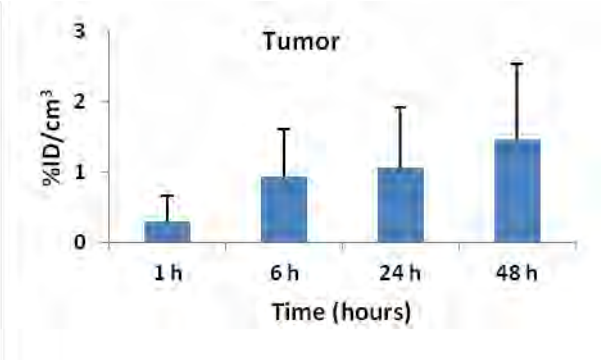

Figure 4.22. Accumulation of ^{64}Cu-GNSm-PEG@[4.4]$^{-}$ in the tumor at different time points (1, 6, 24 and 48 h) after intravenous administration.

4.3.6 *Ex vivo* studies

Ex vivo gamma-counting experiments were conducted for both ^{64}Cu-GNSs-PEG@[4.4]$^{-}$ and ^{64}Cu-GNSm-PEG@[4.4]$^{-}$ nanosystems immediately after finalizing the last imaging session at 48 h time point. Organs of interest were harvested and the amount of radioactivity in each organ was measured in an automated gamma-counter (Wallach Wizard, PerkinElmer, Waltham, MA, USA) (Figure 4.23). The *ex vivo* results of both nanosystems were in good agreement with *in vivo* PET quantification.

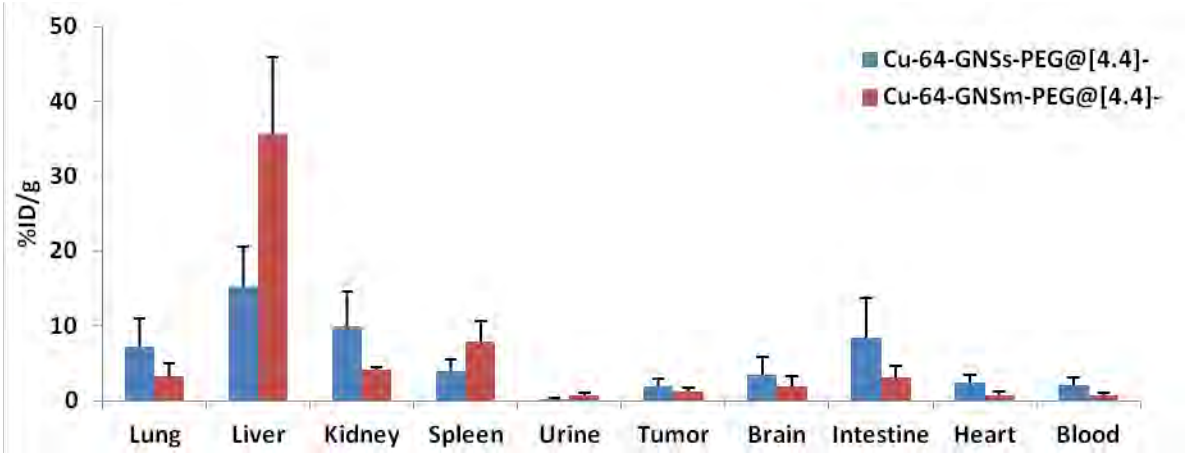

Figure 4.23. Accumulation of ^{64}Cu-GNSs-PEG@[4.4]$^{-}$ and ^{64}Cu-GNSm-PEG@[4.4]$^{-}$ in different organs after *ex vivo* analysis at 48 h time point, analyzed by gamma counter (values are expressed as mean ± standard error mean, n = 3 per NP type).

As mentioned previously, one of the problems to follow the biodistribution of the NPs may arise from eventual detachment of the radiolabel. In order to prove that the distribution data obtained by *in vivo* PET and *ex vivo* gamma counting actually reflect the distribution of the particles, we carried out ICP-MS analysis of selected organs. The boron and gold concentration determined by ICP-MS confirmed the stability of the NPs and correlated well with data obtained from studies conducted with radioactivity measurements, thus confirming the suitability of our approach and the capacity of the nanoparticles to reach the tumor (Figure 4.24).

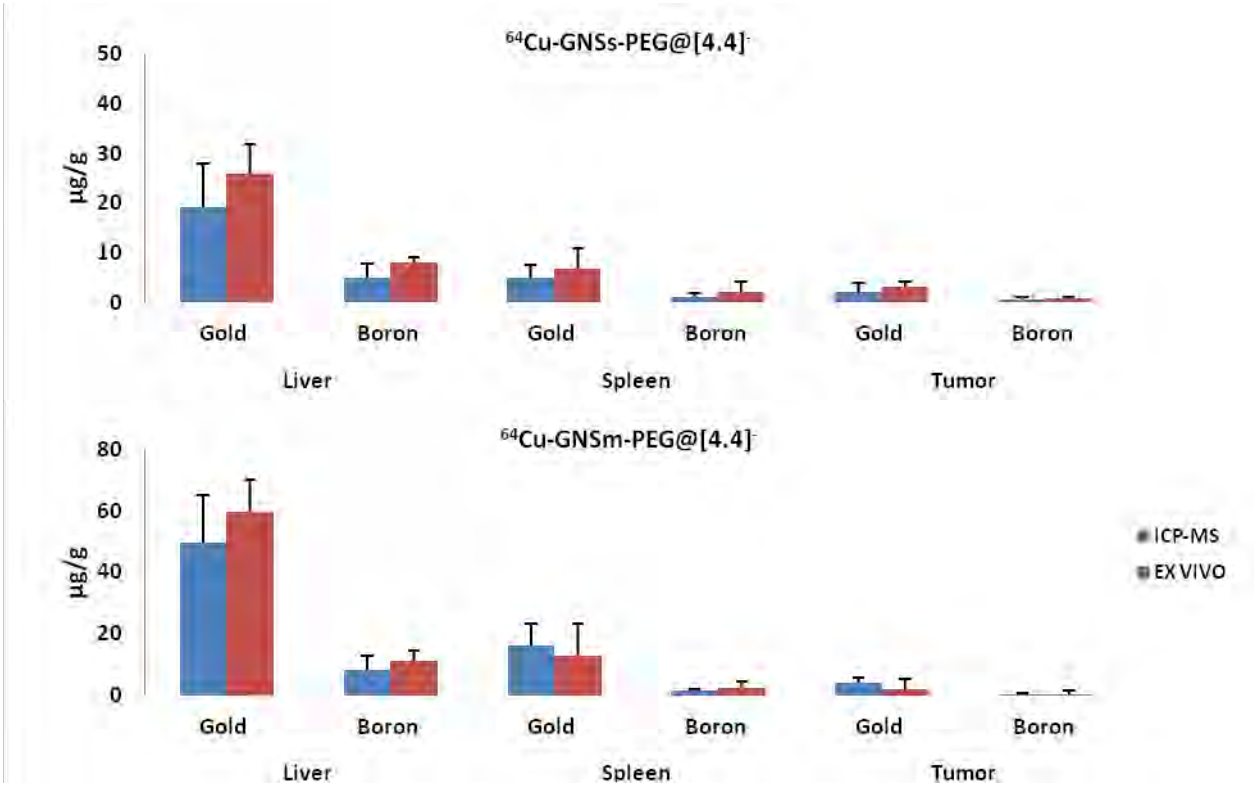

Figure 4.24. Amount of gold and boron in, liver, spleen and the tumor at 48 hours after intravenous administration of ^{64}Cu-GNSs-PEG@[4.4]$^-$ and ^{64}Cu-GNSm-PEG@[4.4]$^-$, as determined by ICP-MS and *ex vivo* gamma counting.

With the results obtained, we made some estimation of the potential therapeutic efficacy of the small gold NPs, which showed enhanced accumulation in the tumor. Considering that: (i) the injected dose to the animal was 200 µg of ^{64}Cu-GNSs-PEG@[4.4]$^-$ (amount of gold); (ii) GNSs contain 210 µg boron per mg of gold; and (iii) the concentration of GNSs in the tumor at t = 24 hours after administration is 5.3±1.3 %ID/cm^3, the average concentration of boron in the tumor at t = 24 hours is 2.22 µg/cm^3. In the case of ^{64}Cu-GNSm-PEG@[4.4]$^-$, the injected dose to the

animal was 180 μg (amount of gold); (ii) GNSm contain 155 μg boron per mg of gold; and (iii) the concentration of GNSs in the tumor at t = 48 hours after administration is 1.3±0.3 %ID/cm^3, the average concentration of boron in the tumor at t = 48 hours is 0.3 μg/cm^3. These values, despite they could be improved by administering a higher dose to the animals, are below the threshold perceived as sufficient to guarantee therapeutic efficacy. Hence, we next tackled the design of nanosystems suitable for dual therapeutic approaches (see chapter 5).

4.4. Conclusions

The synthesis of medium- (ca. 10 nm) and small- (ca. 3 nm) sized gold NPs, containing copper at the core and functionalized with COSAN and thiolated polyethylene glycol can be achieved by using adapted methods. The presence of the copper at the core enables the radiolabeling using the positron emitter ^{64}Cu. The labeled particles showed good stability *in vivo*, low toxicity *in vitro* and fast internalization in MKN45 cells. PET images following the intravenous administration of small gold nanospheres showed significant accumulation in the tumor at 24–48 hours after administration, whereas medium size particles showed moderate tumor uptake and major accumulation in the liver. In both cases, the accumulation of boron in the tumor is insufficient to tackle therapy experiments. These results suggest that nanosystems enabling dual therapeutic approaches may be required.

4.5. Experimental section

4.5.1. Reagents

Cesium cobalt(III) *bis*(dicarbollide) (COSAN) (Katchem Ltd., Prague, Czech Republic), tetrahydropyran (sigma Aldrich), gold(III) chloride trihydrate ($HAuCl_4 \cdot 3H_2O$, Aldrich), copper (II) acetylacetonate ($Cu(acac)_2$), oleylamine, 1,2-hexadecanediol (TCI, Spain), hydrochloric acid (HCl, 37%, TraceSELECT®), nitric acid (HNO_3, 70%, ≥99.999% trace metals basis), sodium borohydride, copper chloride ($CuCl_2.2H_2O$), poly (ethylene glycol) methyl ether thiol (MW 2000, Sigma-Aldrich) and cyanine 3 N-Hydroxysuccinimide ester (Cy3-NHS) from BroadPharm®, were used as purchased. All other reagents and anhydrous solvents, stored over 4 Å molecular sieves, were purchased from Aldrich Chemical Co. (Madrid, Spain) and used without further purification. HPLC grade solvents were purchased from Scharlab (Sentmenat, Barcelona, Spain). $^{64}Cu^{2+}$ dissolved in 0.1M HCl was produced at CIC biomaGUNE Radiochemistry facility by

proton irradiation of ^{64}Ni via the $^{64}Ni(p,n)^{64}Cu$ nuclear reaction using standard protocols [Kume, 2012 #49].

In chemical syntheses, experiments were carried out, except when noted, under a dry, oxygen-free dinitrogen atmosphere. The microwave synthesis of GNSm NPs was performed on a CEM Discover-SP. Column chromatography was performed using silica gel 60 (Scharlab, Spain). Analytical thin layer chromatography (TLC) measurements were conducted with silica gel 60 F_{254} plates (Macherey-Nagel); and the spots were visualized under UV lamp.

4.5.2. Instrumentation:

The ^{1}H-NMR (500 MHz), ^{13}C-NMR (126 MHz) and ^{11}B-NMR (160 MHz) spectra were recorded on a 500-MHz Avance III Bruker spectrometer. All NMR spectra were performed in deuterated solvents at 22 °C. The ^{11}B-NMR shifts were referenced to external $BF_3 \cdot OEt_2$, while the ^{1}H and ^{13}C-NMR shifts were referenced to $SiMe_4$. Chemical shifts are reported in units of parts per million (ppm) downfield from the reference peak and all coupling constants are reported in Hertz (Hz).

UPLC/ESI-MS analyses were performed using an AQUITY UPLC separation module coupled to LCT TOF Premier XE mass spectrometer (Waters, Manchester, UK). An Acquity BEH C18 column (1.7 μm, 5 mm, 2.1 mm) was used as stationary phase. The elution buffers were A (water and 0.1% formic acid) and B (Methanol and 0.1% formic acid). The column was eluted with gradient: t=0 min, 95% A, 5% B; t=0.5 min, 95% A, 5% B; t=5.5 min, 25% A, 75% B; t=16 min, 1% A, 99% B; t=20min, 1% A, 99% B. Total run was 20 min, injection volume was 5 μL and flow rate 300 μL/min. The detection was carried out in both, negative and positive ion mode, monitoring the most abundant isotope peaks from the mass spectra ($M-H^+$) or ($M+H^+$).

Ultraviolet-Visible-Near infrared (UV-Vis-NIR) spectra were measured in an Agilent 8453 UV-Vis-NIR diode-array spectrophotometer.

ξ-potential measurements were performed at neutral pH using a Malvern Zetasizer Nano ZS system (Malvern Instruments, Malvern, UK).

Transmission electron microscopy (TEM) was performed using a JEOL JEM-1400 plus microscope (Jeol, Tokyo, Japan) working at 120 kV. The carbon film of copper grids (CF400-Cu) was treated under air plasma in a glow discharge system (Emitech K100X, 40mA during 2

min) just before sample preparation. For TEM examinations, a single drop (1 μL) of the NPs solution was placed onto a copper grid coated with a carbon film (Electron Microscopy Sciences).

X-ray photoelectron spectroscopy (XPS) experiments were performed in a SPECS Sage HR 100 spectrometer with a non-monochromatic X ray source (Aluminium Kα line of 1486.6 eV energy and 252 W), placed perpendicular to the analyser axis and calibrated using the 3d5/2 line of Ag with a full width at half maximum (FWHM) of 1.1 eV. The selected resolution for the spectra was 15 eV of Pass Energy and 0.15 eV/step. All measurements were made in an ultra-high vacuum (UHV) chamber at a pressure around 6×10^{-8} mbar. An electron flood gun was used for charge neutralisation. Gaussian Lorentzian functions were used for fittings (after a Shirley background correction) where the FWHM of all the peaks were constrained while the peak positions and areas were set free. Main C1s peak was used for charge reference and set at 284.8 eV.

Gamma counting experiments were carried out using a Wallach Wizard, PerkinElmer (Waltham, MA, USA) gamma counter.

ICP-MS measurements were performed on a Thermo iCAP Q ICP-MS (Thermo Fisher Scientific GmbH, Bremen, Germany). An ASX-560 autosampler was coupled to the ICP-MS (CETAC Tech, Omaha, NE, USA).

Cell observer microscopy experiments were carried out using a Zeiss Axio Observer Fluorescence microscope using Ibidi clear bottomed μ-slide 8-well microscopy plates and analyzed by ZEN2012-ZEISS.

Confocal cell microscopy experiments were carried out using a Zeiss 880 Confocal Fluorescence microscope using Ibidi clear bottomed μ-slide 8-well microscopy plates and analyzed by ZEN2012-ZEISS.

Radio-thin layer chromatography (radio-TLC) was performed using iTLC-SG chromatography paper (Agilent Technologies, CA, USA) and 20 mM citric acid + 60 mM EDTA/acetonitrile solution (9/1 v/v) as the stationary and mobile phases, respectively. TLC plates were analyzed using a TLC-reader (MiniGITA, Raytest).

4.5.3 Chemistry and radiochemistry

Synthesis of non-radioactive Cu-GNSs@PEG

In a typical reaction, water (1.0 mL), $HAuCl_4$ (10 mM, 94 µL), and $CuCl_2.2H_2O$ (10 mM, 94 µL) were mixed in a glass vial, followed by the dropwise addition of mPEG-thiol (MW = 2000 Da, 7 mM, 200 µL). To this mixture was added sodium borohydride (20 mM, 200 µL) under quick stirring for 2 min at room temperature and then kept for 2 hours. The Cu-GNSs-PEG NPs were purified using a centrifuge filter (Amicon, 10 kDa MWCO) and washed with MilliQ water (MQ) three times to remove unbound mPEG.

Synthesis of Cu-GNSs-PEG@[4.4]$^-$

To the obtained Cu-GNSs-PEG NPs (210 µg of gold) was added COSAN-SH (**[4.4]**$^-$) (10 mM, 200 µL) under quick stirring at room temperature and then continued for 2 hours. The Cu-GNSs-PEG@[4.4]$^-$ were purified using a centrifuge filter (Amicon, 10 kDa MWCO) and washed with MilliQ water three times to remove unbound **[4.4]**$^-$.

Synthesis of ^{64}Cu-GNSs-PEG@[4.4]$^-$

Synthesis of ^{64}Cu-GNSs-PEG@[4.4]$^-$ was carried out following the same procedure as that used for preparing non-radioactive Cu-GNSs-PEG@[4.4]$^-$. Instead of adding $CuCl_2.2H_2O$ in the first step, radioactive $^{64}CuCl_2$ (222 MBq) was added. The synthesized ^{64}Cu-GNSs-PEG NPs were treated with ethylenediaminetetraacetic acid (EDTA, 10 mM in neutral 50 mM phosphate buffer, 5 µL) and then purified using a centrifuge filter (Amicon, 10 K). The radiochemical purity was determined by instant radio-thin layer chromatography (RadioTLC). In the second step COSAN-SH was attached as described above.

Synthesis of non-radioactive Cu-GNSm NPs

Cu-GNSm NPs nanoparticles were synthesized by reducing $Cu(acac)_2$ and $HAuCl_4$ in oleylamine. Typically, $HAuCl_4.3H_2O$ (0.08 mmol, 0.0256 g), $Cu(acac)_2$ (0.026 mmol, 0.007 g) and 1,2-hexadecanediol (0.4 mmol, 0.010 g) were mixed and dissolved in oleylamine (2 mL) under N_2 atmosphere. Then the resulting solution was heated to 160°C in microwave (CEM Discover-SP) at the heating rate of 4°C/min. After the reaction temperature was kept at 160°C for 2 hours, the solution was cooled to room temperature. The solution was centrifuged and washed

twice with ethanol (2 mL) to remove impurities. The Cu-GNSm NPs nanoparticles were dispersed in hexane.

Synthesis of non-radioactive Cu-GNSm-PEG NPs

The mPEG-thiol (MW = 2000 Da, 7 mM) was dissolved in THF (0.5 mL), added to the Cu-GNSm NPs and stirred for 24 h at room temperature. The mixture was then centrifuged at 10.000 rpm for 8 min to obtain PEGylated GNSm NPs. The Cu-GNSm-PEG was dissolved in MilliQ water (3 mL) and centrifuged at 10.000 rpm for 10 min with centrifuge filter (Amicon, 30K, 3 mL). The procedure was repeated three times to remove unbound mPEG.

Synthesis of Cu-GNSm-PEG@[4.4]$^-$

The COSAN-SH (**[4.4]**$^-$) (0.5 mg) in EtOH (100 µL) was added to the Cu-GNSm-PEG nanoparticles purified by MilliQ water washing (0.3 mg/mL). Afterwards, the solution was stirred at room temperature for 2 h. The mixture was then centrifuged at 10.000 rpm for 8 min using centrifuge filter (Amicon, 30K, 4 mL). The procedure was repeated three times to remove unbound [4.4]$^-$.

Synthesis of ^{64}Cu-GNSm-PEG@[4.4]$^-$

The synthesis of ^{64}Cu-GNSs-PEG@[4.4]$^-$ was carried out following the same procedure as the preparation of non-radioactive Cu-GNSs-PEG@[4.4]$^-$ nanoparticles except for the extra addition of $^{64}CuCl_2$ (370 MBq, 10µL) to the mixture. Then the solution was heated in microwave to 160°C using a heating ramp of 4°C/min. After 2 hours, the solution was cooled to room temperature. The synthesized ^{64}Cu-GNSs-PEG@[4.4]$^-$ was purified and functionalized with mPEG-SH and [4.4]$^-$ by following the same procedure as nonradioactive Cu-GNSs-PEG@[4.4]$^-$.

Synthesis of fluorophore labeled GNSs and GNSm

The synthesis was performed as described previously, but a mixture of 10 % PEG-amine and 90 % PEG-methoxy was used to enable subsequent attachment of the fluorophore Cyanine3-NHS. To attach the fluorophore, 200 µL of functionalized AuNP (1 mg/mL for GNSs or GNSm medium in MQ water) were adjusted to pH 8.6-8.9 and 5 µL Cy3-NHS (1 mg/mL in DMSO) were added. After 1 h incubation at room temperature, the resulting NPs were centrifuged at

8.000×g for 20 min and resuspended in MilliQ water. The labeling was confirmed by UV-VIS spectrophotometry.

4.5.4. *In vitro* studies

Cytotoxicity studies

To determine cell viability, MKN45 human cancer cells, 3T3 healthy mouse cells and human dermal healthy fibroblasts (HDFa) cells were incubated with the multifunctionalized GNSs and GNSm over 24, 48 and 72 hours. Cells were seeded (3×10^4 cells/well, 100 µL/well, 96-well plate), allowed to adhere overnight in complete media (10% Fetal Bovine Serum (FBS) and 1% Penicillin/Streptomycin in RPMI 1640 medium for MKN45 cells, DMEM medium for HDFa cells and 3T3 healthy cells) and maintained in a humid atmosphere at 37°C and 5% CO_2. Then, media was removed and cells were left untreated (blank) or incubated with the GNSs and GNSm-containing formulations, diluted accordingly in media. The experiments were performed in triplicates. After the desired time, cell supernatant was removed and 100 µL/well of MTT reagent (Roche), diluted in the corresponding media to the final concentration of 0.25 mg/mL, was added. After 1 hour incubation at 37°C and 5% CO_2, the excess reagent was removed and formazan crystals were solubilized by adding 200 µL of DMSO per well. The optical density of each well was measured in a TECAN Genios Pro 96/384 microplate reader at 550 nm. Data was represented as the percentage of cell survival compared to control wells.

Cell internalization studies

MKN45 cells were seeded in an 'Ibidi' µ-slide 8-well-plate (20.000 cells/well in 0.3 mL) and incubated overnight to adhere (37 °C, 5% CO_2, humid atmosphere). The media was removed and 0.1 mL Hoechst 33342 (1 µg/mL in media) added to stain the nucleus. After 10 min incubation (37 °C, 5% CO_2, humid atmosphere) 0.1 mL LysoTracker deep red (1 µg/mL in media) was added to stain the lysosomes. After 20 min incubation (37 °C, 5% CO_2, humid atmosphere) media was removed and 0.3 mL of Cy3-labeled GNSs or GNSm (20 µg/mL in medium) were added. After 2 h incubation (37 °C, 5% CO_2, humid atmosphere) the media was removed and replaced with fresh media. The images were taken with a Cell Axio Observer Fluorescence Microscope. Controls of single staining for each fluorophore were included. Images were analyzed by ZEN-ZEISS software.

4.5.5. *In vivo* experiments

Animals

The animals were maintained and handled in accordance with the Guidelines for Accommodation and Care of Animals (European Convention for Protection of Vertebrate Animals Used for Experimental and Other Scientific Purposes) and internal guidelines. Experimental procedures were approved by the ethical committee and local authorities. All animals were housed in ventilate cages and fed on standard diet *ad libitum*.

MKN45 mouse tumor model development

In order to study the biodistribution of the GNSs and GNSm in tumor-bearing mice, Rj:NMRI-*Foxn1*$^{nu/nu}$ female mice (7-8 weeks old, Janvier) were subcutaneously inoculated with 2×10^6 MKN45 tumor cells in the right back. Prior to each inoculation, cells were diluted in sterile PBS: Matrigel (1:1) and Mycoplasma test (Lonza) was carried out to ensure that cells were not contaminated. Tumors were measured every 2–3 days with a digital caliper and volumes were calculated as V (mm^3) = [(short diameter)^2 x (long diameter)]/2. Biodistribution studies were carried out when tumor volume was approximately 200–300 mm^3 (~15 days after tumor inoculation).

Biodistribution studies

PET studies with ^{64}Cu-labeled multifunctionalized GNSs and GNSm were carried out in MKN45 tumor-bearing mice (n=3 per NP type) using an eXplore Vista-CT small animal PET-CT system (GER healthcare). Anesthesia was induced with 3% isoflurane and maintained by 1.5 to 2% of isoflurane in 100% O_2. For intravenous administration of the radiotracer, the tail vein was catheterized with a 24-gauge catheter and the labeled NPs (ca. 3–10 MBq) were injected. PET images were analyzed using PMOD image analysis software (PMOD Technologies Ltd, Zürich, Switzerland). Volumes of interest (VOIs) were manually drawn in lungs, liver, heart, kidneys, spleen, brain, stomach, tumor and bladder using CT images as anatomical reference. VOIs were then transferred to the PET images and time activity curves (decay corrected) were obtained for each organ as cps/cm^3. Curves were transformed into real activity (Bq/cm^3) curves. Injected dose normalization was finally applied to data to get time activity curves as percentage of injected dose per cm^3 of tissue (%ID/cm^3).

In vivo imaging studies using PET in combination with Computerized Tomography (CT) were carried out in a human gastrointestinal adenocarcinoma mouse model (MKN45 human cell line) with Cu-GNSs-PEG@[4.4]$^-$ and Cu-GNSm-PEG@[4.4]$^-$. Static images were acquired (total acquisition time of 30 min) after 1h administration of Cu-GNSs-PEG@[4.4]$^-$ and Cu-GNSm-PEG@[4.4]$^-$ and further static acquisitions were recorded at t = 6 h, 24 h and 48 h post-administration.

4.5.6. *Ex vivo* studies

Mice submitted to imaging sessions were sacrificed at 48 hours post injection, after the last imaging session. Organs of interest were collected and weighed, and the radioactivity was measured in a well gamma-counter (Wallach Wizard, PerkinElmer, Waltham, MA, USA). The uptake of ^{64}Cu in the different organs was calculated as a percentage of the injected dose per gram of tissue (%ID/g) according to the prepared standards. The weighed organs (liver, spleen and tumor) were then immersed in digest solution (HNO_3/HCl = 1:1) with a volume of 5 mL. The dispersions were heated to boiling until organs were completely dissolved. 1 mL of H_2O_2 was then added into the solution, and heating continued until the solution became clear and transparent. The solution was then cooled to room temperature, diluted by 2% HNO_3 to 15 mL, and subsequently analyzed by ICP-MS to determine the concentration of Au and B in each sample.

4.6. References

1. Aminabad NS, Farshbaf M, Akbarzadeh A. Recent Advances of Gold Nanoparticles in Biomedical Applications: State of the Art. *Cell Biochemistry and Biophysics*. **2019**;77(2):123-37.

2. Jeong HH, Choi E, Ellis E, Lee TC. Recent advances in gold nanoparticles for biomedical applications: From hybrid structures to multi-functionality. *Journal of Materials Chemistry B*. **2019**;7(22):3480-96.

3. Terentyuk GS, Maslyakova GN, Suleymanova LV, Khlebtsov BN, Kogan BY, Akchurin GG, Shantrocha AV, Maksimova IL, Khlebtsov NG, Tuchin VV. Circulation and distribution of gold nanoparticles and induced alterations of tissue morphology at intravenous particle delivery. *Journal of Biophotonics*. **2009**;2(5):292-302.

4. Sun X, Huang X, Yan X, Wang Y, Guo J, Jacobson O, Liu D, Szajek LP, Zhu W, Niu G, Kiesewetter DO, Sun S, Chen X. Chelator-free ^{64}Cu-integrated gold nanomaterials for positron emission tomography imaging guided photothermal cancer therapy. *ACS Nano*. **2014**;8(8):8438-46.

5. Zhao Y, Sultan D, Detering L, Luehmann H, Liu Y. Facile synthesis, pharmacokinetic and systemic clearance evaluation, and positron emission tomography cancer imaging of ^{64}Cu-Au alloy nanoclusters. *Nanoscale*. **2014**;6(22):13501-9.

6. Zhao Y, Sultan D, Detering L, Cho S, Sun G, Pierce R, Wooley KL, Liu Y. Copper-64-alloyed gold nanoparticles for cancer imaging: Improved radiolabel stability and diagnostic accuracy. *Angewandte Chemie - International Edition*. **2014**;53(1):156-9.

7. NIST X-ray Photoelectron Spectroscopy Database [database on the Internet]. Measurement Services Division of the National Institute of Standards and Technology (NIST). 2012 [cited 08/07/2019].

Chapter 5: Gold Nanorods as boron carriers for BNCT

5.1. Introduction

In the last two chapters, the application of spherical gold NPs as boron-carriers with potential application in Boron Neutron Capture Therapy (BNCT) has been explored. The results obtained suggest that the amount of boron accumulated in the tumor models investigated is insufficient to tackle *in vivo* therapeutic experiments. In view of the results, we decided to explore nanosystems enabling the combination of two therapeutic approaches, and the natural selection is gold nanorods (GNRs). Indeed, the shape of nanoparticles has been recognized as a key factor influencing biodistribution, blood circulation time and cellular uptake in cancer drug delivery [1, 2]. This is also the case for gold nanosystems [3], and hence in our case the use of nanosystems with other shapes may increase circulation time and eventually enhance tumor accumulation. Besides this, GNRs exhibit strong surface plasmon band in the visible (~520 nm) and near infrared (~900 nm) regions corresponding to the transverse and longitudinal surface plasmon oscillations of free electrons, respectively. The interaction of incident infrared light with the GNRs produces ultimately localized heating, which can be used to trigger thermal damage locally. Because infrared light can penetrate deeply into tissues, photothermal therapy using GNRs as the sensitizing agent has been investigated in the recent years, both to induce local heating and to trigger drug release upon interaction with incident light [4-6].

In this chapter, as a third approach for the development of gold NP-based BNCT agents, we selected rod-shaped gold particles functionalized with PEG-thiol (to improve GNRs stability and prolong circulation time during *in vivo* biodistribution studies). As the boron source, we decided to incorporate the boron cluster **[4.4]**$^-$ (see chapter 3) on the GNRs surface *via* Au-S interaction. The resulting multifunctionalized GNRs were radiolabeled with ^{64}Cu, a positron emitter with a half-life of 12.7 hours, to enable *in vivo* imaging using Positron Emission Tomography (PET). The radiolabel was incorporated on the surface of the GNR core *via* chemical reduction of $^{64}CuCl_2$ under mild reaction conditions. The presence of gold nanorods and boron atoms in the tumor tissue, as demonstrated in our *in vivo* experiments, should enable the application of simultaneous BNCT and photothermal therapy, with the consequent improved therapeutic efficacy.

5.2 Objectives

The specific objectives of this chapter are:

5- To synthesize and characterize stable and biocompatible GNRs functionalized with PEG and COSAN.

6- To perform radiolabeling studies for the incorporation of positron emitters in the core of the multifunctionalized GNRs.

7- To perform *in vitro* studies (cytotoxicity and cell internalization studies) of multifunctionalized GNRs in different cell lines; namely, MKN45 gastric cell line and human dermal fibroblasts (HDFa) cell line.

8- To evaluate pharmacokinetic properties of the novel multifunctionalized GNRs using positron emission tomography (PET) in a human gastrointestinal adenocarcinoma mouse model (MKN45 human cell line) after intravenous administration.

5.3 Results and Discussion

5.3.1 Synthesis and Characterization of GNR-mPEG@[4.4]$^-$

The approach that we followed for the preparation of boron-rich GNRs was similar to that used in previous chapters, this is, we used the same stabilising agent and the same boron cluster, [3,3'-Co(1,2-$C_2B_9H_{10}$)(8'-O-$(CH_2)_5$-SH-1',2'-$C_2B_9H_{11}$)]$^-$ (**[4.4]**$^-$), which was synthesized following the method described in Chapter 3.

In parallel, cetyltrimethylammonium bromide (CTAB)-stabilised GNRs (GNR-CTAB) were prepared following the seedless method [7]. The conditions were adjusted in order to achieve monodisperse GNRs with average dimensions (length × width) of 37 × 10 nm, in a one-pot reaction. In brief, $HAuCl_4$ was added to CTAB solution and shaken for 1 min. To this solution, silver nitrate was added and shaken gently for 1 min. Hydrochloric acid was introduced to obtain a pH close to 2.0. After that, ascorbic acid was added under gentle stirring until the solution became clear. In the final step, ice-cold sodium borohydride was injected into the growth solution and allowed to react for 6 h. The growth solution was maintained at 27-30 °C in a water bath (Figure 5.1). The synthesized GNR-CTAB were centrifuged twice at 14500 rpm to remove the excess CTAB as well as other reagents, and re-dispersed in water.

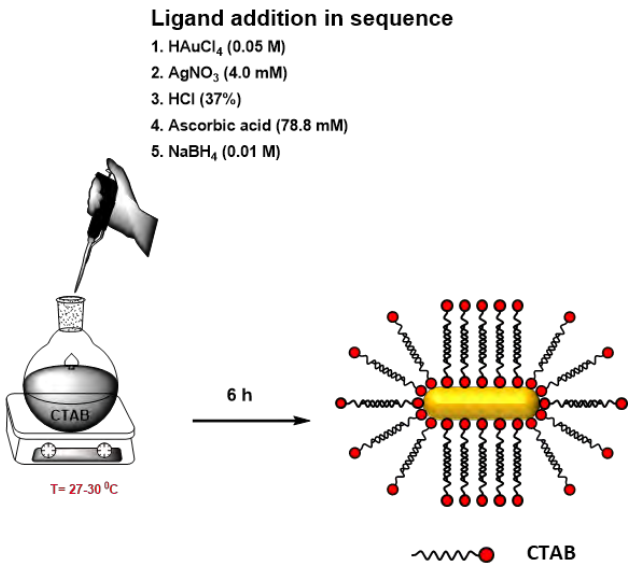

Figure 5.1. Schematic representation of the preparation of GNR-CTAB.

The obtained GNR-CTAB were analysed by UV-Vis-NIR spectrophotometry, transmission electron microscopy (TEM) and dynamic light scattering (DLS). UV-Vis-NIR showed the longitudinal surface plasmon resonance (SPR) band centred at 811 nm (Figure 5.2a). TEM images showed uniform gold nanorods with sizes 37±3 × 10±1 nm (length × width; aspect ratio of 3.7) (Figure 5.2b). Zeta-potential values of +35±1 mV were obtained, as expected due to the positively charged CTAB surfactant bilayer [8] (Figure 5c).

The biological application of GNRs requires the removal of CTAB surfactant bilayer due to its high toxicity and the poor colloidal stability in biological media [9]. Therefore, to increase the *in vivo* stability, biocompatibility and blood circulation half-life of GNRs, several GNRs surface modifications by ligand exchange with different polymers have been proposed [10-12]. Among the many different polymers and ligands, poly(ethylene glycol)thiol (PEG-SH) is one of the most commonly used in the modification of gold nanostructures. PEG polymers provide high degree of stability, low toxicity and high biocompatibility for GNRs and several PEGylated products have been approved by the FDA (Food and Drug Administration) for clinical use.

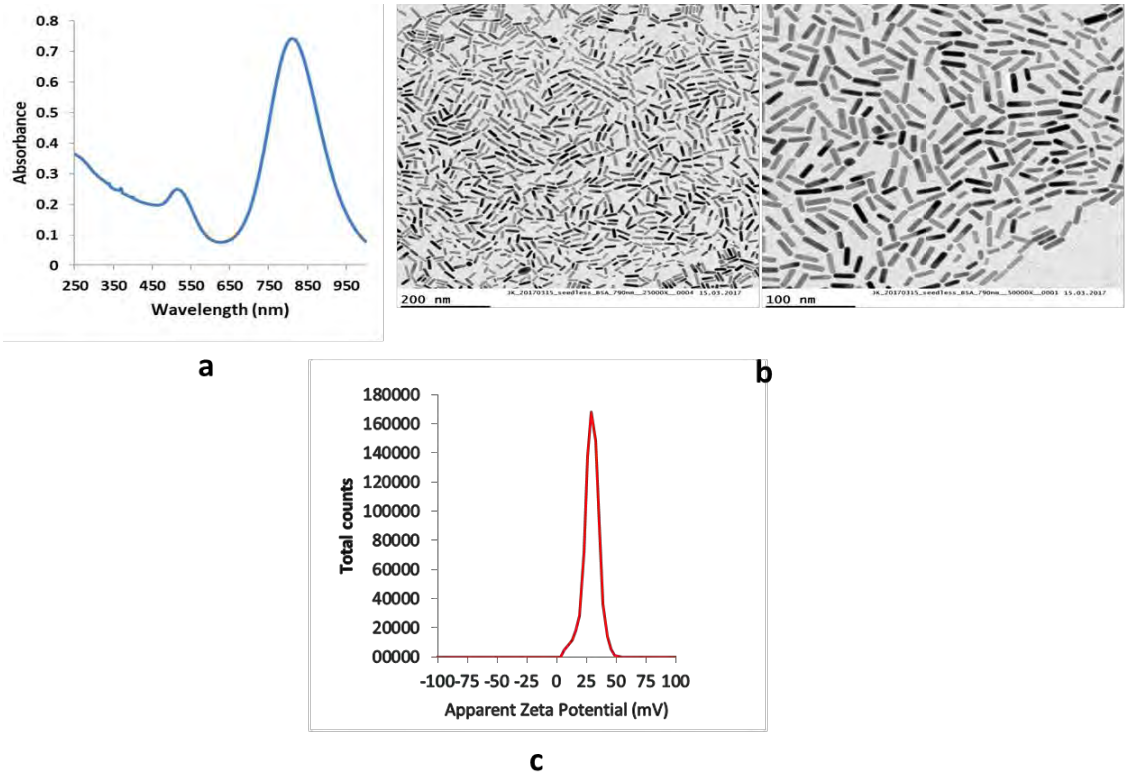

Figure 5.1. UV-Vis-NIR absorption spectra (a); TEM (b) and Zeta potential (c) of GNR-CTAB.

CTAB-protected GNRs were functionalized with PEG by reacting with methoxyPEG$_{5k}$–SH for 20–24 h in pure water based on previously reported protocols [11, 13]. In this work, mPEG-stabilized GNRs (GNR-mPEG) were prepared by mixing GNR-CTAB solution with 5 kDa mPEG (PEG:Au molar ratio of 1.5) for 24 hours at room temperature in water (Figure 5.3).

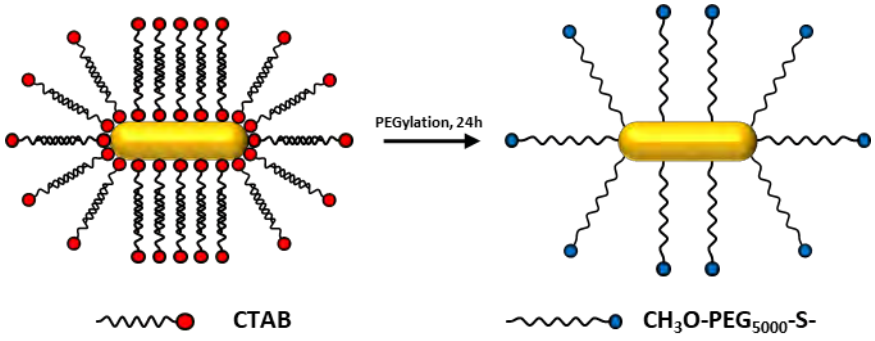

Figure 5.3. Schematic representation of the preparation of GNR-mPEG.

The functionalization of GNRs with mPEG–SH was much more complex than that of the citrate-AuNPs because of a strong capping surfactant (CTAB) on the nanorods. In the case of spherical gold nanoparticles the citrate monolayer can be very easily replaced by the thiol group (reaction time 2 h); however, the double-layered CTAB on GNRs hinders the binding of PEG–SH to the GNR surface, leading to a slow loading speed of PEG–SH. After 24 h reaction, the synthesized GNR-mPEG were centrifuged twice at 14500 rpm to remove the excess PEG, and re-dispersed in water. The minimal bathochromic shift in the longitudinal SPR band from 800 to 819 nm (Figure 5.4a) after replacement of CTAB by mPEG confirms the retention of structural and optical properties of the GNRs after modification. Replacement of positively charged CTAB with neutral PEG chains resulted in zeta potential values close to neutral (8±2 mV; Figure 5.4b). TEM images revealed the similar size and aspect ratio of GNRs before and after PEGylation (Figure 5.4c).

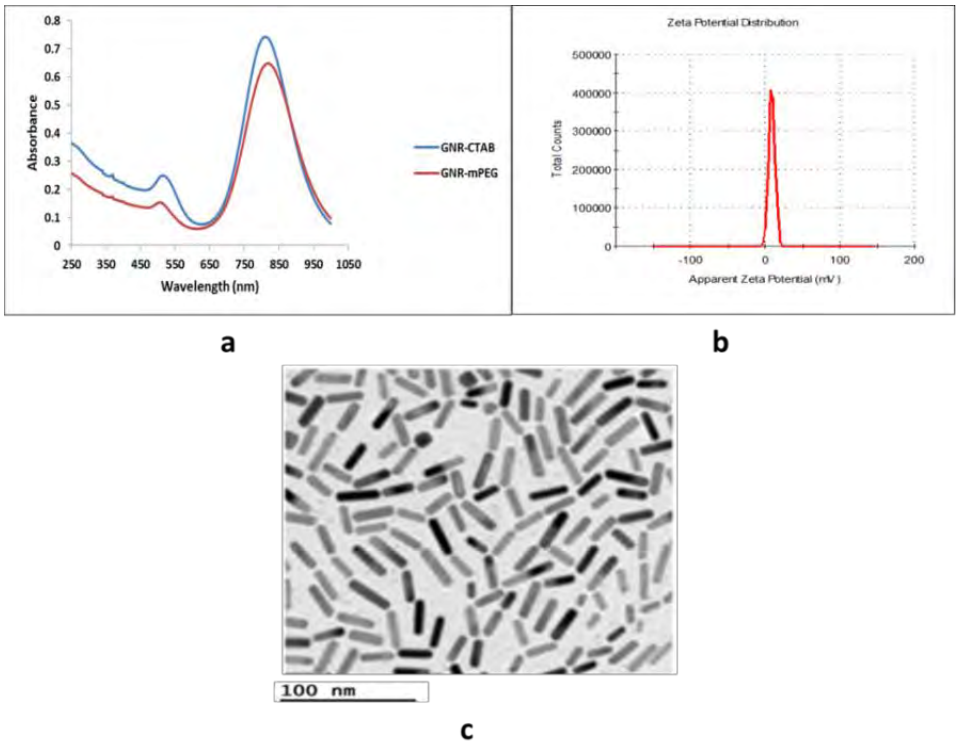

Figure 5.4. UV-vis-NIR of GNR-CTAB and GNR-mPEG (a); Zeta potential (b) and TEM images (c) of GNR-mPEG.

After successful functionalization of GNRs with mPEG-thiol, we next tackled the attachment of thiolated COSAN derivative (**[4.4]**$^-$) on the GNR-mPEG surface. This was carried out by

incubation of GNR-mPEG solution and compound **[4.4]**$^-$ in ethanol under stirring for 2 h at room temperature (Figure 5.5).

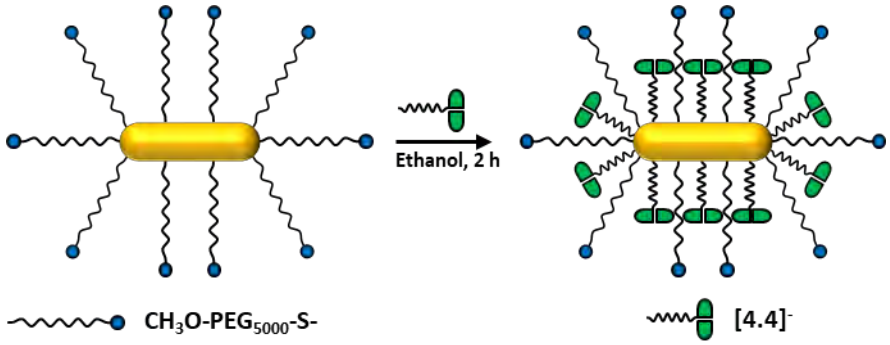

Figure 5.5. Preparation of GNR-mPEG@[4.4]$^-$ from GNR-mPEG.

In order to evaluate the loading capacity of the boronated ligand into the GNRs, these were incubated with different amounts of **[4.4]**$^-$ (GNR/[4.4]$^-$ molar ratios: 12, 10, 8, 6, 4, 2, 1.5 and 1.0). Upon surface modification of GNR-mPEG with different concentrations of **[4.4]**$^-$, no tailing or broadening was observed in the normalised UV-vis spectra, indicating excellent stability of the synthesized GNRs (Figure 5.6). However, broadening of the longitudinal peak and increase in the intensity of the transversal absorption band indicate the instability of the functionalized GNRs for GNR/**[4.4]**$^-$ molar ratio 1.0 (blue line, Figure 5.6). Therefore, the GNR/**[4.4]**$^-$ molar ratio 1.5 was considered as optimal ratio to load the boron rich compound on GNR surface, as under these conditions we expected to obtain maximum concentration of boron on the NPs without affecting the stability and aggregation status of the nanorods.

After purification by centrifugation and repeated washing, boron-rich GNRs (GNR-mPEG@[4.4]$^-$) were obtained. The size and aspect ratio remained the same as for GNR-mPEG (Figure 5.7a). While UV-Vis-NIR spectroscopy showed unchanged absorption maximum at 819 nm (Figure 5.7b), a new absorption band appeared at 320 nm, related to the absorption by COSAN (314 nm), suggesting successful adsorption of the boron cluster on the surface of GNRs. The recorded shift of the zeta potential value, from 8±2 mV to -12±2 mV (Figure 5.7c), confirms the attachment of negatively charged cobalt-*bis*-dicarbollide complexes on the GNR surface.

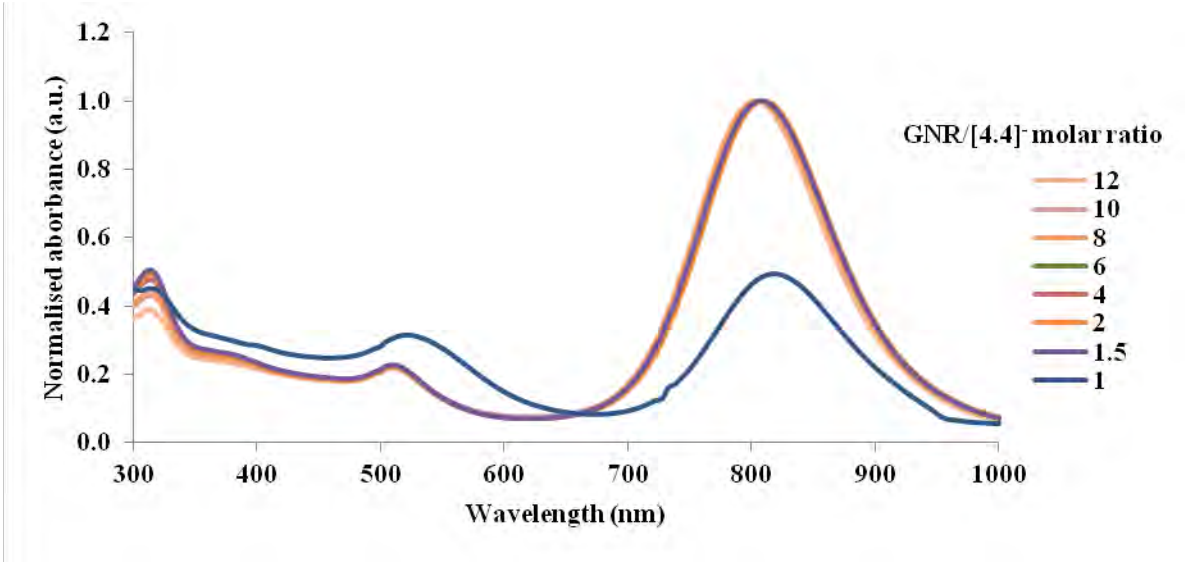

Figure 5.6. Normalised UV-Vis-NIR spectra of GNR-mPEG@[4.4]$^-$ with different GNR/**[4.4]**$^-$ molar ratios.

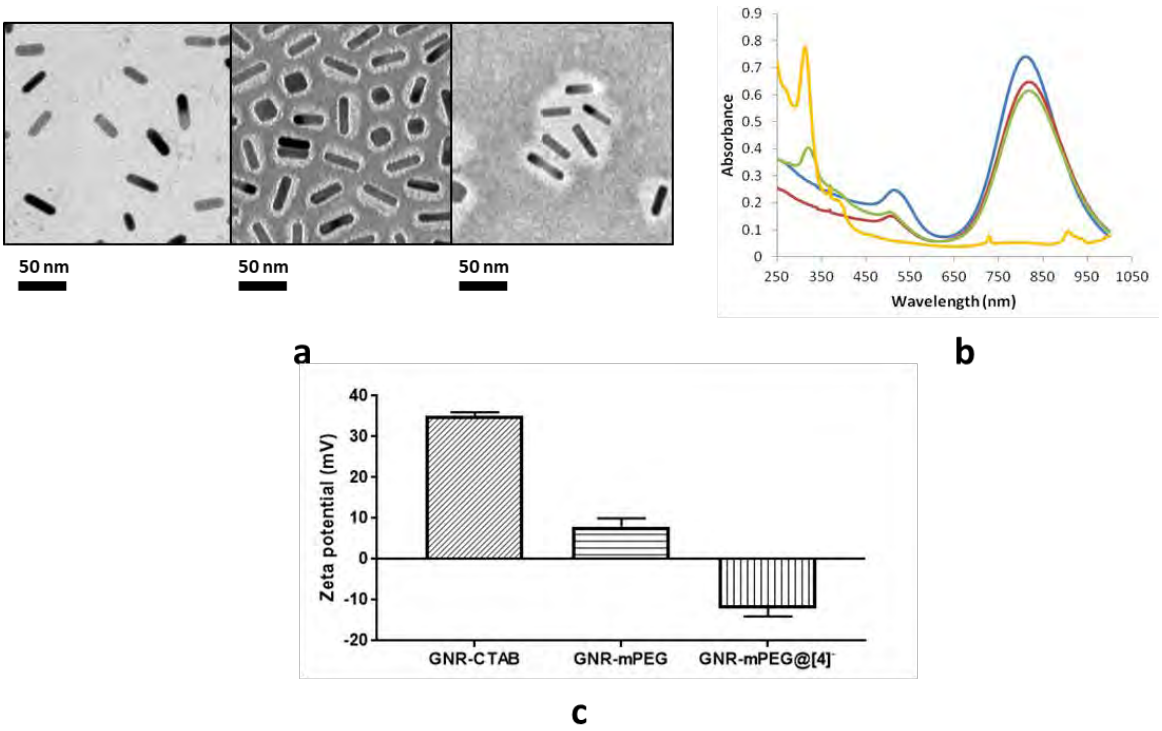

Figure 5.7. a) Representative transmission electron micrograph (TEM) of GNR-CTAB (left), GNR-mPEG (middle) and GNR-mPEG@[4.4]$^-$ (right); b) UV-vis-NIR absorption spectra of GNR-CTAB (blue line), GNR-mPEG (red line), GNR-mPEG@[4.4]$^-$ (green line) and compound [4.4]$^-$ (yellow line); and c) Zeta-potential values measured for GNR-CTAB, GNR-mPEG and GNR-mPEG@[4.4]$^-$.

As an additional structural evidence, the presence of COSAN on the surface was confirmed by scanning transmission electron microscopy (STEM) combined with energy-dispersive X-ray spectroscopy (EDXS). The energy bands in STEM-EDXS corresponding to cobalt and boron were observed, confirming the presence of **[4.4]**$^-$ on the surface of particles (Figure 5.8).

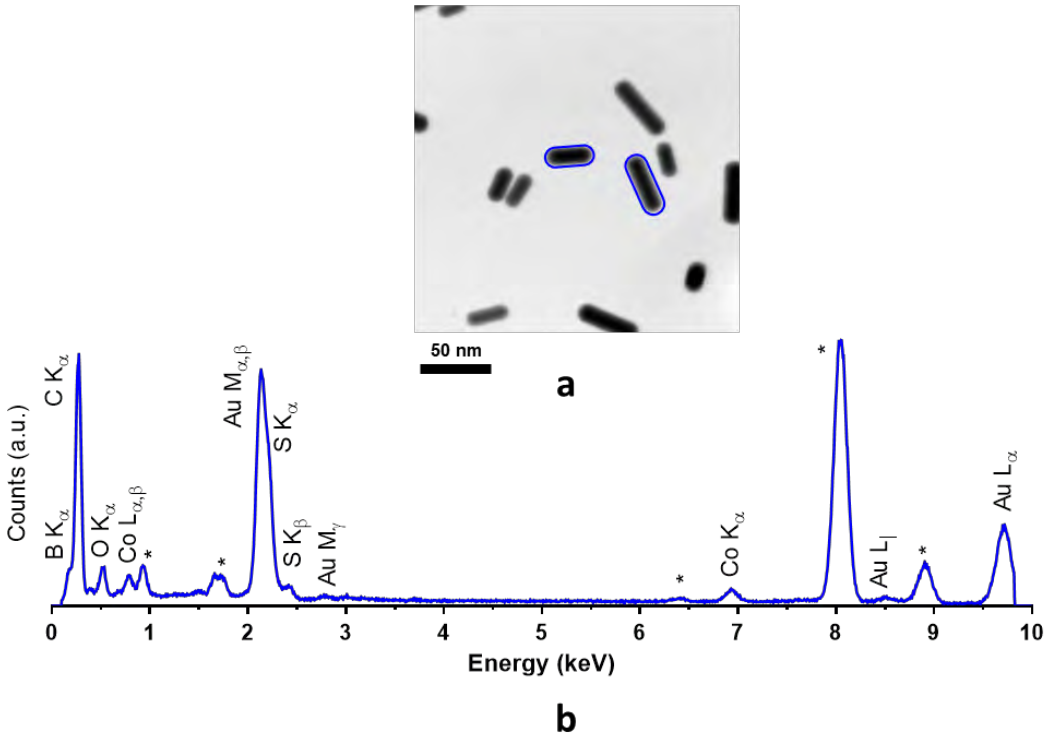

Figure 5.8. a) STEM images of GNR-mPEG@[4.4]$^-$; the areas analyzed with EDXS are delineated in blue; b) sum EDXS spectrum of the selected GNRs.

Furthermore, X-ray photoelectron spectroscopy (XPS) analysis of GNRs-mPEG@[4.4]$^-$ showed a peak at 780.2 eV in the Co spectrum, corresponding to Co-B bonds, and peaks at 192.8 and 188.5 eV, corresponding to B-O and C-B bonds, respectively (Figure 5.9) [14]. These results confirmed the presence of both cobalt and boron on the surface of the nanorods.

In order to determine the loading capacity of the system, ICP-MS analysis were performed to measure the gold and boron content in the final GNR-mPEG@[4.4]$^-$ (GNR/[4.4]$^-$ molar ratio 1.5). The amount of **[4.4]**$^-$ was estimated to be 225 μg per mg of gold, which results in ca. 100 μg of boron/mg of gold.

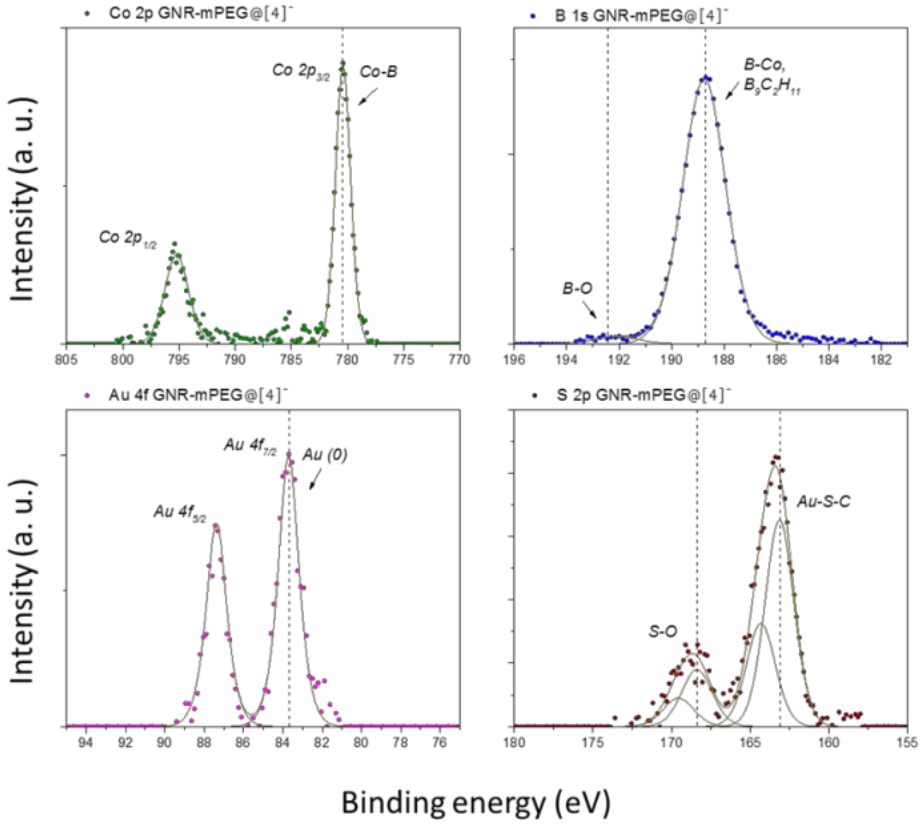

Figure 5.9. X-ray photoelectron spectroscopy (XPS) analysis of GNRs-mPEG@[4.4]$^-$

5.3.2 *In vitro* studies

Cytotoxicity studies

To evaluate the cell cytotoxicity of the multifunctional GNR-mPEG@[4.4]$^-$, the MKN-45 gastric adenocarcinoma and human dermal fibroblasts (HDFa) cell lines were used as *in vitro* models. These cell lines were treated with 10, 20, 40, 60, 80, and 100 μM (gold concentration) of the GNRs for up to 72 hours prior to analysis using the MTT assay.

The results (Figure 5.10) confirm that treatment of MKN-45 and HDFa cells with GNR-mPEG@[4.4]$^-$ did not reduce the viability of the cells at any of the concentrations assayed, indicating negligible cytotoxicity in this range of concentrations.

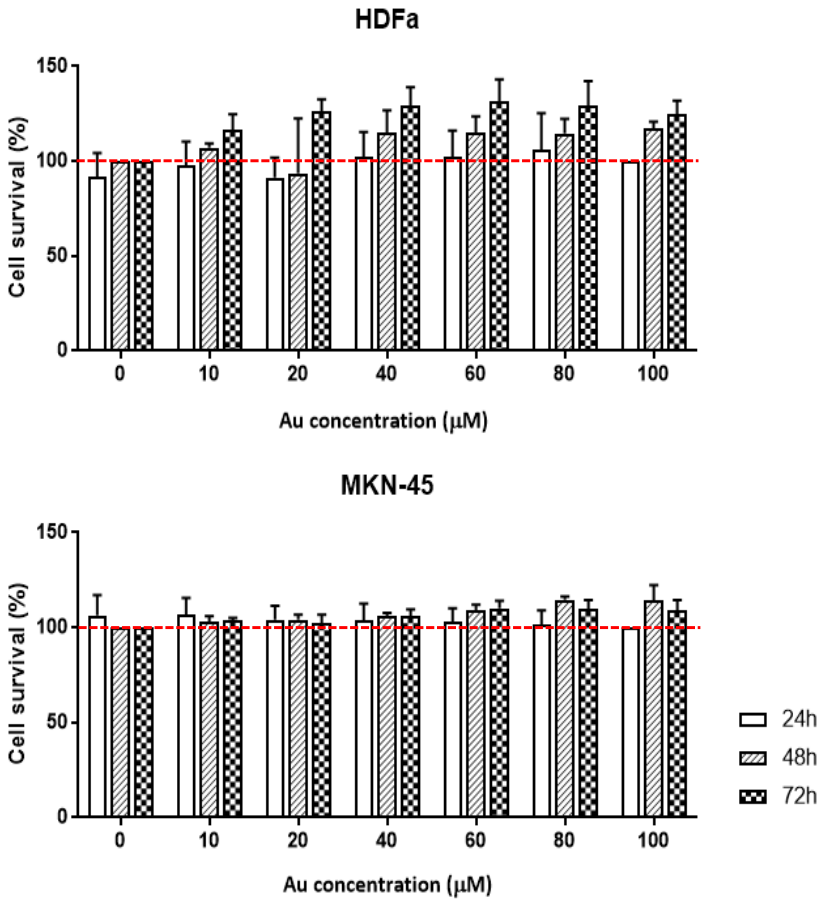

Figure 5.10. Cell viability in the presence of GNR-mPEG@[4.4]$^-$ for 24, 48 and 72 hours: a) MKN45 gastric cell line and b) human dermal fibroblasts (HDFa); in both cases, cells were incubated with increasing concentrations of GNRs and cell viability was determined by the MTT assay. Data are shown as the mean ± standard deviation of three independent experiments.

Cell internalization studies

Incubation of nanoparticles with cells seeded on a surface [two-dimension (2D) cell culture] is the most common method to evaluate the cellular uptake of nanoparticles. The cellular uptake of multifunctionalized GNRs was investigated in MKN-45 cells (as these are the cells inoculated for the generation of the tumor model, *vide infra*) using live cell fluorescence microscopy. With that aim, a fluorophore needed to be incorporated on the NPs. To enable conjugation with a fluorophore, GNR-mPEG@[4.4]$^-$ were reacted with PEG-amine-thiol (5kDa) at room temperature for 2h, centrifuged at 14000 rpm for 10 min and washed two times with water. Then, the fluorophore Cy3-NHS ester dissolved in DMSO was added to amino-functionalized GNR-mPEG@[4.4]$^-$ (pH 7.4-8.0) and stirred for 2h at room temperature, centrifuged at 14000 rpm for

10 min and washed two times with water. The fluorophore-labeled GNR-mPEG@[4.4]$^-$ were incubated with MKN-45 cells for 2 h. To enable co-localization between the GNR-mPEG@[4.4]$^-$ and the lysosomes, these were stained with Lysotracker-deep-red. Images were obtained using a live cell Axio Observer (Zeiss) fluorescence microscope and analyzed by the ZEN-ZEISS software, showing a clear co-localization between the GNR-mPEG@[4.4]$^-$ and the Lysosomes and therefore demonstrating internalization (Figure 5.11).

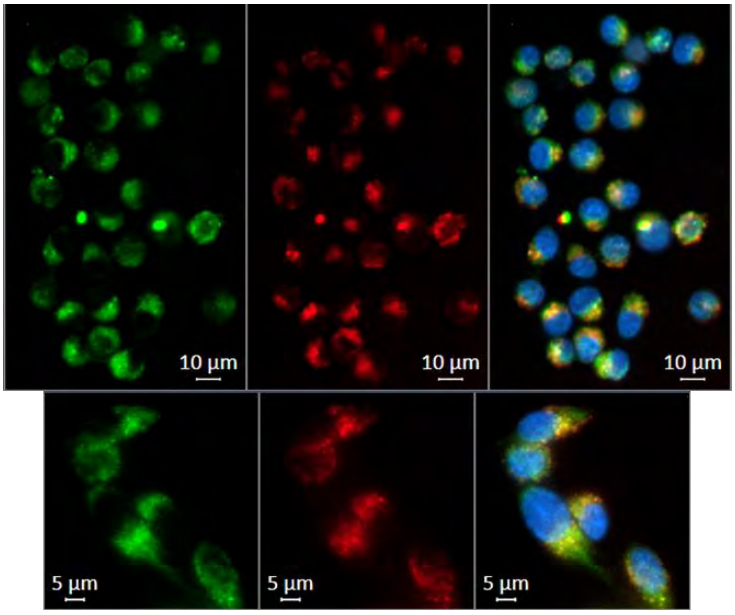

Figure 5.11. Live cell fluorescence microscopy of GNRs after 2 h incubation. In green: GNR-mPEG@[4.4]$^-$, fluorophore-labeled with NHS-Cy3; in red: Lysosomes, stained with LysoTracker deep red; in blue: nucleus, stained with Hoechst33342. Merged signals of GNR-mPEG@[4.4]$^-$, colocalizing with lysosomes appear in yellow.

5.3.3. Radiolabeling of GNRs-mPEG@[4.4]$^-$ with ^{64}Cu

To introduce PET imaging capabilities to nanosystems, one of the most common way consists of attaching the radionuclide ^{64}Cu via a metal chelator [15]. However, the possible detachment of the ^{64}Cu atom by transchelation from the chelator complex could lead to a significant difference between the radionuclide signal and the distribution of GNRs. A few years ago, Sun et al. reported a straightforward, facile synthesis of ^{64}Cu labeled gold nanomaterials for PET imaging guided therapy in a U87MG glioblastoma xenograft model [16]. Based on this protocol, multifunctional GNRs were labeled with ^{64}Cu radionuclide. In brief, [^{64}Cu]$CuCl_2$ was reduced in

the presence of hydrazine (N_2H_4) on the surface of GNRs-mPEG@[4.4]$^-$ at room temperature for 1 hour (Figure 5.12).

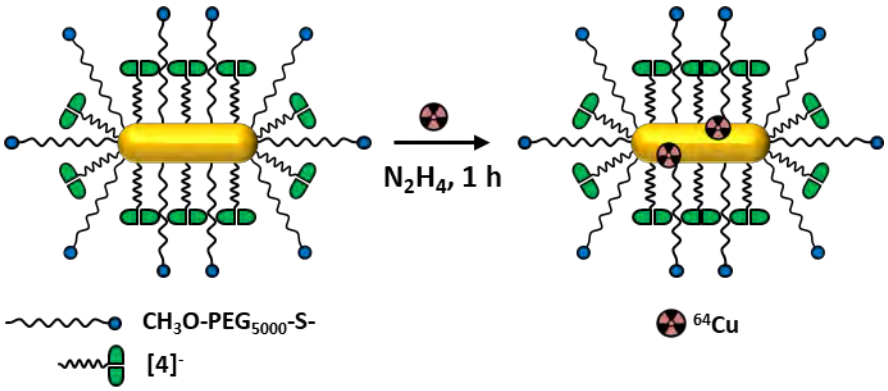

Figure 5.12. Schematic representation of radiolabeling of GNRs-mPEG@[4.4]$^-$ with ^{64}Cu.

After 1h, the synthesized GNRs-mPEG@[4.4]$^-$ were challenged with ethylenediaminetetraacetic acid (EDTA, 10 mM in neutral 50 mM phosphate buffer, 5 µL) and centrifuged at 14000 rpm for 10 min and washed two times with water. The radiochemical purity of [^{64}Cu]GNRs-mPEG@[4.4]$^-$ was monitored by using instant thin-layer chromatography (iTLC) paper (Agilent Technologies) with 20 mM citric acid and 60 mM EDTA/acetonitrile solution (9/1 v/v) as the stationary and mobile phases, respectively.

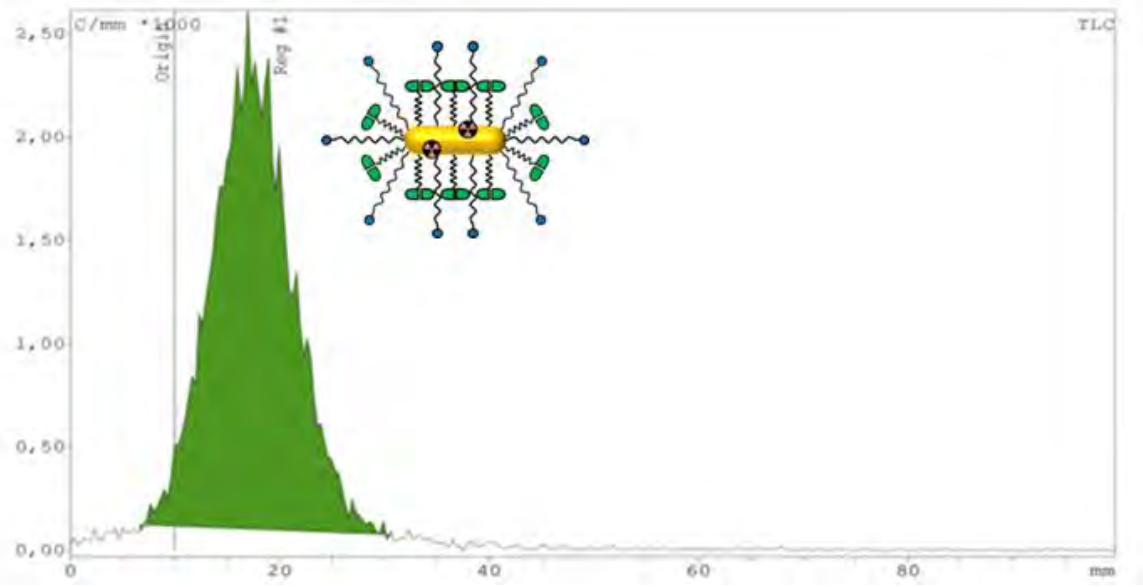

Figure 5.13. Radiochemical purity of [^{64}Cu]GNRs-mPEG@[4.4]$^-$

Radiochemical yields close to 70% were achieved and radiochemical purity was > 98% (Figure 5.13), as derived from the presence of one single peak in the chromatogram at the seeding position. Noteworthy, TEM images and UV-Vis-NIR spectra of GNRs-mPEG@[4.4]$^-$ (after radioactive decay) remained unaltered after incorporation of the ^{64}Cu radiolabel on the gold core, confirming the suitability of labeling method to tackle *in vivo* experiments (Figure 5.14).

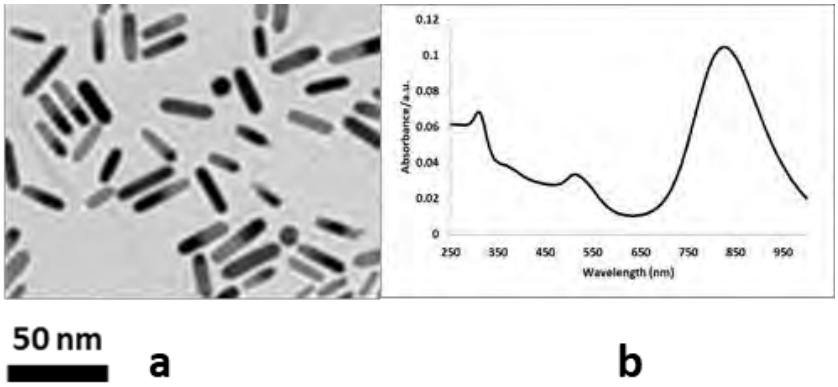

Figure 5.14. TEM image (a) and UV-Vis-NIR spectra (b) of [^{64}Cu]GNRs-mPEG@[4.4]$^-$ after complete radioactive decay).

5.3.4. Radiochemical stability

As mentioned in previous chapters, the stability of the radiolabel is paramount when performing *in vivo* experiments, because detachment of the radiolabel may lead to wrong interpretation of the imaging data. When radiometals are employed for radiolabeling, one of the most conclusive approaches to determine stability *in vitro* consists of incubating the labeled species in the presence of a chelator capable of sequestrating the radionuclide. Following this rationale, we investigated the radiochemical stability of [^{64}Cu]GNRs-mPEG@[4.4]$^-$ by incubation in three different media at 37 °C: (i) Physiological saline solution containing EDTA as a chelator (0.9% NaCl + 2.5 mM EDTA); (ii) phosphate buffered saline containing EDTA (PBS + 2.5 mM EDTA); and (iii) mouse serum.

The experiments confirmed the excellent stability of the radiolabel, as expected due to the incorporation on the gold core. Irrespective of the medium, >92% of the initial ^{64}Cu remained attached to GNRs-mPEG@[4.4]$^-$ at 48 h of incubation (Figure 5.15), thereby proving that the labeled GNRs are sufficiently stable to proceed to *in vivo* experiments.

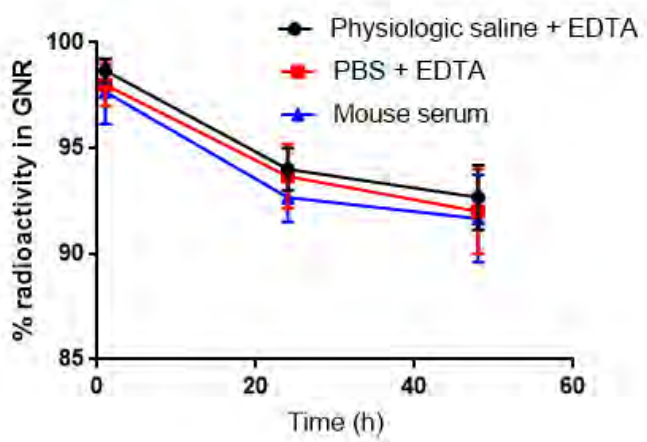

Figure 5.15. Radiochemical stability of GNR-mPEG@[4.4]$^-$ at different incubation times in: physiological saline solution containing EDTA (0.9% NaCl + 2.5 mM EDTA); phosphate buffered saline containing EDTA (PBS + 2.5 mM EDTA); and mouse serum.

5.3.5. *In vivo* studies

Following the investigation of *in vitro* toxicity and cell internalization, we tackled the determination of the biodistribution of the labeled nanorods in a xenograft mouse model generated by subcutaneous administration of MKN-45 cells, using PET imaging in combination with computerized tomography (CT) (Figure 5.16).

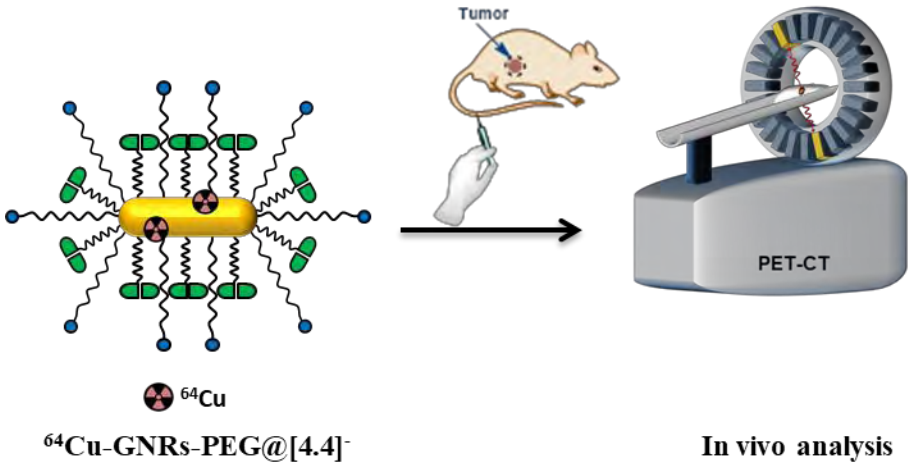

Figure 5.16. Schematic representation of *in vivo* analysis of [^{64}Cu]GNR-mPEG@[4.4]$^-$ using PET-CT

General biodistribution of the labeled GNRs and the accumulation in the tumor were determined by acquiring static PET images at different time points after administration of the labeled species

(1, 4, 24 and 48 hours; see Figure 5.17 for representative images). Volumes of interest (VOIs) were drawn in major organs and tumor tissue based on reconstructed CT images, and used to quantify PET images. The concentration of radioactivity in each region was determined as percentage of injected dose per cubic centimeter of tissue (%ID/cm^3) (Figure 5.18a).

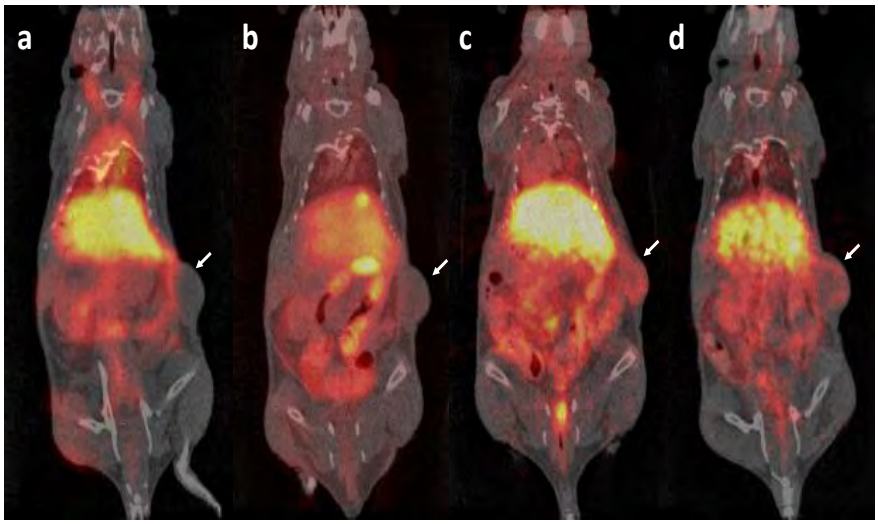

Figure 5.17. Representative PET images (coronal views) obtained at 1 (a), 4 (b), 24 (c), and 48 (d) hours after administration of [^{64}Cu]GNR-mPEG@[4.4]$^-$ in mice bearing MKN-45 tumor. Maximum intensity projection (MIP) PET images were co-registered with representative CT coronal slices. The position of the tumor is indicated with white arrows.

At t = 1 hour, high accumulation of radioactivity was observed in the heart (28.7±3.2 %ID/cm^3), suggesting the presence of a significant amount of labeled GNRs in the blood pool. This value progressively decayed with time, to reach a value of 2.22±0.16 %ID/cm^3 at t = 48 hours. A mono-exponential equation was fitted to the obtained values, to determine an estimated half-life of GNRs in blood of 1.4 hours (Figure 5.18d).

High accumulation of GNRs was observed in liver at short times after administration (26.3±2.8 %ID/cm^3), as well as in the lungs (14.6±3.0 %ID/cm^3) and spleen (13.7±1.8 %ID/cm^3). In these organs, a progressive decrease of radioactivity concentration was observed over time, reaching values of 15.5±3.9 %ID/cm^3, 0.96±0.5 %ID/cm^3 and 4.3±3.4 %ID/cm^3, respectively, at t = 48 hours after administration. These results suggest moderate sequestration of the NPs by organs of the mononuclear phagocyte system (MPS). Lower accumulation in kidneys (i.e. 9.3±1.0

%ID/cm^3), and no significant elimination via urine were observed, suggesting a very slow glomerular filtration rate, and hence confirming the stability of the label. A progressive decrease of the amount of GNRs found in liver and kidneys is important because this trend may reduce local side- or toxic effects in eventual long-term treatments.

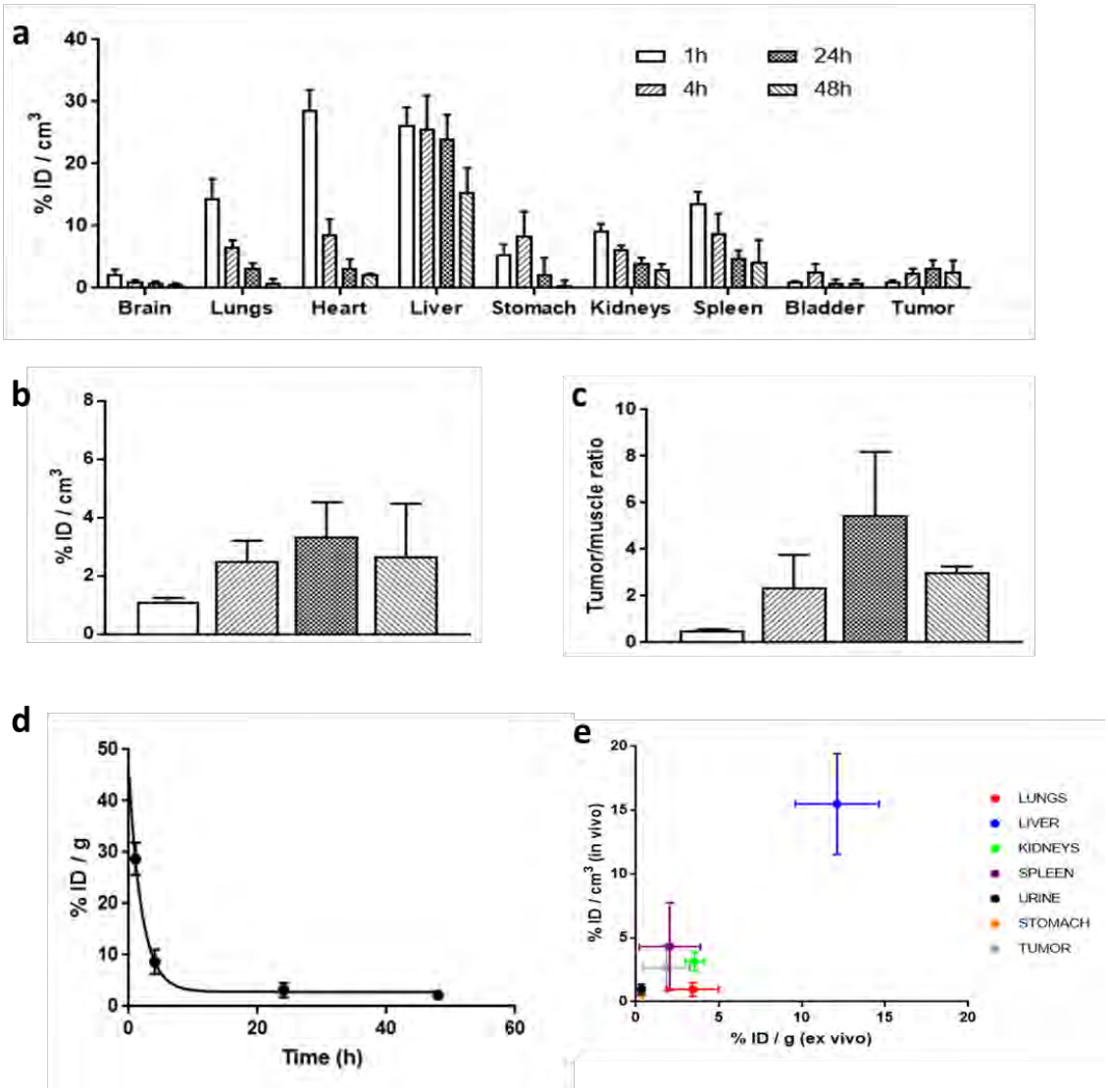

Figure 5.18. (a,b) Accumulation of [^{64}Cu]GNR-mPEG@[4.4]$^-$ in different organs (a) and the tumor (b) at different time points after intravenous administration, as determined by PET imaging; (c) tumor-to-muscle ratios at different time points; (d) Time activity curve in blood; (e) correlation of results obtained by *in vivo* imaging and dissection/gamma counting. In all cases, values are expressed as mean ± standard deviation (n=4).

Noteworthy, the concentration of radioactivity in the tumor progressively increased with time (Figure 5.18b) to reach the maximum value at t = 24 hours (3.3±1.2 %ID/cm^3) and slowly decreased afterwards (2.7±1.8 %ID/cm^3 at t =48 hours). The tumor-to-muscle ratio showed a similar trend, reaching the maximum of 5.4±2.7 at t = 24 hours after administration (Figure 5.18c).

5.3.6. *Ex vivo* studies

In vivo biodistribution results were confirmed by *ex vivo* gamma-counting experiments, conducted immediately after finalizing the last imaging session. Mice were sacrificed after 48 h time point, organs of interest were harvested and the amount of radioactivity in each organ was measured in an automated gamma-counter (Wallach Wizard, PerkinElmer, Waltham, MA, USA). As depicted in Figure 5.18e, a good correlation between *in vivo* and *ex vivo* results was achieved. Major differences were encountered in the lungs. This is somehow expected, as the values determined *in vivo* (using PET imaging) are expressed as %ID/cm^3, because volumes of interest are delineated. However, values obtained *ex vivo* correspond to %ID/g, and hence *in vivo* and *ex vivo* data should match only when the density of the tissue investigated is close to 1. This is not the case for a breathing lung under physiological conditions, where the density is assumed to be close to 0.5 g/cm^3 due to the presence of a large volume of air.

Our results above assume that the GNRs are chemically and radiochemically stable over the whole duration of the study, this is, that the imaging results reflect the real accumulation of GNR-mPEG@[4.4]$^-$ in different organs and tumor tissue. Despite the low elimination via urine suggest that the radiolabel does not detach from the NPs, it is not a proof of the chemical stability of the NPs.

In order to prove that the presence of radioactivity in the tumor (as well as other organs) can be correlated with the actual concentration of nanoparticles (and boron), the concentration of boron and gold in selected organs (spleen, liver) as well as in the tumor were determined by ICP-MS (Figure 5.19). As it can be seen, a good correlation between results obtained by ICP-MS and *in vivo* imaging was achieved, confirming the stability of our functionalized GNRs and their capacity to reach the tumor.

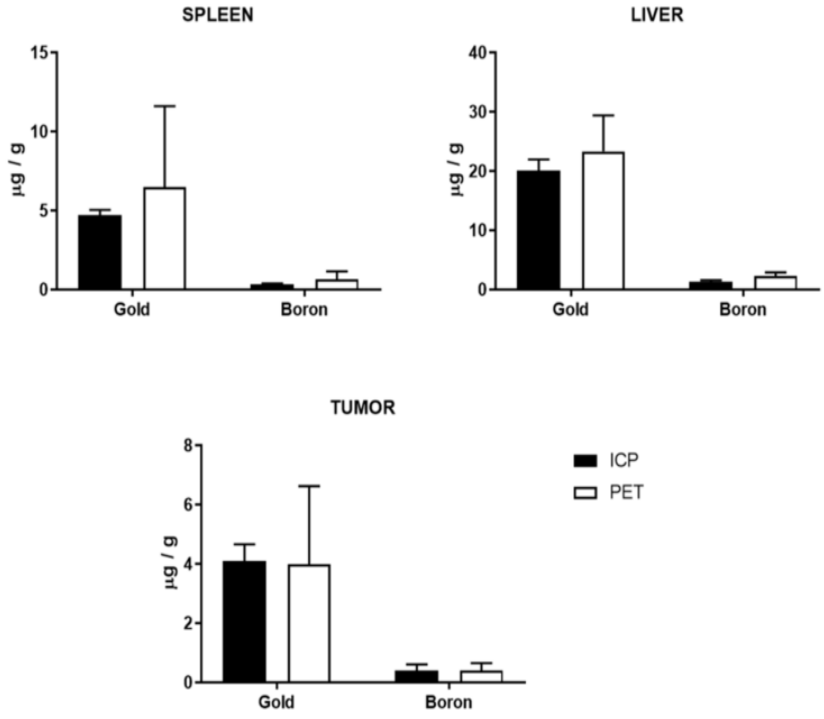

Figure 5.19. Amount of gold and boron in the spleen, the liver and the tumor at 48 hours after intravenous administration of GNR-mPEG@[4.4]$^-$, as determined by ICP-MS and PET imaging. Values for PET imaging are obtained by multiplying the %ID/cm^3 (values from Figure 5.18a) by the relative load of boron and gold in the nanosystems.

Our biodistribution data are in good agreement with results reported in the literature. Although no examples of boron-rich GNRs have been reported, GNRs bearing other functionalities have been assayed *in vivo*. In one of the examples reported, non-targeted, PEG-stabilized GNRs were evaluated in a xenograft mouse model of breast cancer and maximum accumulation in the tumor was observed at 6–24 hours after administration, with values slightly above 5% ID/g. These uptake values could be significantly increased by covalently attaching a bombesin peptide to the GNRs. The authors also observed high accumulation in liver and kidneys [17]. In a more recent work [18], slightly larger (93.4 nm in length, 24.8 nm in width; aspect ratio = 3.8) PEG-stabilized GNRs functionalized with Arg-Gly-Asp- (RGD-) peptides were assayed in a mouse model of melanoma generated by subcutaneous inoculation of $\alpha_v\beta_3$-positive B16F10 mouse malignant melanoma cells. Maximum accumulation at 6 hours after administration was observed in liver

(26.51±4.93 %ID/g), lungs (7.07±0.25 %ID/g) and spleen (5.55±0.69 %ID/g), while accumulation in the tumor was 5.09±0.68 %ID/g and the tumor-to-muscle ratio was close to 10.

We calculated the amount of boron accumulated in the tumor at different times after administration based on PET imaging results. Considering that: (i) the injected dose to the animal was 150 μg of GNR-mPEG@[4.4]$^-$ (amount of gold); (ii) GNRs contain 100μg boron per mg of gold; and (iii) the concentration of GNRs in the tumor at t = 24 hours after administration is 3.3±1.2 %ID/cm^3, the average concentration of boron in the tumor at t = 24 hours is 0.5 μg/cm^3. This value is below the commonly accepted threshold to guarantee therapeutic efficacy in stand-alone BNCT therapy. Higher values could however be easily achieved by administering higher or repeated doses.

The values obtained with our nanosystems are significantly lower than those achieved with other nanocarriers. For example, the administration of carborane-appended water-soluble single-wall carbon nanotubes (administered dose per animal 4.6-10 mg) in a mouse model of mammary carcinoma resulted in boron concentration of almost 30 μg/cm^3 [19]. In another, more recent work, boron-conjugated micelles with a boron load of 7.7 wt% were investigated in a mouse model of colon cancer, resulting in tumor uptake values close to 5 %ID/g in a time window between 24 and 48 hours after administration [20]. Intravenous administration of a dose of 15.6 mg/kg to tumor-bearing mice was sufficient to retard growth significantly after neutron irradiation.

It is worth mentioning that comparison of tumor accumulation of different boron-rich nanosystems should be performed with care, as different tumor models could lead to very different tumor accumulation values, even when experiments are performed at the same site and under identical experimental conditions. Our nanosystems, despite resulting in lower accumulation than that required to guarantee efficacious therapy, have the advantage of being capable to respond to light stimulus generating local heat, thus enabling combined BNCT and photothermal therapies.

5.4. Summary and conclusions

In this chapter, we developed a synthetic strategy for the preparation of GNRs simultaneously functionalized with mPEG$_{5k}$-SH and a thiolated COSAN analogue (GNR-mPEG@[4.4]$^-$).

Monidisperse and stable GNRs could be obtained with an aspect ratio of 3.7 (37±3 × 10±1 nm; length × width). The resulting GNRs showed good internalization capacity in MKN45 cells and low toxicity both in MKN45 and human dermal fibroblasts (HDFa). Treatment of the GNRs with $^{64}CuCl_2$ in the presence of a reducing agent enabled the incorporation of the positron emitter at the gold core, resulting in stable labeling in different media. *In vivo* experiments in a xenograft mouse model generated by inoculation of MKN45 cells showed significant accumulation of the GNR-mPEG@[4.4]$^-$ in the tumor and good tumor-to-muscle ratios at 24–48 hours after administration. Such multidecorated GNRs carry large amounts of boron, and hence bear the potential to become a valuable tool for the development of nanoparticle-based BNCT agents. This, together with the capability to absorb near infrared light, opens new avenues for their use in combined therapies (BNCT + photothermal therapy)

5.5. Experimental section

5.5.1. Reagents

Cesium cobalt(III) *bis*(dicarbollide) (COSAN) (Katchem Ltd., Prague, Czech Republic), tetrahydropyran (sigma-Aldrich), hexadecyltrimethylammonium bromide (CTAB, Sigma), gold(III) chloride trihydrate ($HAuCl_4 \cdot 3H_2O$, Aldrich), sodium borohydride ($NaBH_4$, Aldrich), silver nitrate ($AgNO_3$, Sigma-Aldrich), ascorbic acid (Sigma), potassium carbonate (K_2CO_3, Sigma-Aldrich), poly (ethylene glycol) methyl ether thiol (MW 5000, Nektor), Cy3-NHS (BroadPharm®), and hydrazine hydrate (50–60%) (Sigma-Aldrich) were used as purchased. All other reagents and anhydrous solvents, stored over 4 Å molecular sieves, were purchased from Aldrich Chemical Co. (Madrid, Spain) and used without further purification. HPLC grade solvents were purchased from Scharlab (Sentmenat, Barcelona, Spain). $^{64}Cu^{2+}$ in 0.1 M HCl was produced at CIC biomaGUNE Radiochemistry facility using cyclotron via the $^{64}Ni(p,n)^{64}Cu$ nuclear reaction.

For chemical reactions, experiments were carried out under a dry, oxygen-free dinitrogen atmosphere unless otherwise noted. Analytical thin layer chromatography (TLC) measurements were conducted with silica gel 60 F_{254} plates (Macherey-Nagel).

5.5.2. Instrumentation:

The ^{1}H-NMR (500 MHz), ^{13}C-NMR (126 MHz) and ^{11}B-NMR (160 MHz) spectra were recorded on a 500-MHz Avance III Bruker spectrometer. All NMR spectra were performed in deuterated solvents at 22 °C. The ^{11}B-NMR shifts were referenced to external $BF_3 \cdot OEt_2$, while the ^{1}H and ^{13}C-NMR shifts were referenced to $SiMe_4$. Chemical shifts are reported in units of parts per million (ppm) downfield from the reference peak and all coupling constants are reported in Hertz (Hz).

UPLC/ESI-MS analyses were performed using an AQUITY UPLC separation module coupled to LCT TOF Premier XE mass spectrometer (Waters, Manchester, UK). An Acquity BEH C18 column (1.7 μm, 5 mm, 2.1 mm) was used as stationary phase. The elution buffers were A (water and 0.1% formic acid) and B (Methanol and 0.1% formic acid). The column was eluted with gradient: t=0 min, 95% A, 5% B; t=0.5 min, 95% A, 5% B; t=5.5 min, 25% A, 75% B; t=16 min, 1% A, 99% B; t=20min, 1% A, 99% B. Total run was 20 min, injection volume was 5 μL and flow rate 300 μL/min. The detection was carried out in both, negative and positive ion mode, monitoring the most abundant isotope peaks from the mass spectra ($M\text{-}H^+$) or ($M+H^+$).

Transmission electron microscopy (TEM) was performed using a JEOL JEM-1400 plus microscope (Jeol, Tokyo, Japan) working at 120 kV. The carbon film of copper grids (CF400-Cu) was treated under air plasma in a glow discharge system (Emitech K100X, 40mA during 2 min) just before sample preparation. For TEM examinations, a single drop (1 μL) of the NPs solution was placed onto a copper grid coated with a carbon film (Electron Microscopy Sciences). After 1 minute, the drop was removed with filter paper and the sample was incubated with 3 μL of uranyl acetate 0.5% (3 min). The drop was removed with filter paper and the grid placed on top of a drop of water twice and dried with a filter paper. Scanning transmission electron microscopy (STEM) images were taken in a JEOL JEM-2100F (200kV, HAADF detector, coupled with an EDXS-INCA Oxford system). Energy dispersive X-ray spectroscopy (EDXS) of selected areas was carried out for thirty minutes, in which the sample displacement was automatically corrected every two minutes. A clear grid region without particle presence was analysed to evaluate the presence of scattered signals coming from the detector, grid and equipment microscope composition (Copper, Silicon and Iron, among others). These non-relevant signals were omitted (<0.1 keV) or asterisk-labeled in the spectrum.

XPS experiments were performed in a SPECS Sage HR 100 spectrometer with a non-monochromatic X ray source (Aluminium Kα line of 1486.6 eV energy and 252 W), placed perpendicular to the analyser axis and calibrated using the 3d5/2 line of Ag with a full width at half maximum (FWHM) of 1.1 eV. The selected resolution for the spectra was 15 eV of Pass Energy and 0.15 eV/step. All measurements were made in an ultra-high vacuum (UHV) chamber at a pressure around 6×10^{-8} mbar. An electron flood gun was used for charge neutralisation. Gaussian Lorentzian functions were used for fittings (after a Shirley background correction) where the FWHM of all the peaks were constrained while the peak positions and areas were set free. Main C1s peak was used for charge reference and set at 284.8 eV.

ICP-MS measurements were performed on a Thermo iCAP Q ICP-MS (Thermo Fisher Scientific GmbH, Bremen, Germany). An ASX-560 autosampler was coupled to the ICP-MS (CETAC Tech, Omaha, NE, USA). UV-Vis-NIR spectra were measured in an Agilent 8453 UV-Vis-NIR diode-array spectrophotometer. ξ-potential measurements were performed using a Malvern Zetasizer Nano ZS system (Malvern Instruments, Malvern, UK). Radio-thin layer chromatography (radio-TLC) was performed using iTLC-SG chromatography paper (Agilent Technologies, CA, USA) and 20 mM citric acid + 60 mM EDTA/acetonitrile solution (9/1 v/v) as the stationary and mobile phases, respectively. TLC plates were analyzed using a TLC-reader (MiniGITA, Raytest).

Cell observer microscopy experiments were carried out using a Zeiss Axio Observer Fluorescence microscope using Ibidi clear bottomed μ-slide 8-well microscopy plates and analyzed by ZEN2012-ZEISS.

Confocal cell microscopy experiments were carried out using a Zeiss 880 Confocal Fluorescence microscope using Ibidi clear bottomed μ-slide 8-well microscopy plates and analyzed by ZEN2012-ZEISS.

5.5.3. Chemistry

Synthesis of GNRs using seedless growth method

Gold Nanorods (GNRs) were synthesized following a seedless growth method. $HAuCl_4$ (100 μL, 0.05 M) was added to 10.0 mL of cetyltrimethylammonium bromide (CTAB; 0.1 M) and shaken. Following this, $AgNO_3$ (250 μL, 4.0 mM) was added, and the solution was gently shaken. HCl

(12.0 µL, 37 wt%) was introduced to obtain a pH close to 1.0 followed by addition of 70 µL of ascorbic acid (78.8 mM) under gentle stirring until the solution became clear. In the final step, ice-cold $NaBH_4$ (10 µL, 0.01 M) was injected into the growth solution and allowed to react for 6 h. The growth solution was maintained at 27 °C in a water bath. The synthesized GNRs were centrifuged twice at 10.000×g to remove the excess CTAB as well as other reagents, and re-dispersed in water.

Synthesis of PEG-modified GNRs

A GNR solution as prepared above was centrifuged at 10.000×g for 10 min, decanted, and resuspended in water to remove excess CTAB. A thiol-terminated PEG solution (300 µL, 10 mM, Nektor, MW ca. 5000, mPEG-SH) was added to the centrifuged GNR solution (2 mL; 1mM Au). The mixed solution was stirred for 24 hours at room temperature, and centrifuged twice at 10.000×g for 10 min, decanted, and re-suspended in water to remove excess PEG reagent.

Synthesis of PEG-stabilized, COSAN-functionalized GNRs

To the PEG-modified GNRs (2 mL; 1 mM Au), 150 µL of a fresh solution of COSAN-SH $[4.4]^-$ in ethanol (3 mg/mL) were quickly added and stirring was maintained for 2 hours. The resulting NPs were centrifuged at 8.000×g for 20 min and resuspended in ultrapure water three times to remove excess COSAN-SH reagent, and re-dispersed in 1.0 mL ultrapure water.

Synthesis of ^{64}Cu-Integrated GNR-mPEG-COSAN

$^{64}CuCl_2$ produced by proton irradiation of ^{64}Ni as previously described [21], was diluted into 0.4 M ammonium acetate buffer (NH_4Ac, pH 5.5). A 500 µCi ^{64}Cu solution was then added dropwise into the mPEG-stabilized, COSAN-functionalized GNRs solution (Au Concentration=250 µg/mL). After stirring for 5 min, 3 µmol of N_2H_4 was added, and the solution was allowed to react at room temperature for 1 hour before it was washed by centrifugation to remove the excess reagents as well as the unreacted ^{64}Cu. The labeling efficiency was calculated based on radiation dosimeter readings before and after purification. The labeling efficiency was determined by using instant thin-layer chromatography (ITLC) plates with 20 mM citric acid and 60 mM EDTA/acetonitrile solution (9/1 v/v) as an eluent.

Synthesis of fluorophore labeled PEG-stabilized, COSAN-functionalized GNRs

The synthesis was performed as described previously with the difference of using 20 % PEG-amine and 80 % PEG-methoxy to enable labeling with the fluorophore Cyanine3-NHS. Therefore 200 µL of functionalized AuNP (1 mg/mL for rods and medium in MQ water) were adjusted in pH to 8.6-8.9 and 5 µL Cy3-NHS (1 mg/mL in DMSO) were added. After 1 h incubation at room temperature, the resulting NPs were centrifuged at 8.000×g for 20 min and resuspended in ultrapure water. The labeling was confirmed by UV-VIS spectrophotometry.

5.5.4. *In vitro* studies

Cytotoxicity studies

To determine cell viability, MKN45 human gastric cancer cells and human dermal healthy fibroblasts (HDFa) cells were incubated with the GNRs over 24, 48 and 72 hours. Cells were seeded (3×10^4 cells/well, 100 µL/well, 96-well plate), allowed to adhere overnight in complete media (10% Fetal Bovine Serum (FBS) and 1% Penicillin/Streptomycin in RPMI 1640 medium for MKN45 cells and DMEM medium for HDFa cells) and maintained in a humid atmosphere at 37°C and 5% CO_2. Then, media was removed and cells were left untreated (blank) or incubated with the GNR-containing formulations, diluted accordingly in media. The experiments were performed in triplicates. After the desired time, cell supernatant was removed and 100 µL/well of MTT reagent (Roche), diluted in the corresponding media to the final concentration of 0.25 mg/mL, was added. After 1 hour incubation at 37°C and 5% CO_2, the excess reagent was removed and formazan crystals were solubilized by adding 200 µL of DMSO per well. The optical density of each well was measured in a TECAN Genios Pro 96/384 microplate reader at 550 nm. Data was represented as the percentage of cell survival compared to control wells.

Cell internalization studies

MKN45 cells were seeded in an 'Ibidi' µ-slide 8-well-plate (20 000 cells/well in 0.3 mL) and incubated over night to adhere (37 °C, 5% CO_2, humid atmosphere). The media was removed and 0.1 mL Hoechst 33342 (1 µg/mL in media) added to stain the nucleus. After 10 min incubation (37 °C, 5% CO_2, humid atmosphere) 0.1 mL LysoTracker deep red (1 µg/mL in media) was added to stain the lysosomes. After 20 min incubation (37 °C, 5% CO_2, humid atmosphere) media was removed and 0.3 mL of Cy3-labeled AuNP (20 µg/mL in medium) added. After 2 h

incubation (37 °C, 5% CO_2, humid atmosphere) the media was removed and replaced with fresh media. The images were taken with a Cell Axio Observer Fluorescence Microscope. Controls of single staining for each fluorophore were included. Images were analyzed by ZEN-ZEISS software.

5.5.5. *In vivo* experiments

Animals

The animals were maintained and handled in accordance with the Guidelines for Accommodation and Care of Animals (European Convention for Protection of Vertebrate Animals Used for Experimental and Other Scientific Purposes) and internal guidelines. Experimental procedures were approved by the ethical committee and local authorities. All animals were housed in ventilate cages and fed on standard diet *ad libitum*.

MKN45 mouse tumor model development

In order to study the biodistribution of the GNRs in tumor-bearing mice, Rj:NMRI-*Foxn1*$^{nu/nu}$ female mice (7-8 weeks old, Janvier) were subcutaneously inoculated with 2×10^6 MKN45 tumor cells in the right back. Prior to each inoculation, cells were diluted in sterile PBS:Matrigel (1:1) and mycoplasma test (Lonza) was carried out to ensure that cells were not contaminated. Tumors were measured every 2–3 days with a digital caliper and volumes were calculated as V (mm^3) = [(short diameter)^2 x (long diameter)]/2. Biodistribution studies were carried out when tumor volume was approximately 200–300 mm^3 (~15 days after tumor inoculation).

Biodistribution studies

PET studies with ^{64}Cu-labeled multifunctionalized GNRs were carried out in MKN45 tumor-bearing mice (n=4 per compound) using an eXplore Vista-CT small animal PET-CT system (GE Healthcare). Anesthesia was induced with 3% isoflurane and maintained by 1.5 to 2% of isoflurane in 100% O_2. For intravenous administration of the radiotracer, the tail vein was catheterized with a 24-gauge catheter and the labeled NPs (ca. 3–10 MBq) were injected. PET images were analyzed using PMOD image analysis software (PMOD Technologies Ltd, Zürich, Switzerland). Volumes of interest (VOIs) were manually drawn in lungs, liver, heart, kidneys, spleen, brain, stomach, tumor and bladder using CT images as anatomical reference. VOIs were

then transferred to the PET images and time activity curves (decay corrected) were obtained for each organ as cps/cm^3. Curves were transformed into real activity (Bq/cm^3) curves. Injected dose normalization was finally applied to data to get time activity curves as percentage of injected dose per cm^3 of tissue (%ID/cm^3).

Ex vivo studies

The mice were sacrificed at 48 hours post injection, after the last imaging session. Organs of interest were collected and weighed, and the radioactivity was measured in a well gamma-counter (Wallach Wizard, PerkinElmer, Waltham, MA, USA). The uptake of ^{64}Cu in the various organs was calculated as a percentage of the injected dose per gram of tissue (%ID/g) according to the prepared standards. The weighed organs (liver, spleen and tumor) were then immersed in digest solution (HNO_3/HCl = 1:1) with a volume of 5 mL. The dispersions were heated to boiling until organs were completely dissolved. 1 mL of H_2O_2 was then added into the solution, and heating continued until the solution became clear and transparent. The solution was then cooled to room temperature, diluted by 2% HNO_3 to 10 mL, and subsequently analyzed by ICP to determine the concentration of Au and B in each sample.

5.6. References

1. Champion JA, Katare YK, Mitragotri S. Particle shape: A new design parameter for micro- and nanoscale drug delivery carriers. *Journal of Controlled Release*. **2007**;121(1-2):3-9.

2. Wei Y, Quan L, Zhou C, Zhan Q. Factors relating to the biodistribution & clearance of nanoparticles & their effects on in vivo application. *Nanomedicine*. **2018**;13(12):1495-512.

3. Alfranca G, Beola L, Liu Y, Gutiérrez L, Zhang A, Artiga A, Cui D, De La Fuente JM. In vivo comparison of the biodistribution and long-term fate of colloids - gold nanoprisms and nanorods - with minimum surface modification. *Nanomedicine*. **2019**;14(23):3035-55.

4. Haine AT, Niidome T. Gold nanorods as nanodevices for bioimaging, photothermal therapeutics, and drug delivery. *Chemical and Pharmaceutical Bulletin*. **2017**;65(7):625-8.

5. Xia K, Zhang L, Huang Y, Lu Z. Preparation of gold nanorods and their applications photothermal therapy. *Journal of Nanoscience and Nanotechnology*. **2015**;15(1):63-73.

6. Xu W, Lin Q, Yin Y, Xu D, Huang X, Xu B, Wang G. A review on cancer therapy based on the photothermal effect of gold nanorod. *Current Pharmaceutical Design*. **2019**;25(46):4836-47.

7. Ali MRK, Snyder B, El-Sayed MA. Synthesis and optical properties of small Au nanorods using a seedless growth technique. *Langmuir*. **2012**;28(25):9807-15.

8. Gómez-Graña S, Hubert F, Testard F, Guerrero-Martínez A, Grillo I, Liz-Marzán LM, Spalla O. Surfactant (Bi) layers on gold nanorods. *Langmuir*. **2012**;28(2):1453-9.

9. Alkilany AM, Nagaria PK, Hexel CR, Shaw TJ, Murphy CJ, Wyatt MD. Cellular uptake and cytotoxicity of gold nanorods: Molecular origin of cytotoxicity and surface effects. *Small*. **2009**;5(6):701-8.

10. Prencipe G, Tabakman SM, Welsher K, Liu Z, Goodwin AP, Zhang L, Henry J, Dai H. PEG branched polymer for functionalization of nanomaterials with ultralong blood circulation. *Journal of the American Chemical Society*. **2009**;131(13):4783-7.

11. Akiyama Y, Mori T, Katayama Y, Niidome T. The effects of PEG grafting level and injection dose on gold nanorod biodistribution in the tumor-bearing mice. *Journal of Controlled Release*. **2009**;139(1):81-4.

12. Akiyama Y, Mori T, Katayama Y, Niidome T, editors. The effect of PEG grafted on gold nanorods and their injection dose on biodistribution in tumor-bearing mice. Materials Research Society Symposium Proceedings; 2010.

13. Boca SC, Astilean S. Detoxification of gold nanorods by conjugation with thiolated poly(ethylene glycol) and their assessment as SERS-active carriers of Raman tags. *Nanotechnology*. **2010**;21(23).

14. NIST X-ray Photoelectron Spectroscopy Database [database on the Internet]. Measurement Services Division of the National Institute of Standards and Technology (NIST). 2012 [cited 08/07/2019].

15. Martín IG, Frigell J, Llop J, Marradi M. Radiolabelling of NPs using radiometals: ^{99m}Tc, ^{68}Ga, ^{67}Ga, ^{89}Zr, and ^{64}Cu. Isotopes in Nanoparticles: Fundamentals and Applications2016. p. 183-229.

16. Sun X, Huang X, Yan X, Wang Y, Guo J, Jacobson O, Liu D, Szajek LP, Zhu W, Niu G, Kiesewetter DO, Sun S, Chen X. Chelator-free ^{64}Cu-integrated gold nanomaterials for positron emission tomography imaging guided photothermal cancer therapy. *ACS Nano*. **2014**;8(8):8438-46.

17. Heidari Z, Salouti M, Sariri R. Breast cancer photothermal therapy based on gold nanorods targeted by covalently-coupled bombesin peptide. *Nanotechnology*. **2015**;26(19).

18. Zhang Y, Yin L, Xia X, Hu F, Liu Q, Qin C, Lan X. Synthesis and bioevaluation of Iodine-131 directly labeled cyclic RGD-PEGylated gold nanorods for tumor-targeted imaging. *Contrast Media and Molecular Imaging*. **2017**;2017.

19. Yinghuai Z, Peng AT, Carpenter K, Maguire JA, Hosmane NS, Takagaki M. Substituted carborane-appended water-soluble single-wall carbon nanotubes: New approach to boron neutron capture therapy drug delivery. *Journal of the American Chemical Society*. **2005**;127(27):9875-80.

20. Sumitani S, Oishi M, Yaguchi T, Murotani H, Horiguchi Y, Suzuki M, Ono K, Yanagie H, Nagasaki Y. Pharmacokinetics of core-polymerized, boron-conjugated micelles designed for boron neutron capture therapy for cancer. *Biomaterials*. **2012**;33(13):3568-77.

21. Kume M, Carey PC, Gaehle G, Madrid E, Voller T, Margenau W, Welch MJ, Lapi SE. A semi-automated system for the routine production of copper-64. *Applied Radiation and Isotopes*. **2012**;70(8):1803-6.

Chapter 6: Conclusions and future directions

6.1. General conclusions

1. Four gold-based, water-soluble, biocompatible and shape and size-tuned nanosystems, stabilized with polyethylene glycol and functionalized with the boron-rich anion cobalt bis(dicarbollide) (COSAN) could be successfully synthesized and characterized for their evaluation as drug candidates in the context of boron neutron capture therapy (BNCT).
2. The nanosystems showed low *In vitro* cytotoxicity and good cell internalization capacity in different cell lines.
3. The nanosystems could be efficiently radiolabeled with different positron emitters, namely iodine-124 and copper-64, enabling the *in vivo* monitoring using positron emission tomography (PET) imaging.
4. Incorporation of the positron emitter iodine-124 both at the core and the shell of spherical gold nanoparticles with core size 18-21 nm and subsequent investigation using PET imaging in a xenograft mouse model of human fibrosarcoma, confirmed *in vivo* stability of the nanosystems, high accumulation in the organs of the mononuclear phagocytic system (MPS) and low accumulation in the tumor.
5. Incorporation of the positron emitter copper-64 at the core of spherical gold nanoparticles with core size 9-11 nm and subsequent investigation using PET imaging in a xenograft mouse model of human gastrointestinal cancer, showed significant accumulation in the organs of the MPS and low accumulation in the tumor. Reduction of the core size of the spherical particles to 3-4 nm in diameter resulted in a higher bioavailability and increased accumulation in the tumor, with values of 5.3±1.3 %ID/cm^3 at 24 hours after intravenous administration. These results were confirmed by *ex vivo* analysis using Inductively Coupled Plasma-Mass Spectrometry (ICP-MS).
6. Incorporation of the positron emitter copper-64 at the core of gold nanorods with core size 37±3 × 10±1 nm (length × width; aspect ratio of 3.7) and subsequent investigation using PET imaging in a xenograft mouse model of human gastrointestinal cancer, showed accumulation in the organs of the MPS and significant accumulation in the tumor, with values of 3.3±1.2

%ID/cm^3 at 24 hours after administration. These results, which were confirmed by *ex vivo* analysis using ICP-MS, suggest the potential use of the nanosystems as boron carriers for BNCT and sensitizers for photothermal therapy.

6.2. Future directions

The work conducted in this PhD thesis has demonstrated that stable and biocompatible gold nanosystems functionalized with boron-rich compounds can be prepared, characterized and radiolabeled for the subsequent evaluation using *in vivo* positron emission tomography imaging. Despite the accumulation of boron in the tumor was not sufficient to guarantee therapeutic efficacy, the work conducted here may represent the first step towards the development of gold-based BNCT agents.

From the work reported, it is clear that size and shape tuning of the core of the nanosystems has a clear effect on the biodistribution and tumor accumulation. Hence, future work should tackle the investigation of other particle sizes, stabilizing agents and core-shapes, aiming at maximizing the boron content in the nanosystems and the accumulation of the nanosystems in the tumor. Also, the results obtained in chapter 5 related to the application of boron-rich gold nanorods, open new avenues for the preparation of nanosystems suitable for combined therapies. Hence, the use of gold nanosystems with favorable plasmonic properties, such as nanostars, is worth to be explored.

Annex I. NMR spectra

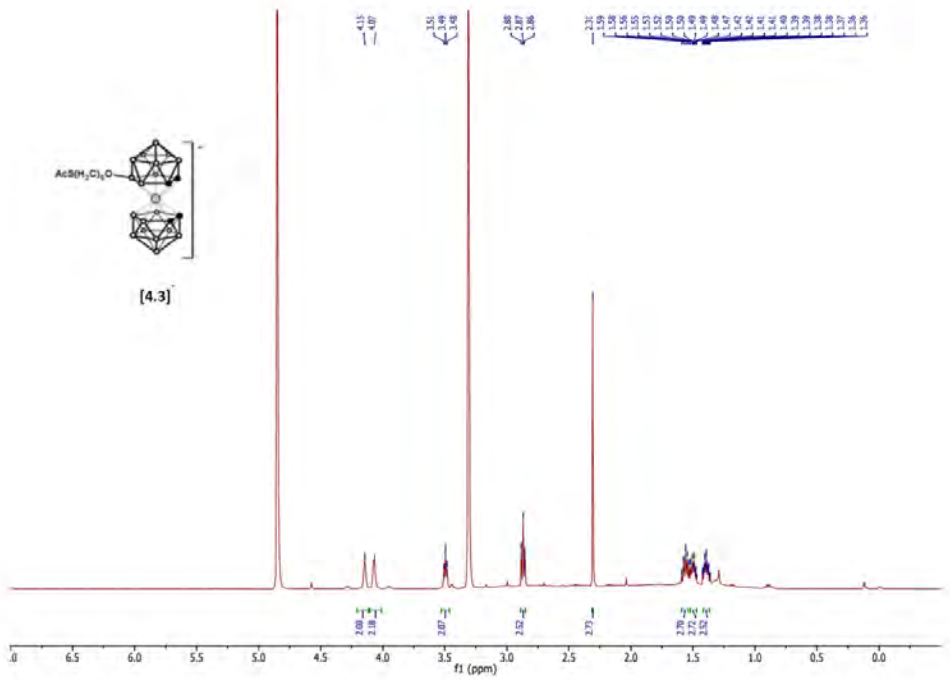

500 MHz ^{1}H NMR spectrum of **[4.3]**$^{-}$ in MeOD

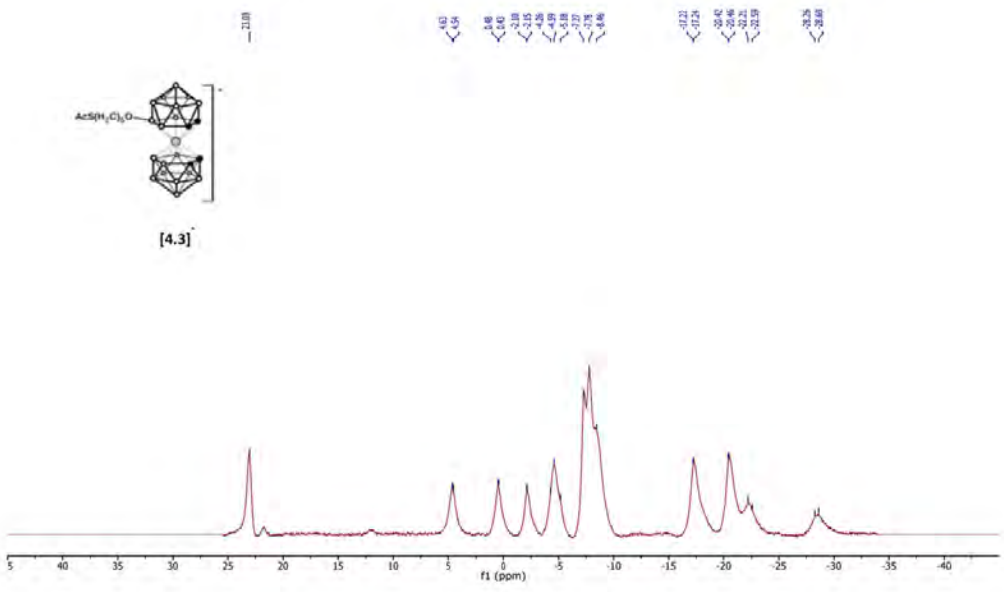

160 MHz ^{11}B NMR spectrum of **[4.3]**$^{-}$ in MeOD

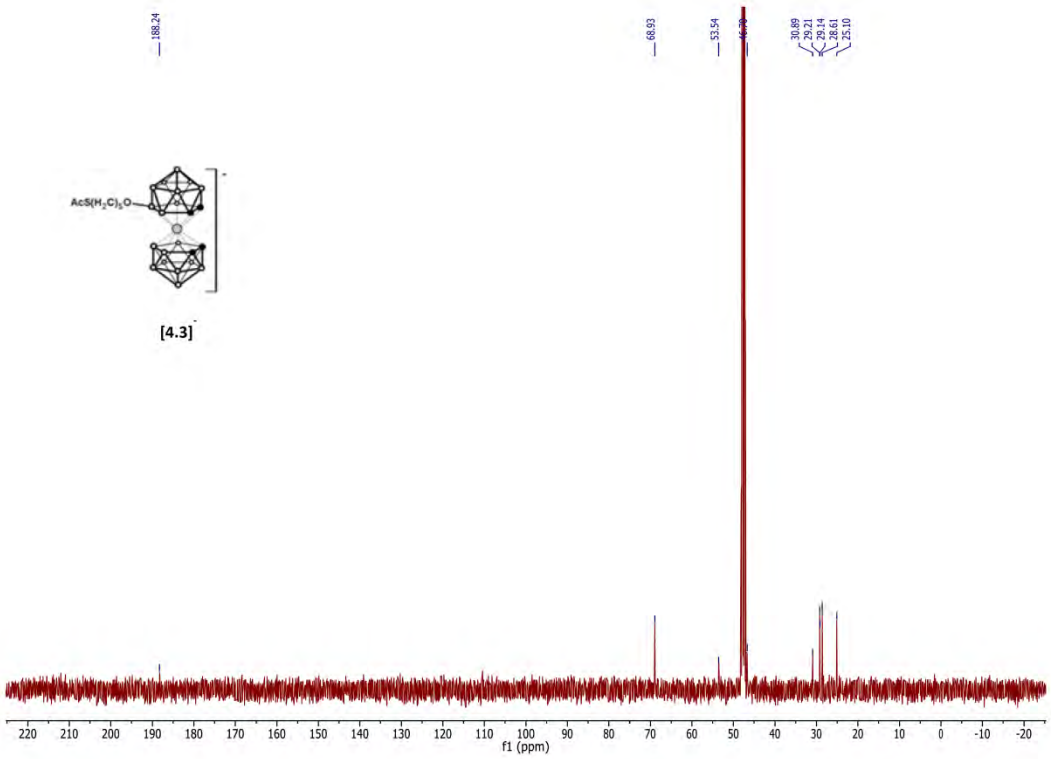

126 MHz ^{13}C NMR spectrum of **[4.3]**$^{-}$ in MeOD

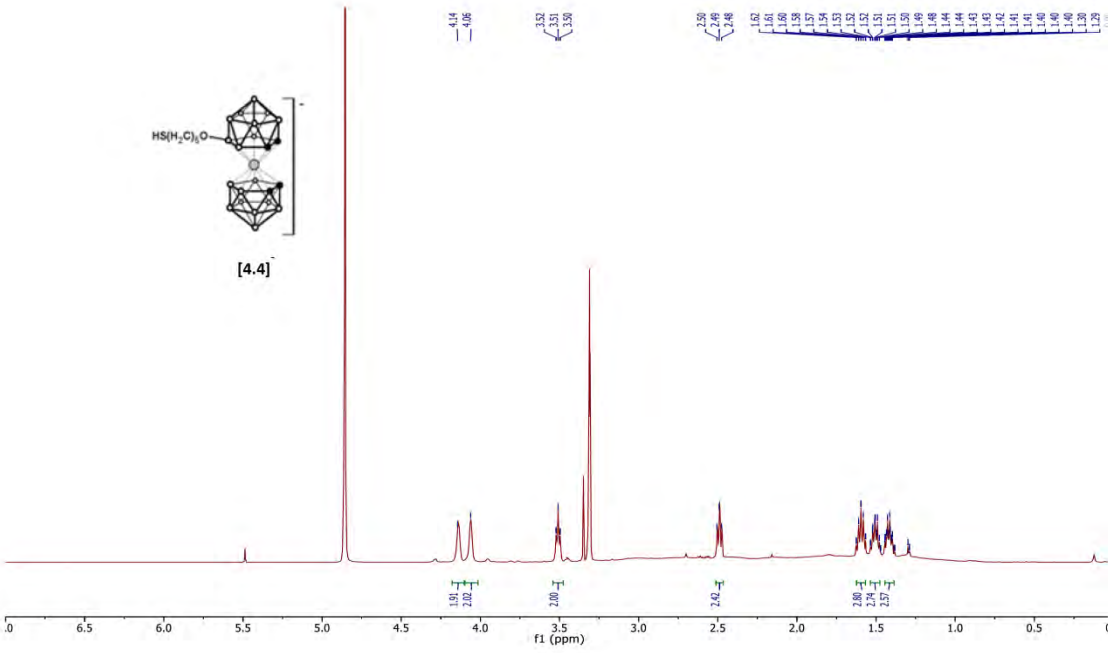

500 MHz ^{1}H NMR spectrum of **[4.4]**$^{-}$ in MeOD

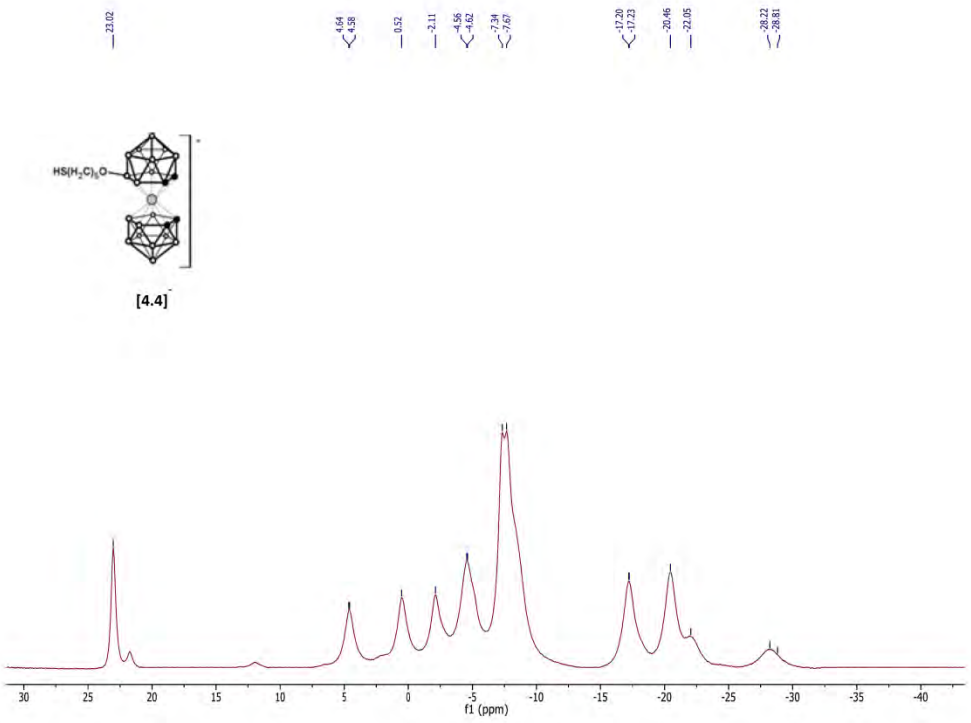

160 MHz ^{11}B NMR spectrum of **[4.4]**$^-$ in MeOD

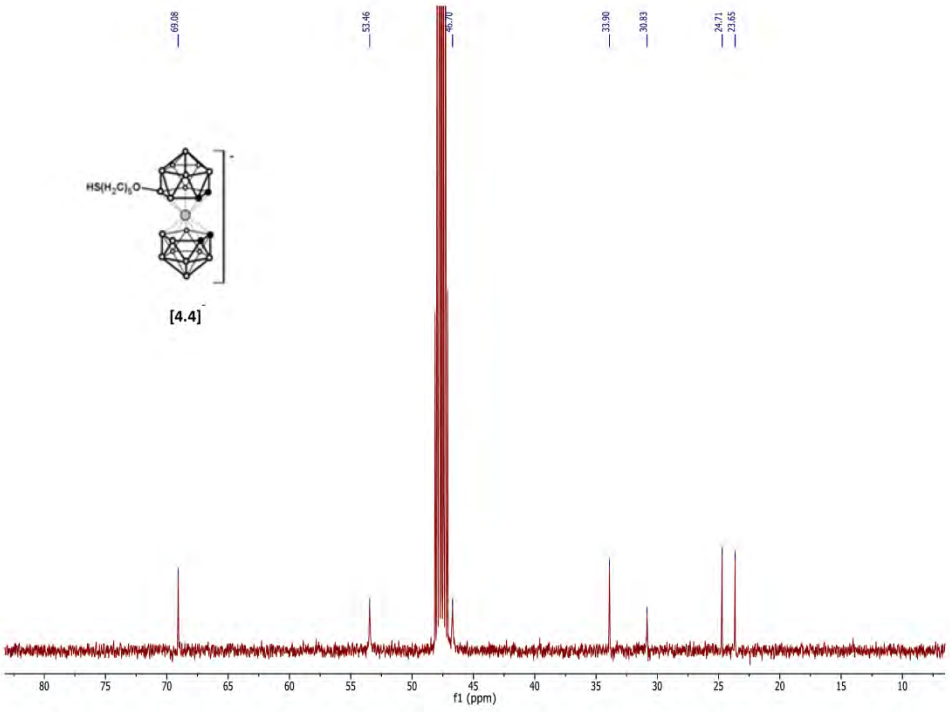

126 MHz ^{13}C NMR spectrum of **[4.4]**$^-$ in MeOD

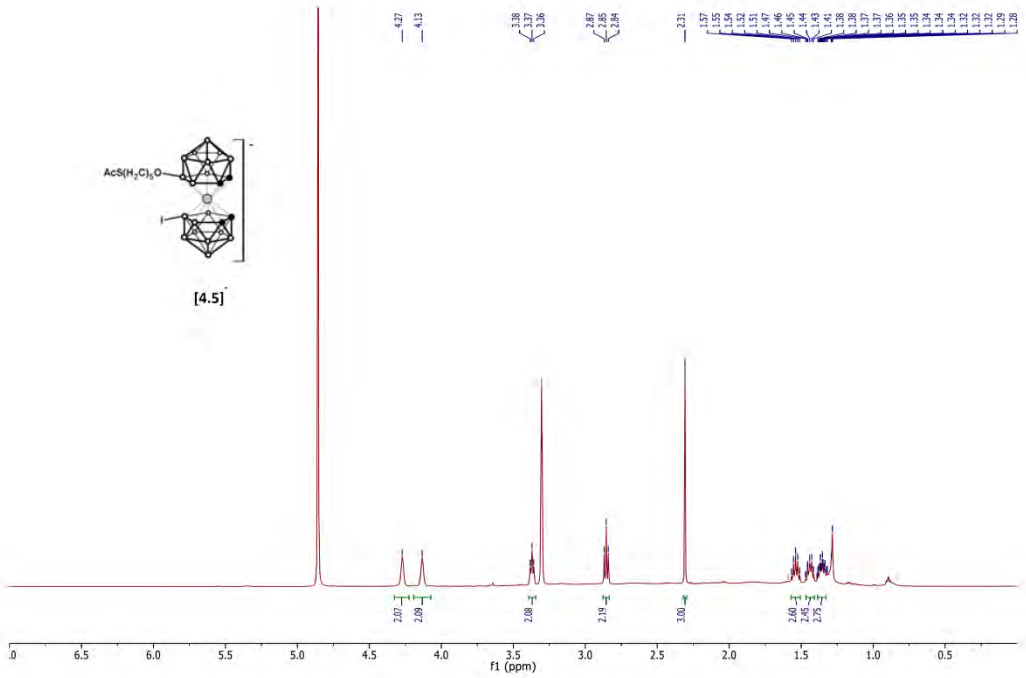

500 MHz ^{1}H NMR spectrum of **[4.5]**$^{-}$ in MeOD

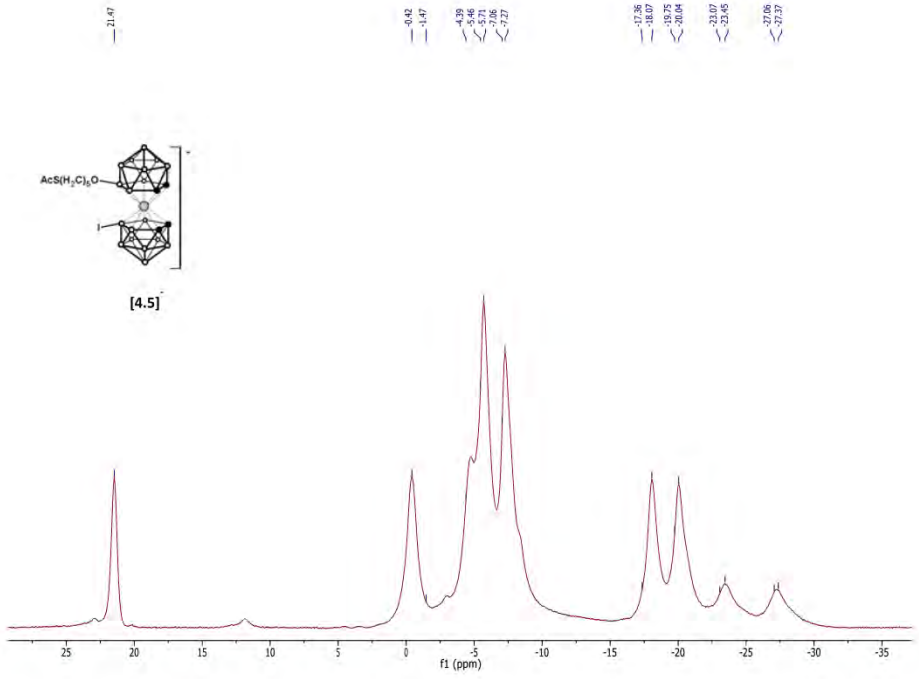

160 MHz ^{11}B NMR spectrum of **[4.5]**$^{-}$ in MeOD

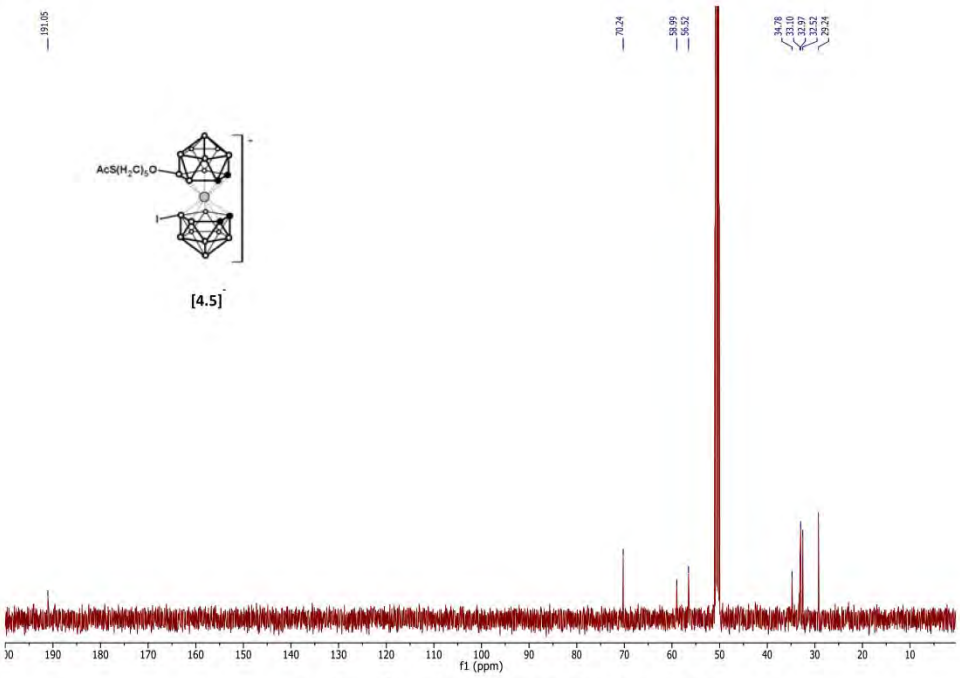

126 MHz ^{13}C NMR spectrum of **[4.5]**$^{-}$ in MeOD

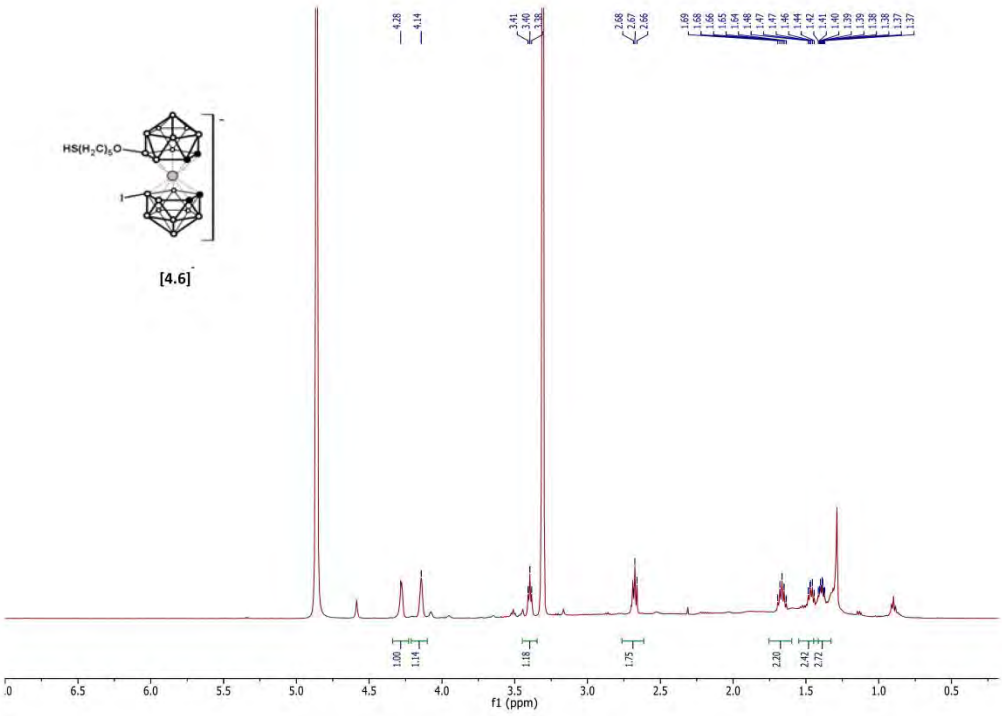

500 MHz ^{1}H NMR spectrum of **[4.6]**$^{-}$ in MeOD

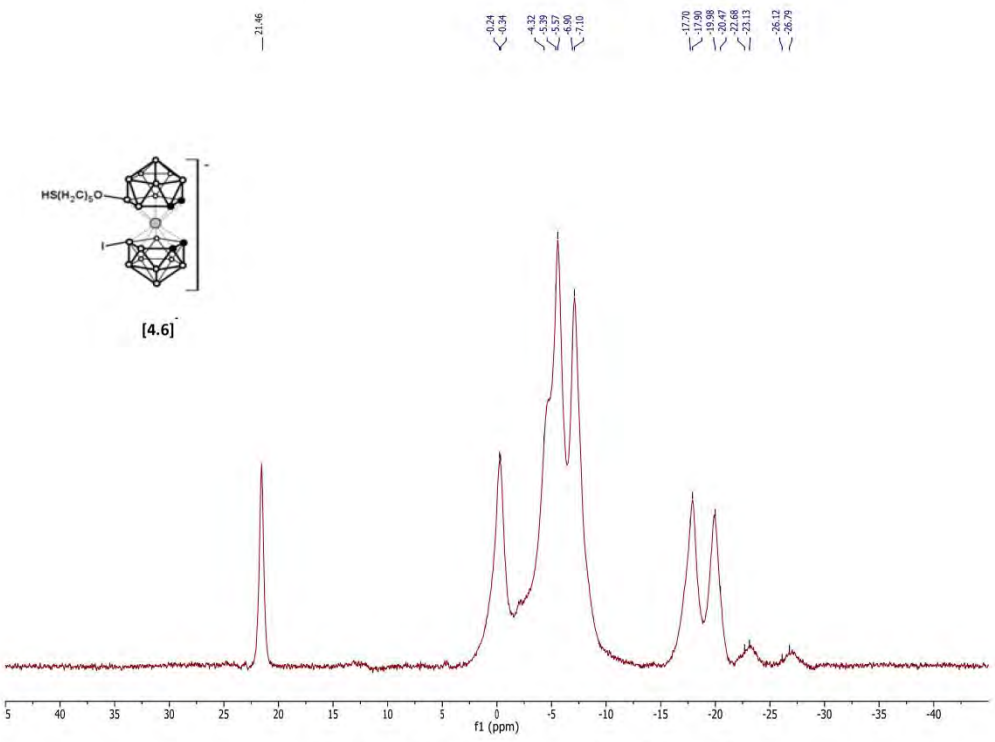

160 MHz ^{11}B NMR spectrum of **[4.6]**$^-$ in MeOD

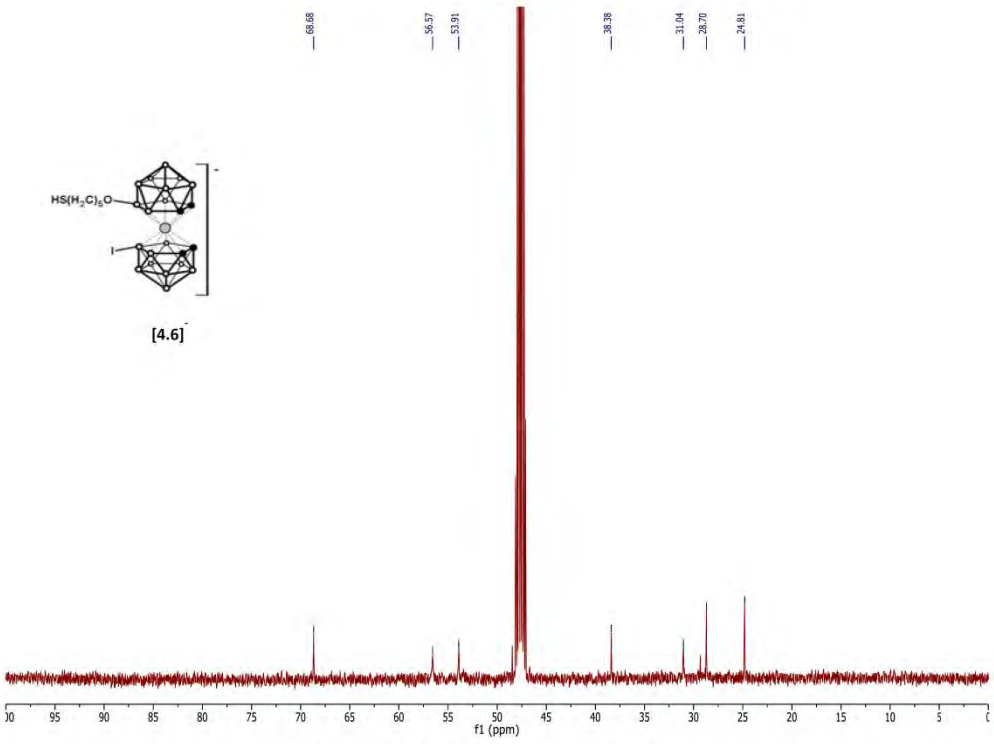

126 MHz ^{13}C NMR spectrum of **[4.6]**$^-$ in MeOD